

**SELF-CLEANING OF GLASS AND POLYCARBONATE  
SURFACES USING TEXTURING AND DYNAMIC  
ROTATION**

BY  
**ADITIA RIFAI**

A Thesis Presented to the  
DEANSHIP OF GRADUATE STUDIES

**KING FAHD UNIVERSITY OF PETROLEUM & MINERALS**

DHAHRAN, SAUDI ARABIA

In Partial Fulfillment of the  
Requirements for the Degree of

**MASTER OF SCIENCE**

In  
**MECHANICAL ENGINEERING**

**DECEMBER 2015**

KING FAHD UNIVERSITY OF PETROLEUM & MINERALS

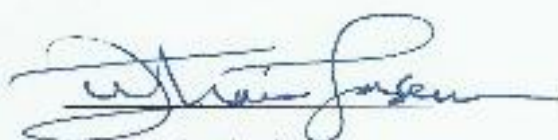
DHAHRAN- 31261, SAUDI ARABIA

**DEANSHIP OF GRADUATE STUDIES**

This thesis, written by Adria Rifai under the direction his thesis advisor and approved by his thesis committee, has been presented and accepted by the Dean of Graduate Studies, in partial fulfillment of the requirements for the degree of **MASTER OF SCIENCE IN MECHANICAL ENGINEERING.**



Dr. Numan Abu-Dheir  
(Advisor)



Dr. Zuhair Ghasim  
Department Chairman



Dr. Sami Bekir Yilbas  
(Member)



Dr. Salam A. Zuaino  
Dean of Graduate Studies



Dr. Mazen Muhammad Khaled  
(Member)

18/4/16

Date

© Aditia Rifai

2015

### *Dedication*

I dedicate this thesis to my family for nursing me with affections and love and their dedicated partnership for success in my life

## ACKNOWLEDGMENTS

بسم الله الرحمن الرحيم

All the praises and thanks be to Allah who gave me the opportunity and capability to finish my study in KFUPM.

I am deeply indebted and most sincere appreciation goes to my advisor, Dr. Numan Abu-Dheir, for knowledge, patience, encouragements, and guidance he has shown me over the past few years that I have been with this department, be it scientifically, personally, or academically.

I would like to thank my thesis committee members for their support and sharing their knowledge over the years: Dr. Bekir Sami Yilbas from Mechanical Department and Dr. Mazen Mohammad Khaled from Chemistry Department. I acknowledge also the financial support of King Fahd University of Petroleum and Minerals (KFUPM) through Project# MIT11111-11112 to accomplish this work.

Thanks to my wonderful family: my parents, Emak and Bapak, for their endless pray, love and support; my brother and sisters, for keeping my spirit and encouragement during my master journey; and lastly — to my wife Siti Nurhayati, your endless love, support and encouragement has been most influential and inspiring.

# TABLE OF CONTENTS

ACKNOWLEDGMENTS .....	V
TABLE OF CONTENTS .....	VI
LIST OF TABLES.....	X
LIST OF FIGURES.....	XI
LIST OF ABBREVIATIONS .....	XVII
ABSTRACT .....	XVIII
ملخص الرسالة.....	XXI
CHAPTER 1 INTRODUCTION.....	1
1.1 Dust adhesion problem .....	1
1.2 Self-cleaning surface .....	3
1.3 Dust cleaning methods.....	5
1.4 Scoop of the work.....	7
CHAPTER 2 LITERATURE REVIEW.....	8
1.5 Dust adhesion forces.....	8

1.5.1	Contact Mechanic.....	8
1.5.2	Surface Energy.....	10
1.5.3	Cassie-Baxter and Wenzel theory .....	11
1.6	Factors affecting self-cleaning properties.....	12
1.6.1	Surface Functional Groups to hydrophobicity.....	12
1.6.2	Surface Structure Effect to hydrophobicity.....	12
1.6.3	Surface roughness effect to transmittivity.....	15
1.7	Surface Texturing.....	17
1.7.1	Modified silica nanoparticle .....	17
1.7.2	Oil impregnated silica nanoparticle .....	21
1.7.3	Silica Nanoparticle Aerogel deposition by Sol-gel process .....	22
1.7.4	PDMS double casting.....	24
1.8	Dynamic dust cleaning .....	27
1.9	Dust Characterization.....	30
<b>CHAPTER 3 MATERIALS AND METHODS.....</b>		<b>33</b>
1.10	Materials.....	33
1.10.1	Oil impregnated silica nanoparticle and sol-gel process.....	33
1.10.2	PDMS double casting .....	34

1.10.3	Dynamic dust cleaning .....	34
1.11	Methods.....	35
1.11.1	Oil impregnated silica nanoparticle.....	35
1.11.2	PDMS double casting .....	37
1.11.3	Silica aerogel nanoparticle deposition by sol-gel dip-coating .....	39
1.11.4	Dynamic Dust Cleaning .....	40
1.12	Characterization .....	40
1.12.1	Scanning Ellectron Microscope (SEM) .....	40
1.12.2	Ultraviolet Visible (UV-Vis) light Spectrophotometer .....	42
1.12.3	Water Contact Angle Masurement.....	42
1.12.4	Atomic Force Microscope.....	44
1.12.5	Particle Size Analyzer .....	44
<b>CHAPTER 4 RESULTS AND DISCUSION.....</b>		<b>45</b>
1.13	Dust Particle Characterization .....	45
1.14	Oil Impregnated Silica Nanoparticle .....	48
1.15	PDMS Double Casting .....	55
1.16	Silica Aerogel Nanoparticle Deposition by Sol-gel Dip-coating.....	61
1.17	Dynamic Dust Cleaning.....	65



<b>CHAPTER 5 CONCLUSION AND FUTURE WORK.....</b>	<b>78</b>
<b>1.18 Conclusion.....</b>	<b>78</b>
<b>1.18.1 Surface Texturing.....</b>	<b>78</b>
<b>1.18.2 Dynamic Dust Cleaning .....</b>	<b>79</b>
<b>1.19 Future Work .....</b>	<b>79</b>
<b>1.19.1 Surface Texturing.....</b>	<b>79</b>
<b>1.19.2 Dynamic Dust Cleaning .....</b>	<b>80</b>
<b>REFERENCES .....</b>	<b>81</b>
<b>VITAE .....</b>	<b>87</b>

## LIST OF TABLES

Table 1 Average relative composition (atomic percent) of the particle classes .....	31
Table 2 Mean, standard deviation and peak value of dust particle dust distribution.....	46
Table 3 EDS quantitative analysis of dust particle .....	48
Table 4 Oil impregnated silica nanoparticle's samples .....	49
Table 5 Water contact angle and transmittivity measurement of oil impregnated nanoparticle surface .....	52
Table 6 PDMS lotus leaf double casting's samples.....	56
Table 7 The samples list of silica aerogel nanoparticle deposition .....	62
Table 8 Dust removed from polycarbonate disk surface by rotation.....	73
Table 9 The elemental analysis of dust residue on the disk surface .....	74

## LIST OF FIGURES

Figure 1 Saudi power plan in 2032 [1] .....	1
Figure 2 Dust Accumulation effect to photovoltaic energy loss [3] .....	2
Figure 3 self-cleaning lotus leaf.....	3
Figure 4 Water contact angle of superhydrophilic and superhydrophobic surfaces [14]..	4
Figure 5 Sliding angle measurement [16] .....	4
Figure 6 Various ways dust cleaning methods: (a) mop and drinking water, (b) steam, (c) compress air, (d) pressurized water, (e) automatic robot device, (f) electric curtain, (g) sprinle water and (h) automatic brushes [22] .....	6
Figure 7 Hamaker's model [28] .....	9
Figure 8 Rumpf-rabinovich's model [29].....	10
Figure 9 Surface energy diagram on water contact angle .....	11
Figure 10 Cassie-Baxter and Wenzel state illustration [32] .....	11
Figure 11 Surface functional groups [35].....	13
Figure 12 The fitted curve of hierarchical structure effect to contact angle (contact angle, in degrees, against the mean outer diameter of protruding structures, in micrometers) [36].....	13
Figure 13 variation of hierarchical structure n-hexatriacontane and its effect to water contact angle [37].....	14
Figure 14 Transmittance loss SiO <sub>2</sub> /TiO <sub>2</sub> film due to surface roughness [40] .....	15
Figure 15 Spectral response of various solar cell [43] .....	16
Figure 16 water contact angle measurement of silica-PDMS surfaces with different particle size and concentration: (a) 7 nm and 0.5 % w/v: 93°, (b) 7 nm and	

1.0 % w/v: 99°, (c) 7 nm and 2.0 % w/v: 130°, (d) 14 nm and 0.5 % w/v: 95°, (e) 14 nm and 1.0 % w/v: 103°, and (f) 14 nm and 2.0 % w/v: 147°	
[44] .....	17
Figure 17 SEM images of silica-PDMS surfaces with (a) 14 nm silica particle and 2.0 % w/v silica concentration and (b) 7 nm silica particle and 2.0 % w/v silica concentration [44] .....	18
Figure 18 illustration of drop coating procedure of superhydrophobic PDMS-based surface [45] .....	19
Figure 19 Top side: SEM image PDMS/Silica coating on glass substrate using (a) unmodified 500 nm silica particle (b) modified 500 nm silica particle; bottom side: SEM image and water contact angle of PDMS/M-silica at different curing temperature: (a) 60°C, (b) 100°C, and (c) 140°C [45].....	20
Figure 20 (a) the schematic process of laser etching, (b) the schematic process of PDMS casting [46].....	20
Figure 21 (a) SEM micro image of laser-etched PDMS with (b, c) higher magnification; (d) comparison laser-etched and flat PDMS; (e) water contact angle: 162°; (f) sliding contact angle: less than 5° [46] .....	21
Figure 22 SEM micrograph of the silica aerogel samples by different molar ratio: (a) and (b) are 0.043 and 0.35 molar ratio of NH <sub>4</sub> OH/MTMS, (c) and (d) are 2 and 8 are molar ratio of H <sub>2</sub> O/MTMS, and (e) and (f) are 3.5 and 14 are molar ratio of MeOH/MTMS [61] .....	22
Figure 23 AFM image of silica aerogel film with (a) 0 and (b) 0.43 molar ratio of MTES/TEOS [62] .....	23

Figure 24 Schematic of PDMS casting process using SiC paper template [63].....	24
Figure 25 (a) 3D AFM image of PDMS surface (b) vertical roughness of PDMS surface, (c) water contact angle measurement of PDMS surface .....	25
Figure 26 illustration of nanocasting procedure of superhydrophobic PDMS surface [65] .....	26
Figure 27 SEM and water contact angle image of (a, d) lotus leaf, (b, e) positive replica PDMS surface, (c, f) negative replica PDMS surface [65] .....	26
Figure 28 Hubbe's model on the lift force [69] .....	28
Figure 29 Flow profile acting on the spherical particle [73] .....	30
Figure 30 Elemental Composition of Dust Particle in Kuwait/Iraq [75] .....	31
Figure 31 Rotational dust cleaning setup .....	34
Figure 32 oil impregnated silica nanoparticles procedure.....	36
Figure 33 illustration of PDMS double casting process .....	38
Figure 34 illustration of Sol gel silica procedure.....	39
Figure 35 TESCAN LYRA3 FEG-SEM .....	41
Figure 36 JEOL Scanning Electron Microscope .....	41
Figure 37 JENWAY 6705 UV-Vis Spectrophotometer .....	42
Figure 38 Kyowa DM-501 contact angle meter .....	43
Figure 39 Nanomagnetix Instrument high performance atomic force microscope (hpAFM).....	43
Figure 40 Microtrac S3500 Particle Size Analyzer.....	44
Figure 41 The dust particle size distribution was presented in number, area and volume percentile .....	46

Figure 42 SEM micrographs of dust particle.....	47
Figure 43 SEM micrograph of EDS measurement of dust particle .....	47
Figure 44 Static water contact angle of (a) glass substrate, (b) mixed-size silica nanoparticle, (c) sample A11, (d) sample A12, (e) sample B11 and (f) sample B12 .....	51
Figure 45 Transmittivity curve of oil impregnated silica nanoparticle samples from 300 – 900 nm wavelength.....	52
Figure 46 SEM micrograph of (a & b) sample O: silica mixed size and (c & d) sample A1: 5% TMCS on silica mixed size.....	53
Figure 47 surface silanization of (left) TMCS and (right) PFOTS .....	54
Figure 48 AFM scanning image of (left) glass substrate, (b) sample O and (c) sample A11 .....	54
Figure 49 Optical camera photograph of PDMS double casting samples: (a) - (d) are negative replica, positive replica, TMCS coated positive replica and oil impregnated TMCS coated positive replica of lotus leaf respectively, and (e) - (h) are negative replica, positive replica, TMCS coated positive replica of ice leaf respectively.....	57
Figure 50 Transmittivity curve of lotus leaf replica PDMS double casting.....	57
Figure 51 Transmittivity curve of rice leaf replica PDMS double casting.....	58
Figure 52 SEM micrograph of (left to right) lotus leaf, negative replica and positive replica .....	58
Figure 53 Water contact angle of lotus leaf replica .....	59

Figure 54 SEM micrograph of lotus leaf (a & b), negative replica (c & d) and positive replica (e & f).....	60
Figure 55 Water contact angle of rice leaf replicas.....	61
Figure 56 Water contact angle of the samples (sample 4 is oil impregnated of sample 2) .....	62
Figure 57 Surface free energy of the samples.....	63
Figure 58 The transmittivity of the samples .....	63
Figure 59 SEM micrograph of sample 1, 2 and 3 respectively from left to right .....	64
Figure 60 AFM image of sample 1, 2 and 3 respectively from left to right .....	64
Figure 61 A schematic view of forces acting on the dust particles during spinning .....	65
Figure 62 Friction coefficient for polycarbonate plane sheet without dust on the surface. ....	66
Figure 63 Contour plots of force ratios along the radial distance ( $r$ ) for different dust particle radius ( $R$ ). The rotational speed is 100 rad/s. ....	68
Figure 64 Contour plots of force ratios along the radial distance ( $r$ ) for different rotational speed ( $\omega$ ). The dust particle radius is 10 $\mu\text{m}$ . ....	69
Figure 65 Semi-log plot of forces along radial distance along disk surface for two dust particle sizes. Adhesion force variation along dust particle radius at disk edge and for $\omega = 100$ rad/s. ....	70
Figure 66 Semi-log plot of forces with dust particle radius ( $R$ ) for two radial locations on disk. ....	71
Figure 67 Semi-log plot of forces with rotational speed ( $\omega$ ) for two radial locations on disk. ....	73

Figure 68 SEM micrographs of dust residues on polycarbonate disk: a) small and large size dust residues, b) dust residues composes of fine size dust particles, c) combined dust particles, d) elongated dust particles composing of fine size dust particles. ....	76
Figure 69 AFM micro-images of dust particle and the adhesion force: a) dust particle on polycarbonate surface, and b) tangential force map recorded from AFM. The peak in the red circle represents the tangential force for the dust particle shown above. ....	77



## LIST OF ABBREVIATIONS

<b>TEOS</b>	:	Tetraethoxysilane
<b>ODTS</b>	:	Octadecyltrichlorosilane
<b>MTES</b>	:	Methyltriethoxysilane
<b>MTMS</b>	:	Methyltrimethoxysilane
<b>TMCS</b>	:	Trimethylchlorosilane
<b>PFOTS</b>	:	trichloro (1H, 1H, 2H, 2H-perfluorooctyl) silane
<b>SAM</b>	:	Self Assembly Monolayer
<b>PDMS</b>	:	Polydimethylsiloxane
<b>SEM</b>	:	Scanning Electron Micrograph
<b>AFM</b>	:	Atomic Force Micrograph
<b>WCA</b>	:	Water Contact Angle
<b>UV-Vis</b>	:	Ultraviolet-visible

## ABSTRACT

Full Name : Aditia Rifai

Thesis Title : Self-Cleaning Of Glass And Polycarbonate Surfaces Using Texturing  
And Dynamic Rotation

Major Field : Materials Science and Engineering

Date of Degree : December, 2015

Self-cleaning surfaces are being fabricated by various methods and materials in order to keep the surface clean from dust. However, most of those surfaces are opaque mainly due to its micro-nano structure of its surface, which is not applicable for photovoltaics. In this study, a novel fabrication method using oil impregnation is introduced on a glass surface with a layer of mixed-size (30, 75 and 220 nm) silica nanoparticles which is formed by dip-coating method. Silica colloidal particles are functionalized by using silane solution (trimethylchlorosilane or trichloro (1H, 1H, 2H, 2H-perfluorooctyl) silane) are deposited on to glass prior to oil impregnation at the surface for improving adherence of the oil. Contact angle measurements are carried out and the static water contact angle, sliding angle and average transmittivity of these resulting surfaces are found to be 113°, 3° and 83% respectively. A cleaning test is relied by incorporating small water droplets on a dusted surface and using a tilted surface at 10° with excellent results. Scanning electron microscope, SEM, and atomic force microscope, AFM, are used to characterize the morphology of the surface. The findings reveal that there are several valleys with varying depth in between the silica particles that function as air pocket to serve for storing oil on the surface. Characterization revealed a hierarchical (nano-micro) structures that are created due to the deposition of different sizes of silica particles where smaller particles lie

on top of bigger particles. The transmissivity of the engineered surfaces is measured and it is found that oil impregnation improves transmittance of the coated glass.

PDMS double casting is also used to replicate hydrophobic of lotus and rice leaves morphology towards producing transparent hydrophobic surface. The positive PDMS replica of lotus and rice leaves result in water contact angles of  $129^\circ$  and  $131^\circ$  respectively whereas the lotus and rice leaf contact angles are  $147^\circ$  and  $149^\circ$  respectively. SEM micrographs of these surfaces demonstrate that the micro details of lotus and rice leaves structures were replicated without nano details. The transmittivity of lotus leaf replica is lower than that of the rice leaf details due to randomly oriented and folded structure of the lotus leaf.

Silica aerogel-nanoparticle is also deposited on glass using sol-gel dip-coating method. The surface developed by this method shows very promising hydrophobicity of  $143^\circ$  static WCA and  $10 \text{ mJ/m}^2$  surface free energy. Oil impregnation process improves water droplet mobility with  $4^\circ$  sliding angle and decreasing WCA to  $110^\circ$ . It also increases the transmittance to 79%.

Dynamic forces are also used to clean dusted surface of glass and polycarbonate. The force generated from dynamic rotation to remove dust particles is calculated using Matlab software. The calculations are governed by centrifugal, drag, lift, gravitational and adhesion forces. Surface roughness effect is also considered in calculation of the adhesion force between dust particles and the substrate. The rotational speed and dust radial distance are varied to examine dynamic efficiency of dust removal. The experimental tests are also performed to show that dust accumulations are cleaned by amount of 3.2, 25.9, 61.4 and

78.2 % at rotational speed of 100, 175, 250 and 375 rpm respectively. In all of the above studies, dust samples are collected from precipitation atop of PV-panels that are located in KFUPM, Dhahran.

## ملخص الرسالة

الاسم الكامل: أديتيا رفاعى

عنوان الرسالة: لتنظيف الذاتي للزجاج والبوليكاربونيت باستخدام تغيير التركيب السطحي و الدوران الديناميكي

التخصص: علوم و هندسة المواد

تاريخ الدرجة العلمية: 1347/3/5 هجري

يتم بناء الأسطح ذاتية التنظيف باستخدام وسائل و مواد مختلفة بهدف الحفاظ عليها نظيفة من الغبار، و بالرغم من ذلك فإن هذه الأسطح تصبح قاتمة للضوء و ذلك بسبب البنية المايكرووية-النانونية لهذه الاسطح و الذي يجعلها غير ملائمة للتطبيقات الكهروضوئية، هذه الدراسة تقدم وسيلة جديدة باستخدام التحميل بالزيت لسطح زجاجي مكسو بطبقة من حبيبات السيليكون ذو أحجام نانوية (30، 70، 220 نانومتر) باستخدام الطلي بالغمس، تم تهيئة هذه الحبيبات باستخدام محلول سايليني (ترايمثايل كلوروسايلين أو ترايكلورويبيرفلوروأكتيل) و ترسيبها على سطح الزجاج قبل التحميل بالزيت، و من بعد تم قياس زاوية الملامسة والذي أنتج زاوية ملامسة ساكنة و زاوية انزلاق و معدل نفاذية للضوء بمقدار 113 درجة و 3 درجات و 83% على التوالي، و تم اعتماد اختبار تنظيف للأسطح باستعمال قطرات ماء على سطح مغبر و بزاوية ميلان ب 10 درجات والذي أخرج نتائج ممتازة، و تم استخدام مجهر المسح الإلكتروني و مجهر القوة الذرية لتوصيف البنية السطحية لعينات الأسطح، و أظهرت النتائج أن الأسطح لديها بنية ذات وديان متغيرة العمق بين حبيبات السيليكا والتي تعمل كجيوب هواء لتخزين الزيت على السطح، وقد أظهر التوصيف المجهرى بنية طبقية (نانوية- مايكرووية) نتيجة ترسيب حبيبات السيليكا مختلفة الأحجام حيث الحبيبات الأصغر تكون فوق الحبيبات الأكبر منها، و وجد أن تحميل الزيت يحسّن من قياس نفاذية الضوء.

بالإضافة إلى ما سبق تم استخدام السكب المزدوج لمادة البي دي إم إس لنسخ أوراق نبتة اللوتس ونبتة الأرز الطاردة للماء لهدف إنتاج أسطح نافذة للضوء و طاردة للماء، النسخة الإيجابية (المماثلة) لورقتي اللوتس و الأرز كان لهما زاوية ملامسة للماء مقاسة ب 129 درجة و 131 درجة على التوالي بينما كان لورقتي اللوتس و الأرز زاوية الملامسة إلى 147 درجة و 149 درجة على التوالي، و بينت الصور المجهرية للماسح الإلكتروني لنسخ ورقتي اللوتس و الأرز وجود البنية المايكرووية مع فقدان البنية النانوية، و كان النفاذ الضوئي لنسخة ورقة اللوتس أقل من نفاذية نسخة ورقة الأرز و ذلك بسبب النية العشوائية و المطوية لورقة اللوتس.

تم استخدام إضافة لما سبق ترسيب حبيبات الإيروجل-النانوية على سطح الزجاج بإستخدام الطلي بالتغميس لمادة السائل-الهلامي، فأظهر السطح المنتج بهذه الطريقة خاصية واعدة لطرد الماء تقدر بزاوة ملامسة للماء من 143 درجة و طاقة حرة للسطح ب 10 ملي جول/ متر<sup>2</sup>، وقد حسن التحميل بالزيت حركية قطرة الماء بزاوية ميلان 4 درجات وقلل زاوية ملامسة الماء إلى 110 درجات، و كذلك زاد من نفاذية الضوء إلى 79%.

أستخدمت القوة الديناميكية لتنظيف سطح زجاج و سطح بوليكاربونيت مغبرين، و تم حساب القوة المتأتية من الدوران الديناميكي و المستخدم لإزالة الغبار بإستعمال برنامج الحاسوب المسمى باتلاب، حيث كانت الحسابات محكومة بالقوة الطاردة و قوة الإحتكاك و قوة الرفع و قوة الجاذبية و قوة اللصق، وتم الأخذ بالخشونة بين السطح و الغبار بعين الاعتبار، و تم فحص الفعالية الدينامكية لتنظيف الغبار عن طريق تغيير السرعة الدورانية و المسافة النصف قطرية، و تم عمل التجارب لإظهار أن الغبار المتراكم نظف بمقدار 3.2 و 25.9 و 61.4 و 78.2% عند استخدام سرعات دوران من 100 و 175 و 175 و 250 و 375 دورة بالدقيقة على التوالي، و الجدير بالذكر أن الغبار المستخدم في هذه الدراسة تم جمعه من الغبار المتراكم من فوق أسطح اللوح الكهروضوئية و المجودة في جامعة الملك فهد للبترول و المعادن في منطقة الظهران.

# CHAPTER 1

## INTRODUCTION

### 1.1 Dust adhesion problem

Photovoltaic (PV) system has a big role as an alternative green energy source due to its huge resource of the sun, technology maturity and easiness to use. According to Kingdom power plan at 2032, as shown on Figure 1, one-third of total power plan will be coming from solar power both from photovoltaic and concentrated solar powers [1].

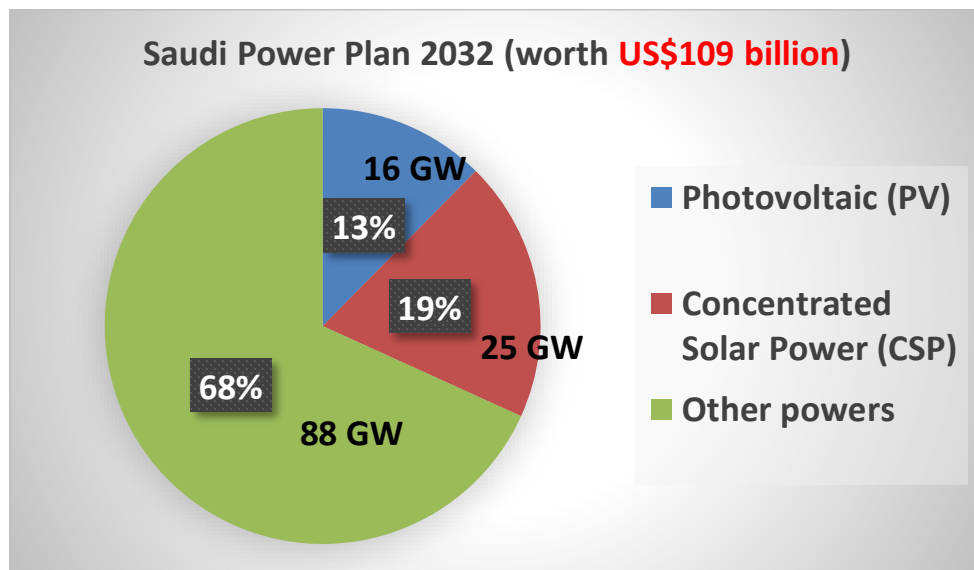


**Figure 1** Saudi power plan in 2032 [1]

However, current energy conversion from sun radiation to electric power is not really big, which is around 15-20% for semi-conductor PV type [2]. Therefore, the maintaining of this

amount of energy is very crucial; otherwise energy value compared to the cost is not significant. Moreover, there is also big problem in PV implementation which is efficiency reduction due to dust deposition or accumulation on the top surface of PV panels. The dust particles and other particulates can lead to 70% efficiency reduction in PV module after one year of accumulation [3]. In term of energy losses, even a relatively small amount of dust with  $1 \text{ g/m}^2$  deposition density causes around 183 SAR/kW<sub>p</sub> energy losses annually as illustrated on Figure 2 [4].

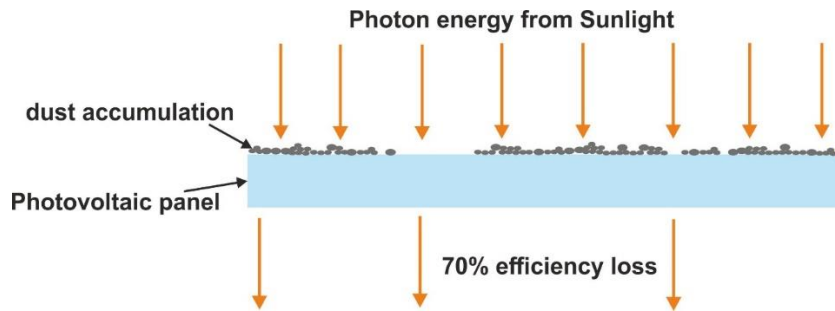


**Figure 2** Dust Accumulation effect to photovoltaic energy loss [3]

Many solutions for the problem of dust accumulation had been offered to overcome this loss either by active or by passive cleaning method. The accumulated dust can be cleaned actively by several ways, such as using fluid stream, ultrasonic, vibration, electric field and dynamic force [5–9]. Passive cleaning method is done by creating a self-cleaning surface with properties to ease cleaning process by reducing adhesion force between the surface and dust. One of the important surface property used in self-cleaning surfaces is superhydrophobicity of the surface [10–12]. Other reports argued that hydrophilic surfaces has good potential to be self-cleaning surfaces by the action of spreading and sliding of water droplets on the surface[12,13]. The following section provides a review to explain the mechanism by which hydrophobicity promotes self-cleaning characteristic.



## 1.2 Self-cleaning surface

A self-cleaning surface is a surface that can passively remove dust particles and other contaminants by utilizing rolling or sliding water droplets. As illustrated on Figure 3, when a water droplet rolls or slides on the surface, it will carry dust particles in its path of movement and thus clean the surface. Originally, this self-cleaning property was inspired by the action of lotus leaves. Other natural leaves also have similar self-cleaning capabilities, e.g. rice leaves.

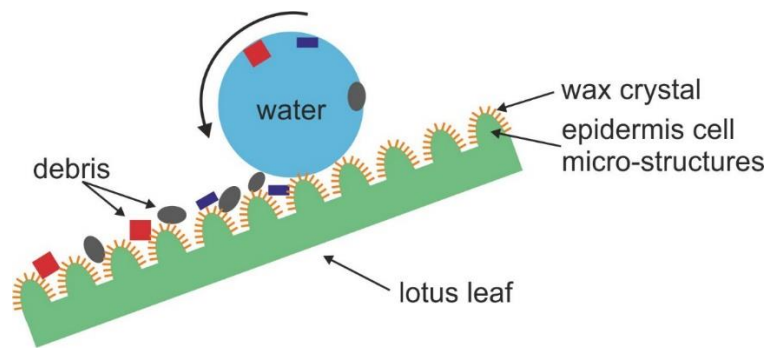


**Figure 3** self-cleaning lotus leaf

Self-cleaning surfaces are governed by two properties: hydrophobicity and the morphology of their surface. Hydrophobicity is evaluated by the surface energy of the surface where the water droplet resides. A surface with high surface energy is called hydrophilic. Hydrophobic surface has high tendency to attract water. On the contrary, a low surface energy surface is a hydrophobic surface. The parameter to distinguish these two opposite surfaces is water contact angle (WCA). Hydrophobic surface has WCA above  $90^\circ$  and hydrophilic one has WCA below  $90^\circ$ . Surfaces with WCA of  $150^\circ$  are called superhydrophobic and those with WCA of less than  $10^\circ$  are called superhydrophilic as shown on Figure 4 [14,15].

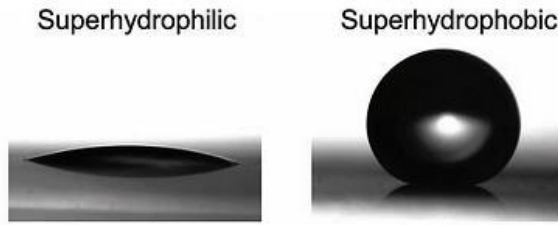


**Figure 4** Water contact angle of superhydrophilic and superhydrophobic surfaces [14]

Superhydrophobic surface repels water droplet easily allowing it to roll on the surface and collecting dust with it. Moreover, due to very low surface energy of superhydrophobic surface, the adhesion force between dust and surface will also be very low and thus making it easier to be removed. On the other hand, the cleaning mechanism of superhydrophilic surfaces is by spreading and sliding the water over the surface and bringing dust with it. Other self-cleaning properties related to water contact angle is sliding angle and hysteresis which are categorized as dynamic water contact angle as shown on Figure 5. Sliding angle is measured by tilting the surface with droplet on top of it from  $0^\circ$  until the droplet is sliding due to gravitational force and hysteresis is the difference of advancing angle ( $\theta_{\max}$ ) and receding angle ( $\theta_{\min}$ ) [16].

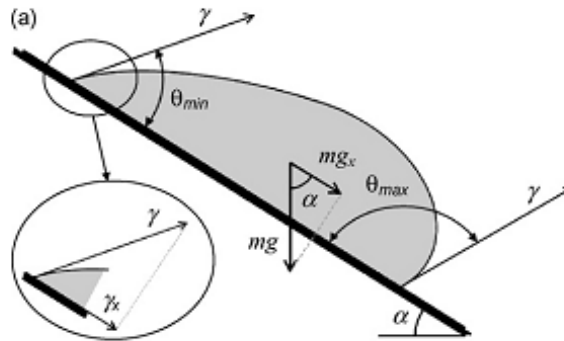


**Figure 5** Sliding angle measurement [16]

### 1.3 Dust cleaning methods

Dust accumulated on PV panels can be cleaned using several methods ranging from traditional to advanced ones as shown on Figure 6. A simple and traditional cleaning method is done by using a mop and water supply; a method that is labor intensive. Pressurized water is used to avoid the need for mops. It also could increase time efficiency and able to clean the spot that difficult to be cleaned by a mop. The steam and compressed air can be used to remove dust accumulation. There are automatic methods where the need for labor is minimized. These include robot device, automatic brushes, and sprinkle water [17]. An advanced method of using electric current to remove and repel the dust has also been utilized by NASA [8,9,18]. Utilizing mechanical vibration or centrifugal forces are examples of the use of dynamic method to clean surfaces from contamination [5,19]. More details on these techniques will be given in chapter 2.

A Self-cleaning surface is characterized by the significant reduction of adhesion forces between dust and surface. However, the self-cleaning surface still utilizes water droplet to clean the surface. This can be effective if it is implemented in an area that has high rainfall rate. For the relatively dry area which has very low rain rate, such as Saudi Arabia, it is very difficult and not really effective to clean the solar panels from dust accumulation using rainfall or external water resources. In Saudi Arabia, average annual rainfall is just around 82 mm which is far less than global average annual rainfall that is around 924 mm [20,21]. Water vapor coming from atmospheric humidity will not help much to clean the PV surface due to very small amount of water droplet create from water vapor. Moreover, water vapor can increase the adhesion force between PV surfaces and dust due to meniscus

force. Therefore, external forces are needed to enhance the cleaning of dust accumulation on PV surfaces in the desert area especially where it is difficult to provide water or any other fluids in the PV plant.

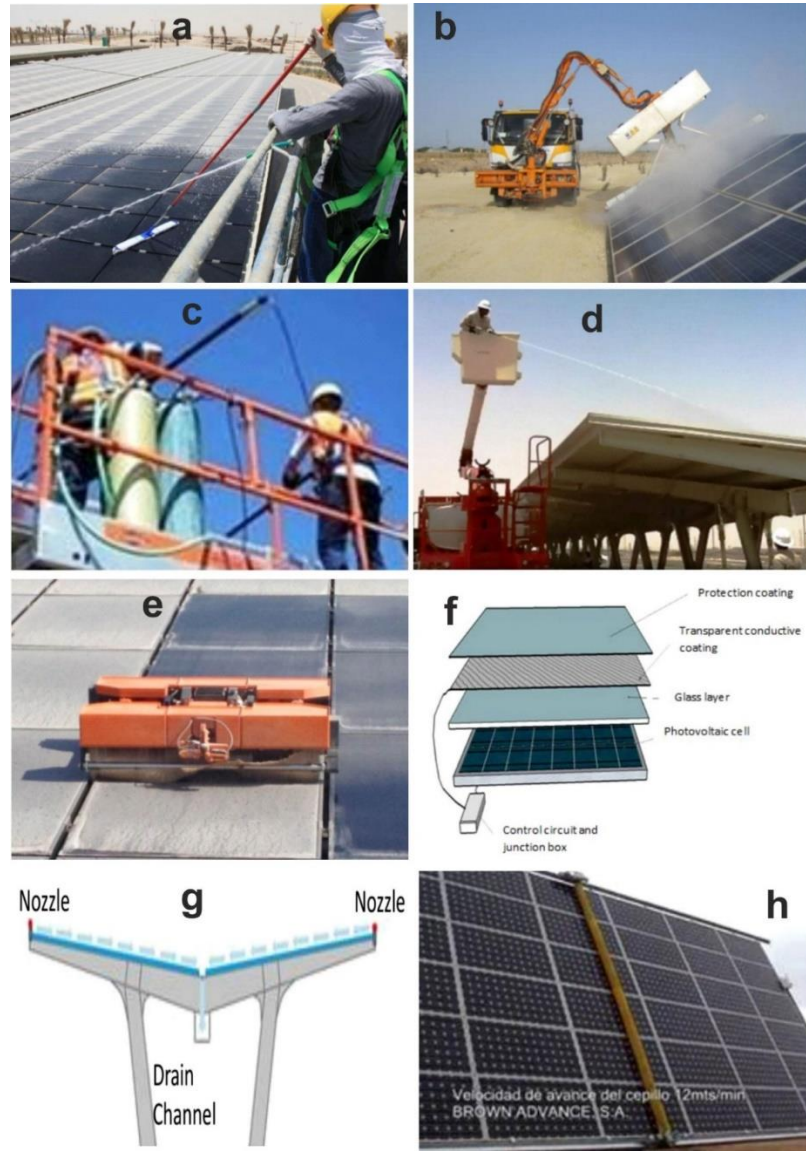


**Figure 6** Various ways dust cleaning methods: (a) mop and drinking water, (b) steam, (c) compress air, (d) pressurized water, (e) automatic robot device, (f) electric curtain, (g) sprinkle water and (h) automatic brushes [22]

In this study, we will investigate effect of surface texturing and dynamic rotation on the self-cleaning characteristics of glass and polycarbonate surfaces. Surface texturing is done by creating nano-rough surface, using silica nanoparticles deposition and PDMS casting, will promote the development of superhydrophobic surface which is the main properties for self-cleaning surface in solar cell application. While the rotational method aims at enhancing the effect of dust removal when there is no enough water to clean the solar panel surfaces. The materials used as substrate are polycarbonate and glass which are mainly used in solar panel covers.

#### **1.4 Scoop of the work**

This study was done to solve dust adhesion problem inside the Kingdom of Saudi Arabia (KSA) where dusty weather is common and become more intense as a result of increasing frequency of sand storms. Designing and engineering of self-cleaning surfaces is a promising solution to solve this problem since it can minimize dust adhesion and reduce the use of water during the cleaning of these surfaces. By applying self-cleaning coating, dust adhesion is expected to decrease and thus reducing the need for intensive use of water, labor and expensive techniques to clean them. To achieve this objective, the following techniques are approached; surface texturing to create self-cleaning surface and dust cleaning method by dynamic rotational force. Some surface texturing is followed by oil impregnation of surface modified silica nanoparticle. The second technique is to use double casting of polydimethylsiloxane on lotus and rice leaf texture. The third technique is to use silica aerogel nanoparticle sol-gel deposition. The last technique is the use of dynamic rotational to clean surfaces of polycarbonate and glass surface.

## CHAPTER 2

### LITERATURE REVIEW

#### 1.5 Dust adhesion forces

##### 1.5.1 Contact Mechanic

The adhesion of dust particle is affected by many factor such as van-der waals force, static electricity, relative humidity, contact area, surface roughness, agglomeration, time of contact, temperature and others [23]. For the sake of simplicity in this preliminary study, Van der Waals force is assumed that is the most common force that plays on particle adhesion [24,25]. Johnson et al. [26] has developed adhesion force theory which is coming from Van-der Waals force of spherical particle on flat wall. This theory is then known as JKR model.

$$F = \frac{3}{2}\pi R\gamma \dots\dots\dots 1$$

Where R is radius of the particle and  $\gamma$  is surface energy between two surfaces. This equation valid for large, soft bodies with high surface energy [24].

##### DMT model

In addition to that, Derjaguin et al. [27] had developed model which is also similar to JKR model but with different constant known as DMT model.

$$F = 2\pi R\gamma \dots\dots\dots 2$$

This equation is appropriate for small, hard solid particles with low surface energy[24].

## Hamaker's model

Another development of adhesion theory was developed by Hamaker as illustrated on Figure 7 [28].

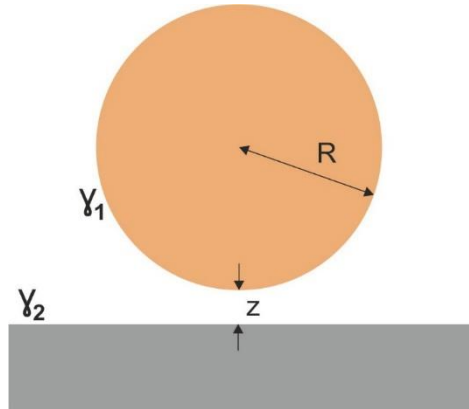


**Figure 7** Hamaker's model [28]

$$F = \frac{AR}{12Z_0^2} \dots\dots\dots 3$$

Where  $A$  is Hamaker constant and  $Z_0$  is separation distance between particle and the surface, normally 0.3 or 0.4 nm [24]. Hamaker model did not consider the particle contact area to the surface.

## Rumpf-Rabinovich model

Rabinovich et al. [29] modified Rumpf model which is about van der Waals force particle on rough surface. They calculated statistically the effect of RMS (root mean square) of the asperity of the rough surface as illustrated on Figure 8.

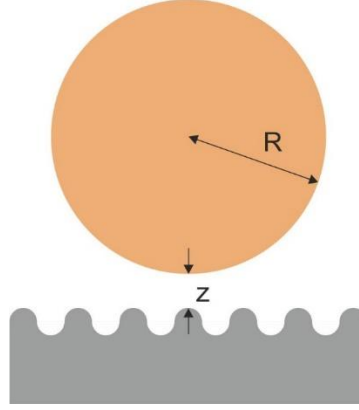


**Figure 8** Rumpf-rabinovich's model [29]

$$F = \frac{AR}{12Z_0^2} \left( \frac{1}{1 + \frac{R}{1.48RMS}} + \frac{1}{\left(1 + \frac{1.48RMS}{Z_0}\right)^2} \right) \dots\dots\dots 4$$

### 1.5.2 Surface Energy

Surface energy of the materials is derived from Young's equation.

$$\gamma_{SV} = \gamma_{SL} + \gamma_{LV} \cdot \cos\theta_Y \dots\dots\dots 5$$

Or familiarly written by

$$\cos\theta_Y = \frac{\gamma_{SV} - \gamma_{SL}}{\gamma_{LV}} \dots\dots\dots 6$$

Where  $\gamma_{SV}$  and  $\gamma_{SL}$  are surface energy of solid against vapor and liquid,  $\gamma_{LV}$  is surface energy of liquid against vapor and  $\theta_Y$  is Young's contact angle of surface and liquid which refers to diagram on Figure 9. The young's equation shows that contact angle affecting the surface energy or in other words surface energy can be measured by knowing the contact angle of the surface against liquid.



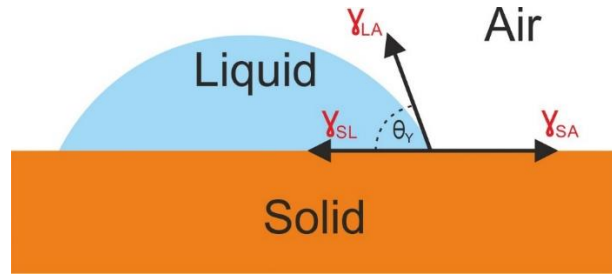


**Figure 9** Surface energy diagram on water contact angle

### 1.5.3 Cassie-Baxter and Wenzel theory

Modification of Young's equation is needed since real surface usually vary in practical condition. There are two famous modified versions of Young's equation which are Cassie-Baxter and Wenzel theories as illustrated on Figure 10 [30–34]. Wenzel theory proposed geometrical surface which is distinguish from actual surface.

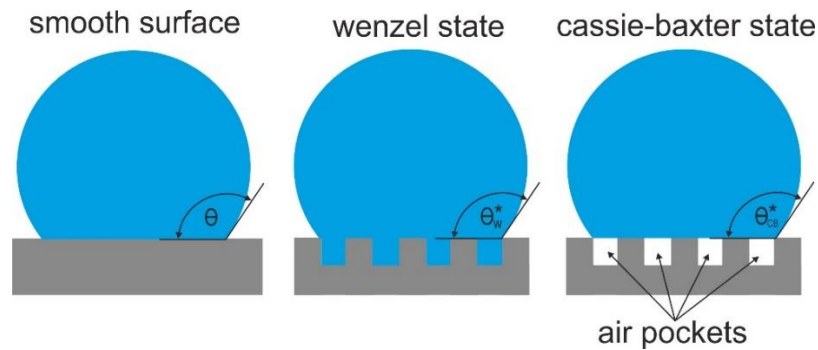


**Figure 10** Cassie-Baxter and Wenzel state illustration [32]

$$r \cdot \cos\theta = \cos\theta^* \dots\dots\dots 7$$

Or can be added by Young's equation

$$r \cdot \left( \frac{\gamma_{SV} - \gamma_{SL}}{\gamma_{LV}} \right) = \cos\theta^* \dots\dots\dots 8$$

Where  $r$  is surface roughness factor (actual surface/ geometric surface),  $\theta$  is real contact angle or Young contact angle which is smooth surface, and  $\theta^*$  is Wenzel apparent contact angle or also called  $\theta_W^*$ .

If there is air trapped inside air pockets of the surface structure, the Cassie-Baxter wetting state is needed to describe in which the fluid just only contact the top peak of the surface.

The contact fraction is called  $f$ .

$$\cos\theta^* = f \cdot (\cos\theta + 1) - 1 \dots\dots\dots 9$$

Where  $f$  is contact fraction and  $\theta^*$  is Cassie-Baxter apparent contact angle or called  $\theta_{CB}^*$ .

## 1.6 Factors affecting self-cleaning properties

### 1.6.1 Surface Functional Groups to hydrophobicity

In ordinary unmodified surface, there are many hydroxyl (-OH) groups on the surface which is coming from water vapor in the atmosphere. This hydroxyl groups will enhance the hydrophilicity of the surface to attract water by forming hydrogen bonding. For getting hydrophobic surface the unreacted functional groups is needed to repel water droplet. Some functional groups was used to create hydrophobicity effect are methyl (-CH<sub>3</sub>) and trifluorocarbon (-CF<sub>3</sub>) groups as shown on Figure 11 [35].

### 1.6.2 Surface Structure Effect to hydrophobicity

Surface roughness is the main factor to create self-cleaning surface. Increasing roughness of the surface reduces the apparent contact angle between solid and liquid, thus it reduces the surface energy since surface energy is a function of area. Moreover, surface roughness

forms air pockets which promotes water repellent effect. This water repellent effect will increases hydrophobicity and self-cleaning properties of the surface.

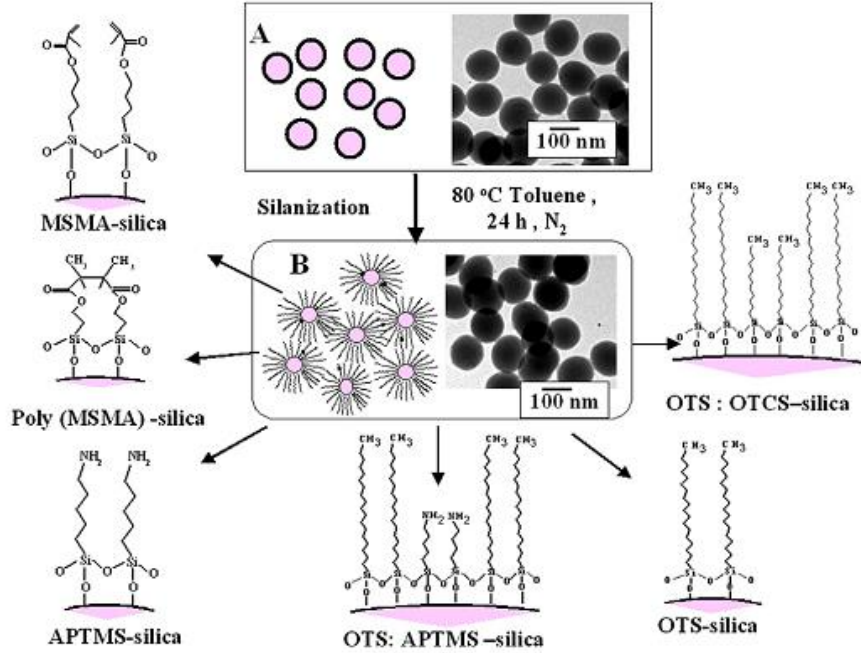


**Figure 11** Surface functional groups [35]

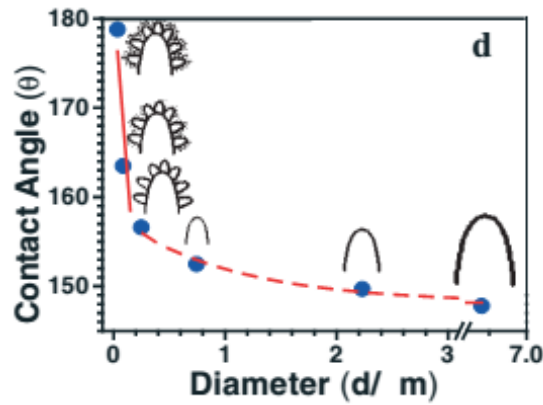


**Figure 12** The fitted curve of hierarchical structure effect to contact angle (contact angle, in degrees, against the mean outer diameter of protruding structures, in micrometers) [36]

Hierarchical structure, combination of micro- and nano-structure, is believed to be the optimal structure to create self-cleaning effect as it appears on lotus leaf [36,37]. Figure 12 shows that hierarchical (micro and nano) structure has higher WCA than microstructure only. Figure 13 shows the nanostructure and microstructure also have different effect on contact angle. Furthermore, the size of the hierarchical structure also affects the water contact angle of the surface. Figure 12 shows that smaller the diameter size of the peaks gives higher contact angle and the forming of nano details increases more the contact angle as well.

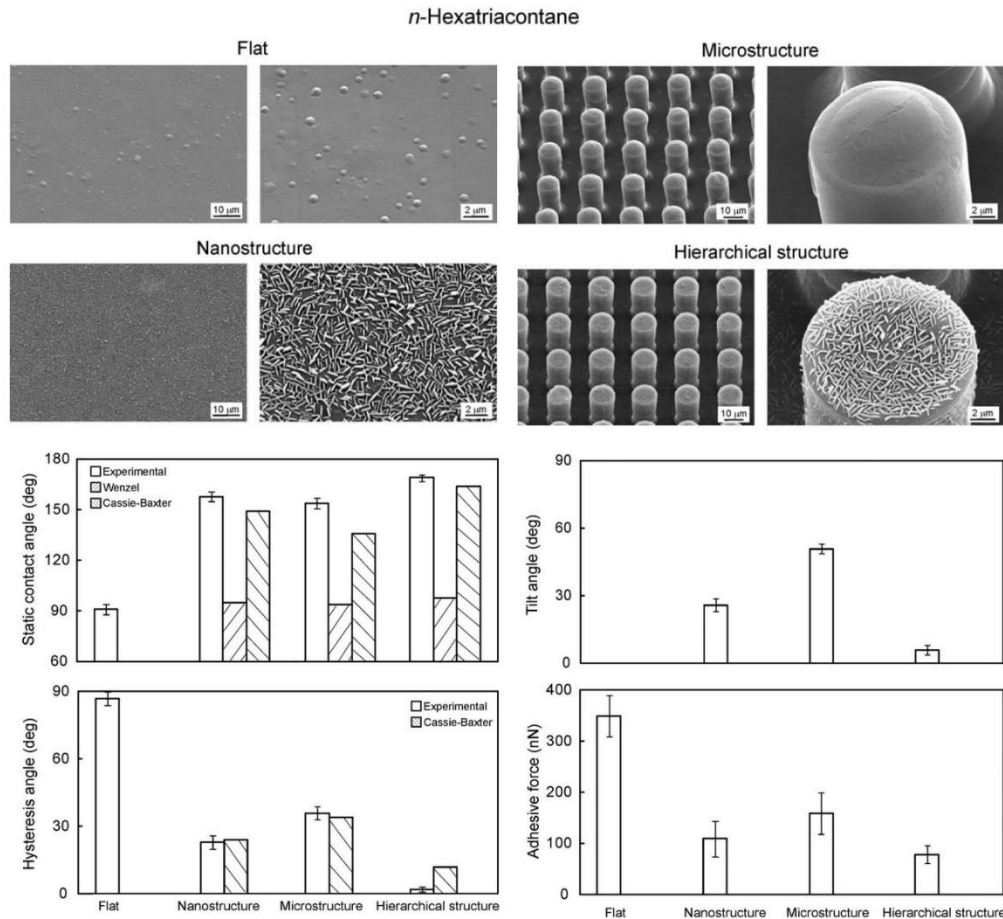


**Figure 13** variation of hierarchical structure *n*-hexatriacontane and its effect to water contact angle [37]

Some reports found that lotus wax materials is intrinsically hydrophilic and has  $74.0 \pm 8.5^\circ$  static WCA [38,39]. The lotus was heated until the nanofibers of lotus wax was disappeared. The contact angles of heated and unheated lotus were measured and compared. The heat treated lotus leaf has lower contact angle but still hydrophobic due to the remaining microstructure. Whereas, the smooth lotus wax has WCA lower than  $90^\circ$  which is categorized as hydrophilic. Therefore, the main factor to create self-cleaning effect is the structure of the surface.

### 1.6.3 Surface roughness effect to transmittivity

When light strikes a surface, it can be absorbed, transmitted, reflected, scattered or combination of them. The cover glass of photovoltaic, lime glass or polycarbonate sheet, is categorized as translucent material which is almost completely transmit the light. However, even translucent surface can possibly scatter or reflect the light reducing the amount of transmitted light. This transmissivity loss was found to be proportional to roughness of the surface as shown on Figure 14 [40–42].

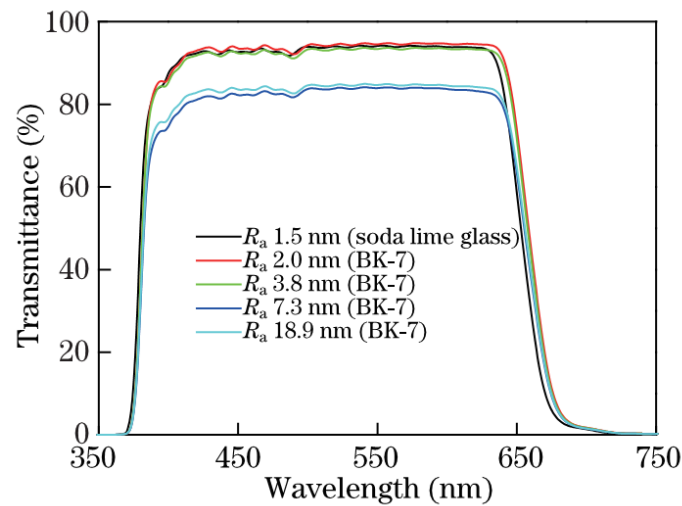


**Figure 14** Transmittance loss  $\text{SiO}_2/\text{TiO}_2$  film due to surface roughness [40]

Photovoltaic works by absorbing certain wavelength range of sunlight then turns it into electric charge. The majority of wavelength range is in visible light which between 400-750 nm which is within human eyes detection range as shown on Figure 15 [43]. Thus, the effective transparency of photovoltaic cover glass coating can be determined easily by human eye. If it has good transparency so it is good candidate to be a cover glass coating for photovoltaic. However, the accurate measurement for this transparency factor is needed by using photospectrometer. Since the application of self-cleaning can be extended to other applications such as windshields which needs to have visible light transparency, it is better to set the transparency range in visible light wavelength (400-750 nm).

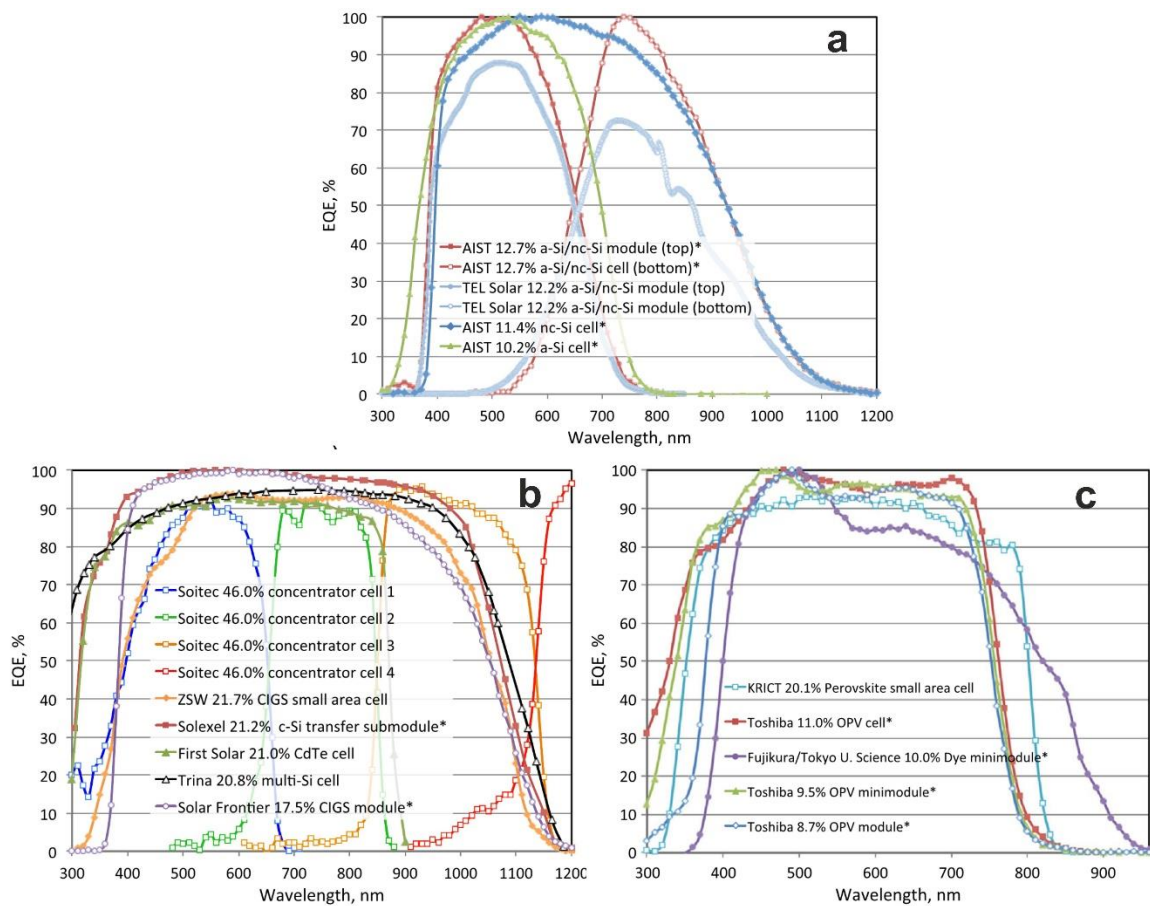


**Figure 15** Spectral response of various solar cell [43]

## 1.7 Surface Texturing

### 1.7.1 Modified silica nanoparticle

Gao *et al.* created superhydrophobic surfaces with hierarchical structure using PDMS and silica particle which is deposited onto glass slide [44]. The silica-PDMS film was deposited by using simple immersion method for 10 minutes. Two kinds of silica particles were used which is 7 nm and 14 nm size. Those two different particle sizes were studied to examine the effect on water contact angle. Concentration of silica particle was also varied to see the effect on water contact angle. Figure 16 shows different result of water contact angle by varying particle size and concentration of silica nanoparticles. The morphology of the surfaces was also studied using SEM image. The hysteresis of contact angle also shows similar trend that 14 nm particle sizes has 10°, 7 nm particle size has 40° and the combination of 14 nm and 7 nm has 30°.

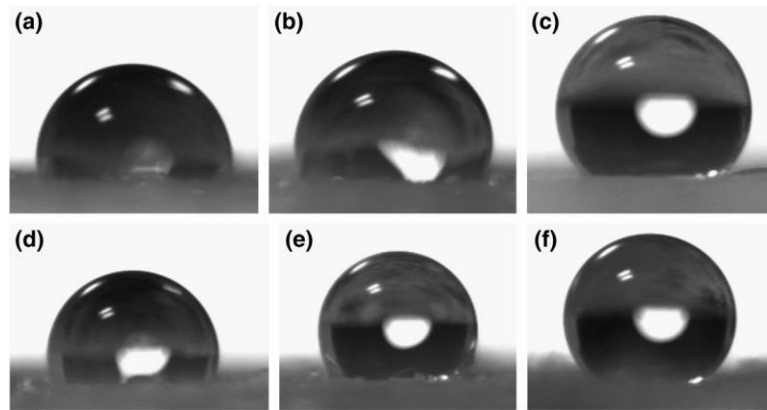


**Figure 16** water contact angle measurement of silica-PDMS surfaces with different particle size and concentration: (a) 7 nm and 0.5 % w/v: 93°, (b) 7 nm and 1.0 % w/v: 99°, (c) 7 nm and 2.0 % w/v: 130°, (d) 14 nm and 0.5 % w/v: 95°, (e) 14 nm and 1.0 % w/v: 103°, and (f) 14 nm and 2.0 % w/v: 147° [44]

From Figure 16, the use of 14 nm particle sizes has higher contact angle than the 7 nm particle size due to the regularity of its micro- and nano-structure as shown in Figure 17. Figure 17 shows SEM image of silica-PDMS surfaces with different particles size. These SEM images show that silica particle-PDMS surface with 7 nm has more groove and irregularity which minimizes the amount of air pocket to maintain the water droplet.

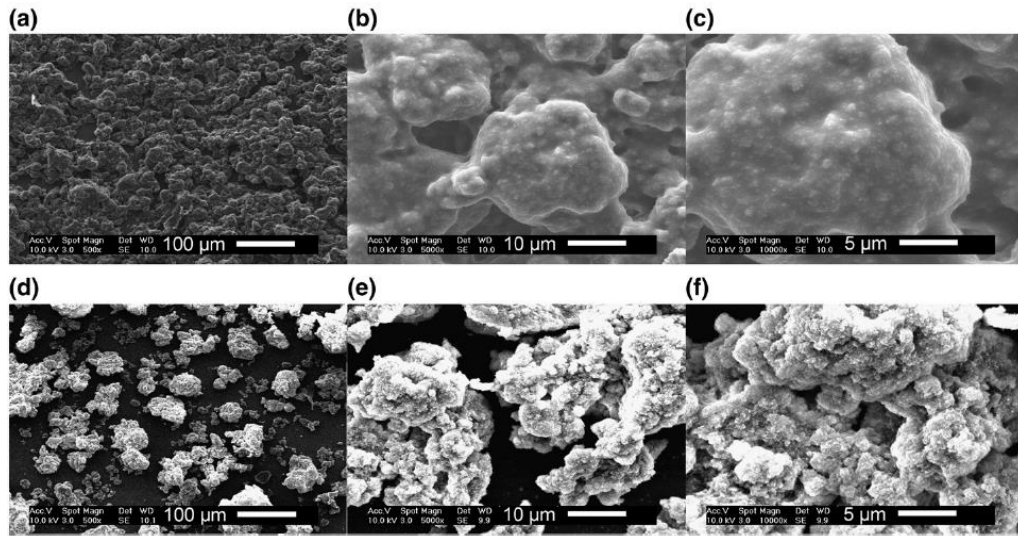


**Figure 17** SEM images of silica-PDMS surfaces with (a) 14 nm silica particle and 2.0 % w/v silica concentration and (b) 7 nm silica particle and 2.0 % w/v silica concentration [44]

Ke et al. developed superhydrophobic surface using silica particle and PDMS by drop-coating method [45]. Figure 18 shows the schematic process of drop-coating technique. First, octadecyltrichlorosilane (OTS) was grown onto silica particle surface. PDMS elastomer was prepared with weight ratio of curing agent to PDMS prepolymer of 1:10. Solution of 500 nm modified silica particle in ethanol then was dropped onto glass substrate. After the glass was dried, another 100 nm modified silica particle was dropped onto coated glass. After it was dried, it was cured at 100°C for 24 h. Finally, PDMS layer was dropped onto the surface then it was cured again.



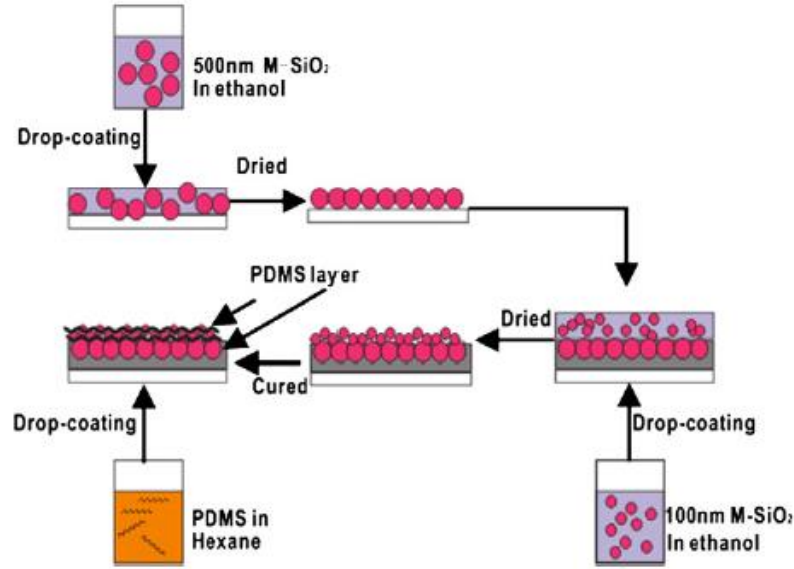


**Figure 18** illustration of drop coating procedure of superhydrophobic PDMS-based surface [45]

Modified silica particle which has OTS layer on its surface enhanced the deposition and adhesion of silica nanoparticles to the substrate which is indicated in the Figure 19 a and b. Curing temperature was also studied and showed that higher curing temperature enhanced the silica NP growth and increase its hydrophobicity as well. Figure 19 c, d and e show the SEM and water contact angle of PDMS/SiO<sub>2</sub> at different curing temperature.

Jin et al. had developed hierarchical-structured superhydrophobic surface using PDMS by casting and laser etching [46]. The procedure of this technique is shown in Figure 20. The micropillar is made by PDMS casting and the sub-micro-roughness is made by laser etching technique. The resulted surface texture of this technique is micro-submicro-nano structures which is generated by micropillars and submicro-nano grooves. Figure 21 a-c shows this hierarchical structure from micro- to nano-size. Figure 21 d shows the comparison between this laser-etched surface and flat PDMS surface. The static and dynamic water contact angle of this laser-etched PDMS are 162° and <5°.

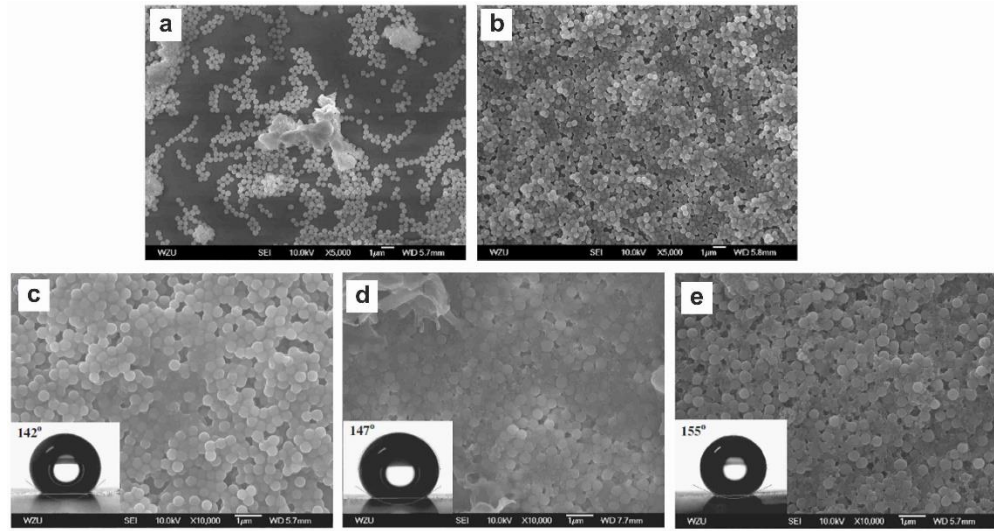


**Figure 19** Top side: SEM image PDMS/Silica coating on glass substrate using (a) unmodified 500 nm silica particle (b) modified 500 nm silica particle; bottom side: SEM image and water contact angle of PDMS/M-silica at different curing temperature: (a) 60°C, (b) 100°C, and (c) 140°C [45]

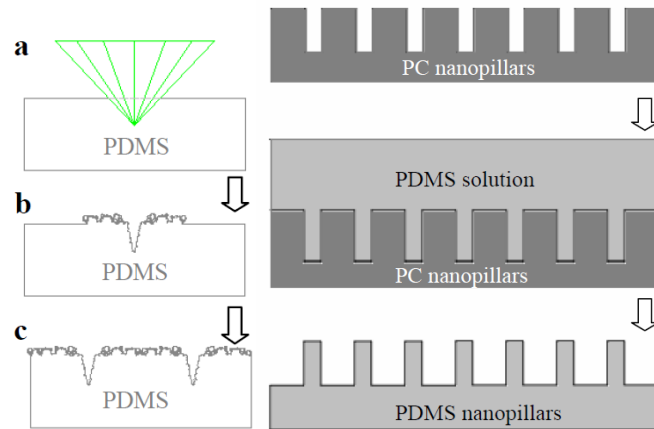


**Figure 20** (a) the schematic process of laser etching, (b) the schematic process of PDMS casting [46]

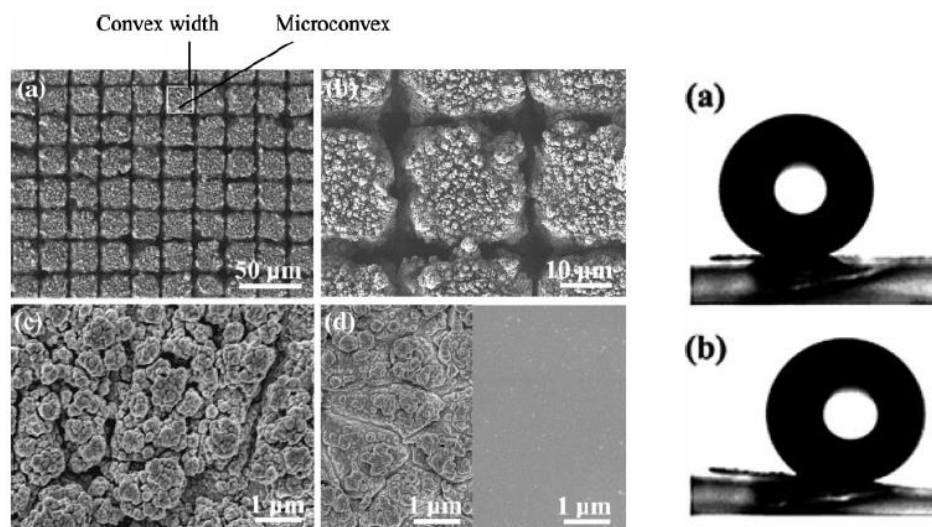


**Figure 21** (a) SEM micro image of laser-etched PDMS with (b, c) higher magnification; (d) comparison laser-etched and flat PDMS; (e) water contact angle:  $162^\circ$ ; (f) sliding contact angle: less than  $5^\circ$  [46]

### 1.7.2 Oil impregnated silica nanoparticle

Surface structure with hierarchical (nano-micro) structure plays very significant role to create self-cleaning effect referring to lotus leaf morphology by reducing contact area due to roughness effect [14,36,37,47–49]. However, roughness resulted from hierarchical structure gives drawback also to transmittivity especially for transparent glass applications. The light transmission was decreased due to higher roughness level of the surface which is indicated by rms (root mean square) value [40–42].

Silica nanoparticle is one of the most promising materials for producing self-cleaning surface since it is relatively transparent, easy to form hierarchical structure and able to carry various surface modifiers [50–53]. Self-cleaning silica nanoparticle was coated by modifying the silica surface by silane solutions such as octadecyltrichlorosilane and trichloro (1H, 1H, 2H, 2H-perfluorooctyl) silane or polydimethylsiloxane to increase the

hydrophobicity of the surface [45,51,52]. However, modified silica nanoparticle decreased the transmittivity of the glass substrate which is not good for transparent application such as photovoltaic and windshield [52,54]. Oil impregnation provides a good solution to the reduced transmittivity loss using index matching and it also has good durability to suspend on modified hydrophobic surface [55–60].

### 1.7.3 Silica Nanoparticle Aerogel deposition by Sol-gel process

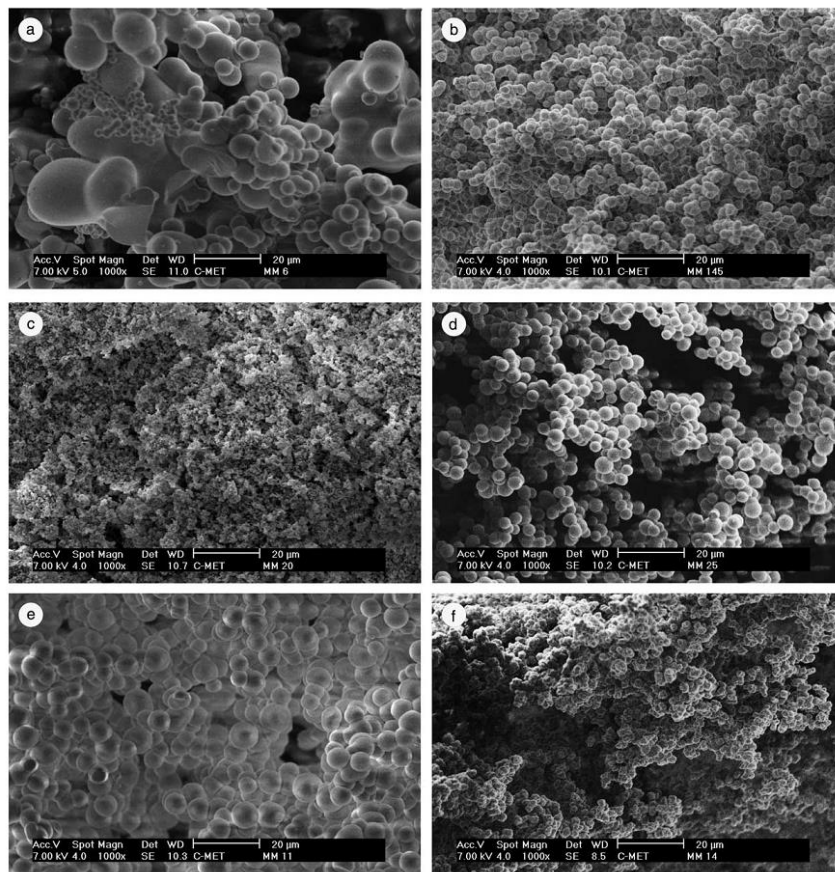


**Figure 22** SEM micrograph of the silica aerogel samples by different molar ratio: (a) and (b) are 0.043 and 0.35 molar ratio of  $\text{NH}_4\text{OH}/\text{MTMS}$ , (c) and (d) are 2 and 8 are molar ratio of  $\text{H}_2\text{O}/\text{MTMS}$ , and (e) and (f) are 3.5 and 14 are molar ratio of  $\text{MeOH}/\text{MTMS}$  [61]

Rao et al. [61] developed superhydrophobic silica aerogel based on MTMS precursor which has SEM images as shown on Figure 22. They made the silica aerogel by combining MTMS, H<sub>2</sub>O and methanol and varied its molar ratio. They used ammonium hydroxide (NH<sub>4</sub>OH) as catalyst of this solution to speed up the gelation time. The molar ratio of NH<sub>4</sub>OH/MTMS was also varied. The highest static contact angle resulted from this method is around 173°.

Latthe et al. [62] developed silica aerogel films by sol-gel process by using MTES, TEOS and water as precursor and NH<sub>4</sub>F as catalyst which has AFM images as shown on Figure 23. The molar ratio of MTES/TEOS was varied from 0 to 0.43. They studied also about frictional force of each sample. They obtained the sample with 160° static WCA, 3° sliding angle and 5.12 µN frictional force.

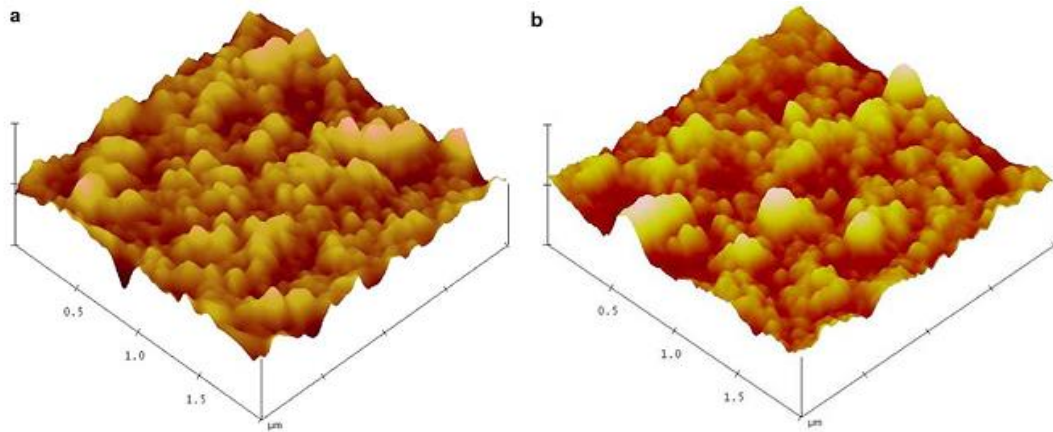


**Figure 23** AFM image of silica aerogel film with (a) 0 and (b) 0.43 molar ratio of MTES/TEOS

[62]

#### 1.7.4 PDMS double casting

Stanton et al. [63] developed simple PDMS casting technique by using SiC sand paper as casting template. They investigated the roughness created by this method and then measure the static and dynamic contact angle of PDMS surface texture. Figure 24 shows the schematic procedure of this technique which is just using SiC sand paper as a template then molding and demolding the PDMS on it. The texture resulted from this method is negative texture of SiC paper since it was just single casting.

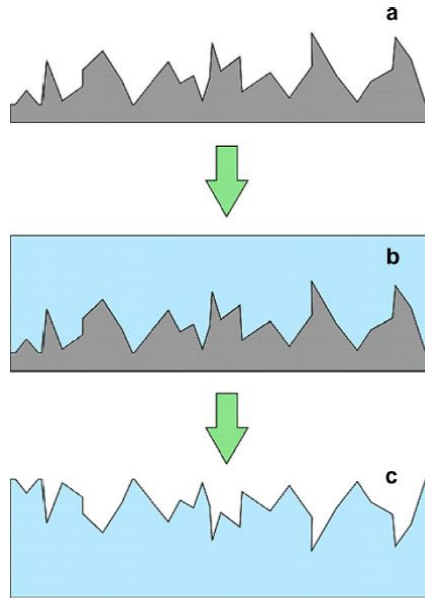


**Figure 24** Schematic of PDMS casting process using SiC paper template [63]

The hydrophobicity of this approach was quite promising which is  $153.5^\circ$  which can be categorized as superhydrophobic surface, see Figure 25. It proves that this microroughness can lead to superhydrophobicity as good as nanoroughness surfaces. However, its sliding contact angle is still high (around  $26^\circ$ ). For comparison, sliding angle of flat PDMS surface is around  $22^\circ$ . Furthermore, if compared to lotus leaf contact angle hysteresis which is

around  $2^\circ$ , it is much larger [64]. It shows that this PDMS surface has high adhesion force.

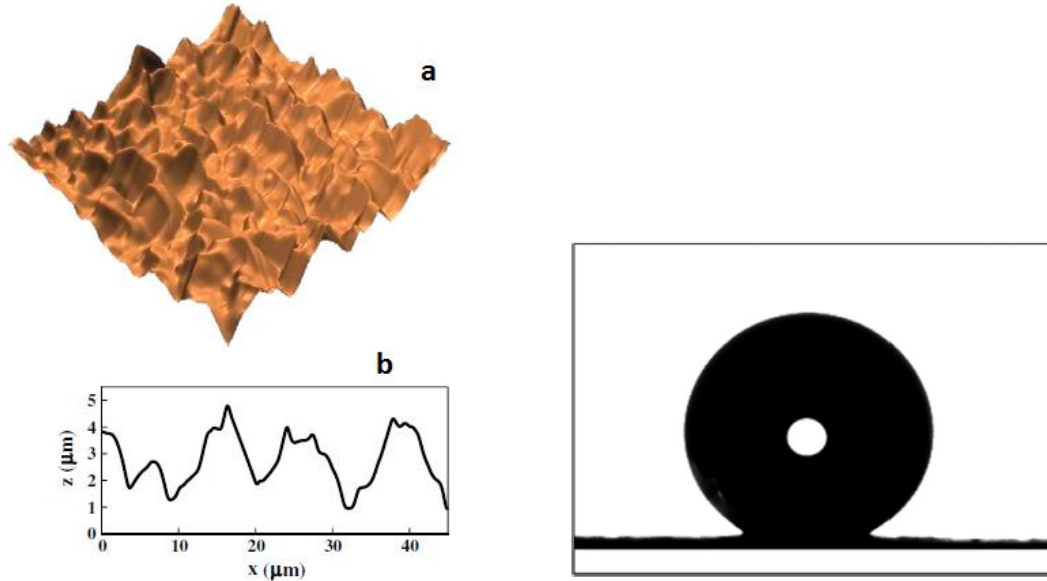


**Figure 25** (a) 3D AFM image of PDMS surface (b) vertical roughness of PDMS surface, (c) water contact angle measurement of PDMS surface

Manhui Sun et al. studied about casting of lotus leaf on PDMS surface [65]. They did double casting to create positive replica which has similar nanostructure of lotus leaf. They used PDMS for the first replica or negative replica. Before doing the casting, anti-stick layer which is trimethylchlorosilane (TMCS) monolayer was deposited onto the master to minimize surface transfer and asperities breakage. Anti-stick layer is widely used in PDMS casting especially for double casting method to maintain the stability of its master template. Other kinds of anti-adhesion layer is being used are Parylene C [66], perfluorodecyltrichlorosilane (PFDTs) [67], and hydroxypropylmethylcellulose (HPMC) [68].



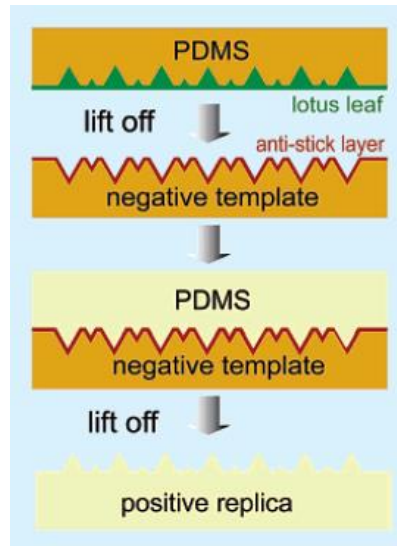


**Figure 26** illustration of nanocasting procedure of superhydrophobic PDMS surface [65]

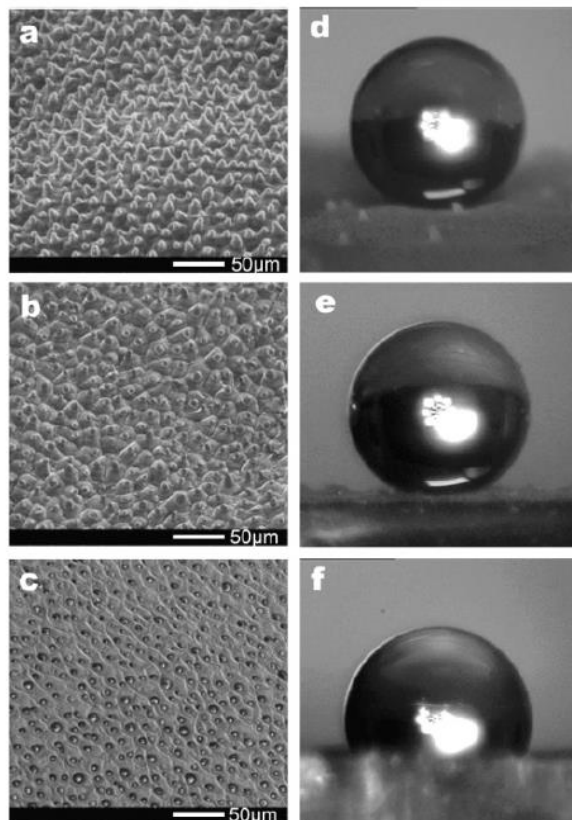


**Figure 27** SEM and water contact angle image of (a, d) lotus leaf, (b, e) positive replica PDMS surface, (c, f) negative replica PDMS surface [65]



The schematic of nanocasting procedure is illustrated by Figure 26. The resulting surface produced by double casting is positive texture which is similar to the master template. The SEM image master template, negative template and positive replica are shown in Figure 27 which also includes measurement of static contact angle. It shows that negative template does not provide good hydrophobicity for templating lotus leaves since its contact angle is lower than lotus leaf itself.

## 1.8 Dynamic dust cleaning

### Gravitational Force

One of the force that is acting on particle adhesion onto the surface is gravitational force which is derived by this familiar equation:

$$F_g = m \cdot g = \frac{4}{3}\pi R^3 \rho g \dots\dots\dots 10$$

Where m is mass of the particle,  $\rho$  is density of the dust particle, and g is gravitational acceleration.

### Lift Force (inertial force and shear stress)

Lift force can be caused by inertial force (Figure 28 b). This inertial lift force will cause torque force on the particle with point contact between particle and wall as the center of rotation. Then another lift force which is caused by flow shear stress also plays torque force on the particle (Figure 28 c). Combination of that torques will lift the particle from the surface.

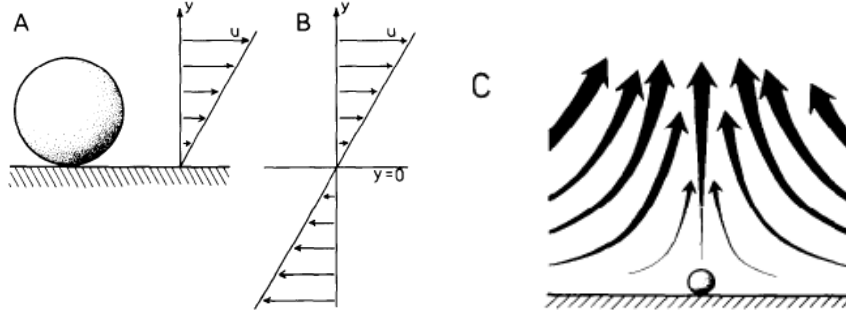


**Figure 28** Hubbe's model on the lift force [69]

Leighton et al. [70] and Cherukat et al. [71] derived lift force from navier-stoke equation for spherical shape particle where particle is almost touching the surface and reynolds number below unity. Then Zhang et al. [5] simplified this equation to be:

$$F_L = \frac{9.22\mu^2}{\rho}(Re^*)^3 \dots\dots\dots 11$$

Where  $\mu$  is dynamic viscosity of fluid and  $Re^*$  is Shear Reynold number which is defined by:

$$Re^* = \frac{Ru^*}{\nu} \dots\dots\dots 12$$

Where  $\nu$  is kinetic viscosity and  $u^*$  is friction velocity:

$$u^* = \sqrt{\frac{2\tau}{\rho}} \dots\dots\dots 13$$

Where  $\tau$  is shear stress.

White [72] has derived shear stress of rotating disk system from navier-stoke equation and using numerical method to solve the partial differential navier-stoke equation.

$$\tau_o = \rho r G_o' \sqrt{\nu \omega^3} \dots\dots\dots 14$$

Where  $\tau_o$  is shear stress at the wall ( $y=0$ ),  $r$  is the position of particle from the center of rotation,  $G'_o$  dimensionless constant at the wall ( $G'_{z=0}=-0.61592$ ) and  $\omega$  is the angular velocity of the disk.

### Drag Force (pressure and shear)

Drag force can be divided into three types, first is pure pressure drag force when the area normal to the flow is relatively wide, secondly the pure shear friction drag force which is caused by friction force of flow to parallel area of the particle, the last one is the combination of pressure and shear drag force. The drag force acting on spherical shape particle can be considered to be the third type which is combination of pressure and shear drag force.

O'Neill et al. [73] and Goldman et al. [74] have formulated the drag force equation which is derived from Navier-Stoke equation.

$$F_D = 10.2\pi\mu Ru \dots\dots\dots 15$$

Where  $\mu$  is the flow velocity.

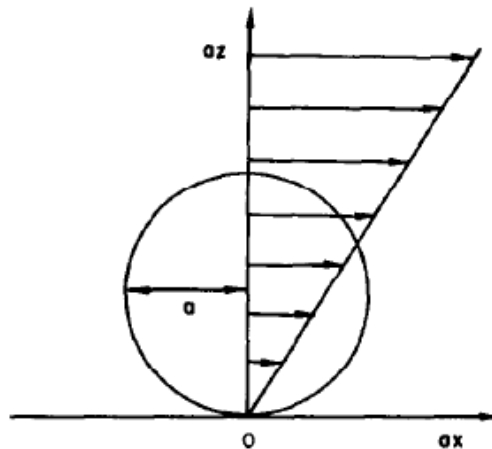


**Figure 29** Flow profile acting on the spherical particle [73]

### **Centrifugal Force**

Centrifugal force also affects the dust adhesion on rotating disk system since it gives force to move from center of rotation to the edge of disk which is function of rotational velocity ( $\omega$ ), mass ( $m$ ) and radius ( $r$ ).

$$F = m\omega^2 r = \frac{4}{3}\pi R^3 \rho \omega^2 r \dots\dots\dots 16$$

### **Friction Force**

Friction force comes since there are a force which is reverse direction of particle movement as a function of coefficient of friction ( $\mu$ ) and normal force ( $N$ ).

$$F_f = \mu N = \mu F_g \dots\dots\dots 17$$

## **1.9 Dust Characterization**

One report provided dust characterization from a desert site in Kuwaiti/Iraqi border during June 2004 [75]. This findings shows that most of the dust micro-particulates are porous silica core coated by several type of clays such as calcium carbonate ( $\text{CaCO}_3$ ), magnesium sulfate ( $\text{MgSO}_4$ ) and metallic compounds. The details of elemental composition findings are shown in Figure 30.

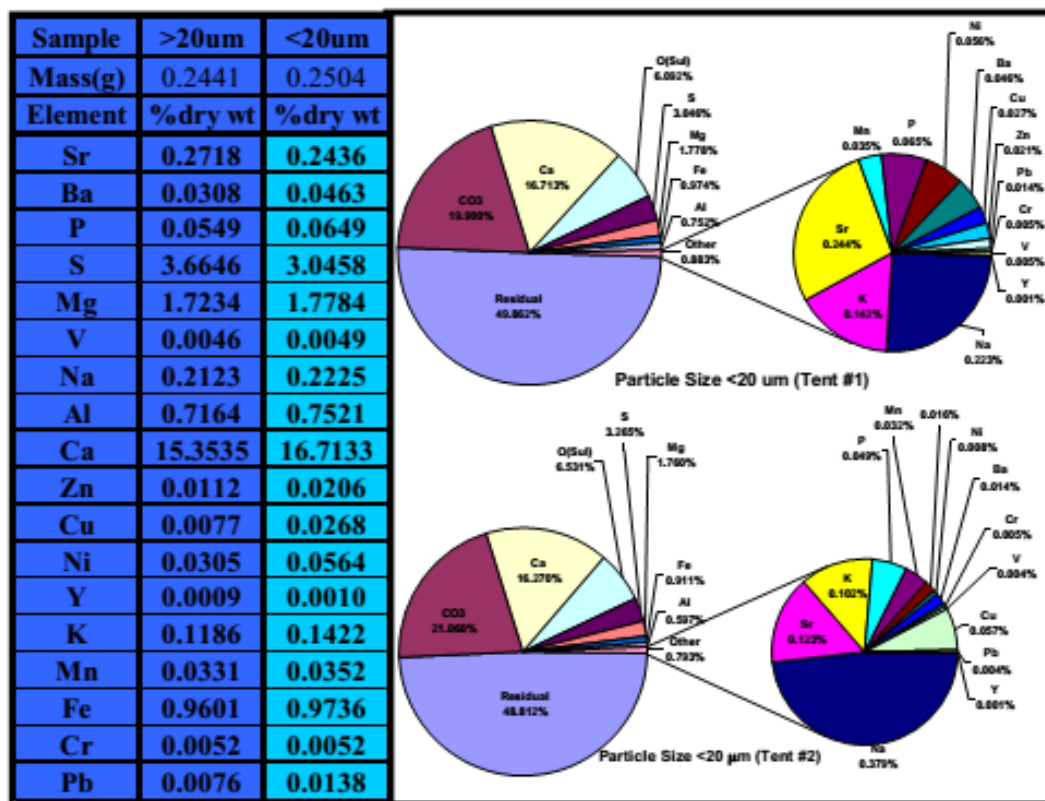


Figure 30 Elemental Composition of Dust Particle in Kuwait/Iraq [75]

Table 1 Average relative composition (atomic percent) of the particle classes

Class name	Na	Mg	Al	Si	P	S	Cl	K	Ca	Ti	Cr	Mn	Fe	Co	Cu
Iron-rich	4	3	12	16	2	3	1	1	2	4	2	1	48	1	1
Titanium-rich	2	2	9	14	1	2	1	1	1	59	1	1	5	1	1
Carbonates	3	9	6	10	1	2	1	1	62	1	1	1	2	1	1
Other calcium-rich	4	6	12	24	3	3	1	2	35	1	1	1	4	1	1
Gypsum	4	2	3	6	2	38	1	1	37	1	1	1	2	1	1
Halite	47	3	2	2	1	3	38	1	1	0	0	0	1	0	0
Quartz	2	2	6	81	2	1	0	1	1	1	0	0	2	0	0
Silicates	4	5	26	46	2	2	1	3	2	1	0	1	6	1	0
Sulfate silicate mixtures	14	6	15	20	4	14	6	3	5	2	2	2	5	2	1
Sulfates	31	8	5	5	6	24	3	3	6	2	2	2	2	2	1
Total	5	5	21	45	2	3	1	3	6	1	1	1	6	1	0

Another report studied dust composition from Saharan desert reaching Izana (Tenerife, Spain) [76]. The dust composition was classified in several kind of minerals and its elemental composition. Table 1 shows the detail of elemental composition of each mineral

types in atomic percent. It shows that the majority elemental composition existed in each dust minerals are silicon and aluminum.

In conclusion, the dust adhesion on surface was caused by van der Waals force between particle and flat surface and then a modification was given by Rumpf-Rabinovich since the existence of roughness affects the adhesion force. Surface texturing is believed to be able to reduce the adhesion force of dust particle by creating hierarchical structure which reduces contact of solid-liquid phase. The surface resulted from this surface texturing was called self-cleaning surface. However, the majority of self-cleaning surfaces were relatively opaque since increasing of roughness decreased the transmittivity due to surface scattering. There are several surface texturing methods which produce self-cleaning surfaces without reducing transmittivity such as modified silica NP deposition and PDMS casting. After all, the active dust cleaning is needed due to lack of water resources inside Saudi Arabia. Centrifugal force action by dynamic rotation is a good solution since it produces high magnitude of force to remove dust accumulation.

## **CHAPTER 3**

### **MATERIALS AND METHODS**

#### **1.10 Materials**

##### **1.10.1 Oil impregnated silica nanoparticle and sol-gel process**

One of the experimental study aims at design and engineering of surface texture that will enhance the self-cleaning characteristics of glass and PC sheets. In preparation to do that and as a result of the extensive literature review several materials were procured from different sources. Colloidal silica PL-3 (30 nm particle diameter size, 20% silica weight content), PL-7 (75 nm particle diameter size, 23% silica weight content) and PL-20 (220 nm particle diameter size, 20% silica weight content) were obtained from FUSO chemical, Japan. Trimethylchlorosilane (TMCS), methyltrimethoxysilane (MTMS), ethanol and hexane were obtained from Fluka Chemika, Switzerland. Deionized (DI) water was obtained by deionizing tap water using Siemens ultra-clear reverse osmosis water purifier. Sulfuric acid 95-97% was obtained from Sigma Aldrich, United States. Hydrogen peroxide 30% was obtained from Carlo Erba Reagents, Italia. 1H, 1H, 2H, 2H-perfluorooctyltrichlorosilane (PFOTS) 97% was obtained from Alfa Aesar, United States. Krytox lubricants was obtained from Dupont, United States. Glass slides was obtained from Corning, United States.

### 1.10.2 PDMS double casting

The experiments for texture duplication of a Lotus leaf and rice leaf were accomplished using double casting technique. The material used for casting/molding is Sylgard 184 silicone elastomer kit (Polydimethylsiloxane (PDMS) and its curing agent). It was obtained from Dow Corning, United States. Surface modification is done using two materials. One is Trimethylchlorosilane, TMCS, ethanol and hexane were obtained from Fluka Chemika, Switzerland. The other material is 1H, 1H, 2H, 2H-perfluorooctyltrichlorosilane (PFOTS) 97%, which was obtained from Alfa Aesar, United States. Krytox lubricants was obtained from Dupont, United States. Deionized (DI) water was obtained by deionizing tap water using Siemens ultra-clear reverse osmosis water purifier.

### 1.10.3 Dynamic dust cleaning

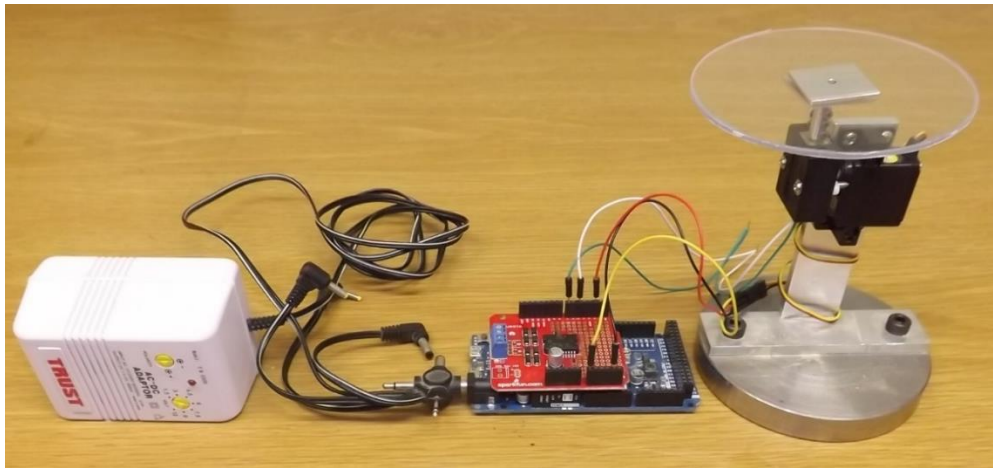


**Figure 31** Rotational dust cleaning setup

Dynamic rotational dust cleaning setup components were bought from Sparkfun, US. The components are Arduino due and motor shield as controller, DC motor to rotate the polycarbonate (PC) disc, and direct current (DC) adapter. The source code made using Processing software as interface in the computer to set the parameter and start the rotation.



The PC disc was made using computer numerical control (CNC) machine in mechanical workshop. Figure 31 shows the physical appearance of the dynamic rotational dust cleaning setup.

## **1.11 Methods**

### **1.11.1 Oil impregnated silica nanoparticle**

#### **3.2.1.1 Glass pre-treatment with Piranha**

A 23 x 23 mm microscope glass slides were washed with soap, distilled water and acetone successively. The cleaned glass slides then were dried at room temperature and then soaked into piranha solution. Piranha solution preparation is done inside fume hood and the fan is on. Safety procedure of wearing hands glove is compulsory. Piranha solution was prepared by mixing 1:7 volume ratio of hydrogen peroxide to sulfuric acid. Hydrogen peroxide was poured first in the beaker glass then adding sulfuric acid by drop wise. The solution was then left for 1 hour to let the heat escape due to exothermic reaction. The glasses were soaked in piranha solution for 1 hour to let the solution react with surface and create –OH functional group. The treated glasses then were rinsed with DI water several times and dried in open atmosphere stream. The used piranha solution was neutralized by adding several grams of sodium bisulfite and left for 1 hour to release the heat. The neutralized piranha solution then was then disposed in inorganic waste container.

#### **3.2.1.2 Silica nano particle deposition**

A simple dip coater machine was built using Arduino microcontroller, stepper motor, acrylic stand, cotton thread and paper clip. Simple source code was created using

Processing software to control Arduino microcontroller by filling dip coating parameters, e.g. withdrawal speed and immersing time, through computer.

Each colloidal silica nano particles were diluted by ethanol with 1:20 volume ratio. The diluted colloidal silica particle was then homogenized in ultrasonic bath for 15 minutes. The treated glass was dipped in a mixed size (explain what is mixed size here) colloidal silica solution for 5 second and 1 mm/s withdrawal rate. The coated glass was then kept in room temperature for 1 hour to let the silica nanoparticles arrange their structure (what is the mechanism of self-arranging). The final step is sintering where the silica coated glasses were sintered in the furnace for 2 hours at 200°C.

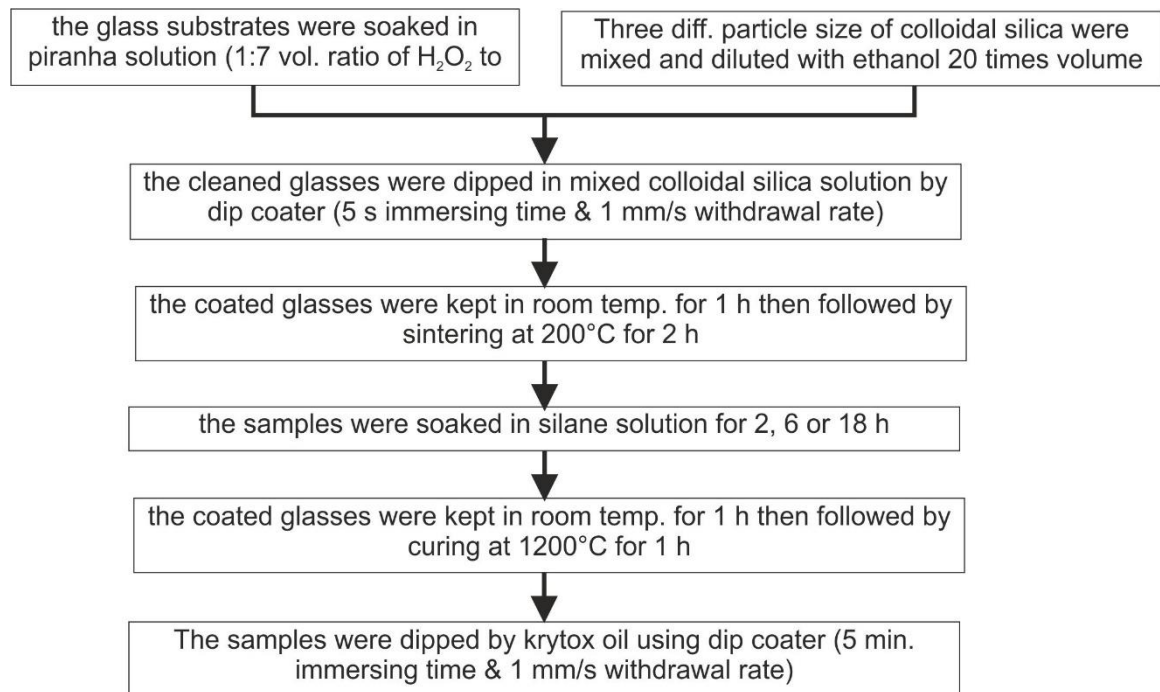


**Figure 32** oil impregnated silica nanoparticles procedure

### 3.2.1.3 Silane surface treatment/modifying

TMCS and PFOTS solutions were diluted in hexane to get 5% and 2% volume ratio respectively. The dilution process was done by stirring the mixed solution for 15 minutes and then dispersed in ultrasonic bath for 15 minutes. The coated glasses were soaked in the diluted silane solution. The soaking time was varied by 2, 6 and 12 hours. The silane-soaked samples were then washed by hexane solution to remove unreacted silane. The samples were then kept in room temperature stream to let the silylating agent develop its self-assembly monolayer (SAM) structure. The silylated samples were heat treated in furnace for 1 hour at 100°C to evaporate the liquid solution trapped inside the coating materials and to improve the crystallization as well.

#### 3.2.1.4 Oil impregnation

Krytox fluorinated oil was used to impregnate the silica particles textured surface after the silane treatment. The surface modified samples were dipped in fluorinated lubricant for 5 minutes and retracted with 1 mm/s rate. The lubricant was found to have good adherence to the surface due the strong bonding to carbon groups of monolayer silylating agent. The whole procedure was shown on Figure 32.

### **1.11.2 PDMS double casting**

#### 3.2.2.1 PDMS Casting (negative replica)

PDMS monomer and its crosslinking catalyst were prepared using mixing ratio of 10:1 by weight. The mixture was stirred in disposable plastic cup using disposable plastic spoon. The mixture was then placed inside desiccator and vacuumed for around 1 hour to remove trapped air bubbles inside the mixture. The leaf sample was placed on the bottom of casting container and then the PDMS was poured on top of it. The container was placed inside the

desiccator and vacuumed again for 1 hour to remove air bubbles create at casting process. The PDMS was kept inside desiccator for 2 days and then cured at 65°C for 2 hours. The PDMS was then peeled off gently from the leaf substrate. The result of these steps is the negative replica.

PDMS negative replica was placed inside the desiccator again. Then few drops of TMCS was dropped on it and then vacuumed for 1 hour to enhance TMCS penetration on every fine details of negative replica surfaces. The samples was left for one night to let TCMS form bonding with PDMS surfaces. The TMCS-coated PDMS negative replica was rinsed with acetone to remove unreacted TMCS. The negative replica then was cured in the oven at 100°C for 1 hour.

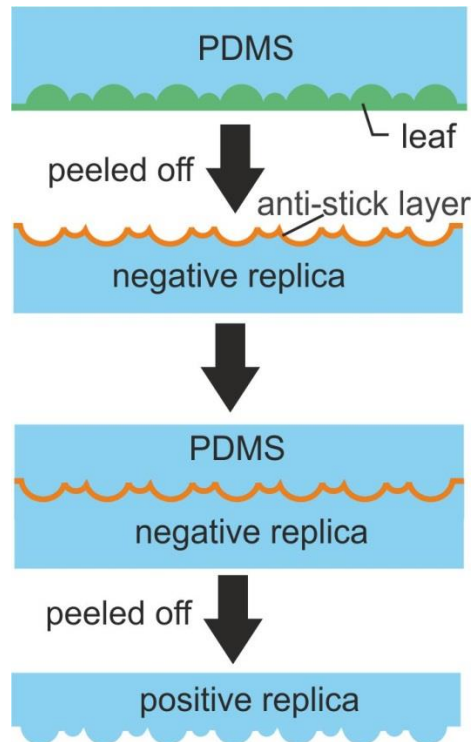


**Figure 33** illustration of PDMS double casting process

#### 3.2.2.2 PDMS Casting (positive replica)

The same procedure as that described for the negative replica was repeated but with the negative replica as the initial substrate. As a result, a replica of the initial leaf is produced.

### 3.2.2.3 Silane surface modifying

It is similar to forming anti-stick monolayer which used TMCS by dropping TMCS solution on top of the surface and leaving it for one night and then washing it with acetone. The washed PDMS replica then was sintered for 1 hour at 100°C. Silane modifier was applied on the surface to increase the hydrophobicity of the surface. It will help to adhere oil strongly also for oil impregnation step. The whole procedure was illustrated on Figure 33.

### 1.11.3 Silica aerogel nanoparticle deposition by sol-gel dip-coating

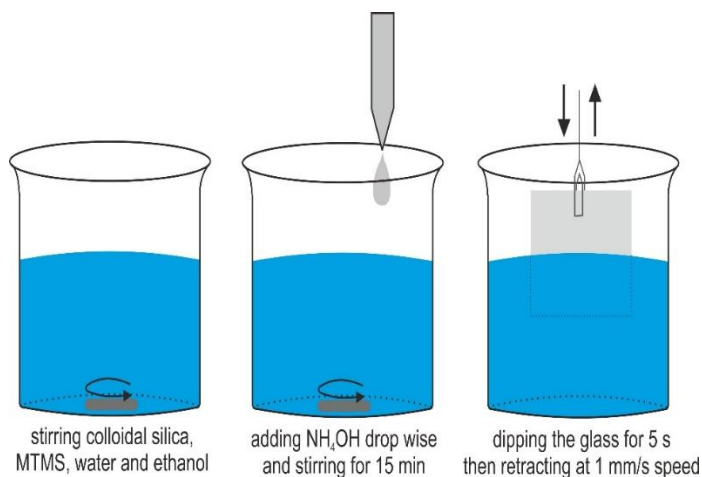


**Figure 34** illustration of Sol gel silica procedure

The glass was prepared by piranha solution as mentioned in 3.2.1 section. Colloidal silica, MTMS, methanol, DI water and ammonium hydroxide were stirred using magnetic stirrer inside fume hood for 15 minutes as shown on Figure 34. The volume ratio of colloidal silica, MTMS, methanol, DI water and ammonium hydroxide was varied. After the stirring

was finished, the glass substrate (25 x 25 mm<sup>2</sup>) was dipped in that solution using dip coater (5 s immersing time and 1 mm/s withdrawal rate). The coated glasses then were kept in room temperature for 1 hour in order for drying and letting the silica arrange its structure. The dried glasses were sintered in furnace at 150°C for 1 hour.

#### **1.11.4 Dynamic Dust Cleaning**

The forces calculation was done by Matlab 2014b edition software. The parameters was varied are rotational speed ( $\omega$ , rad/s), dust radius ( $R$ ,  $\mu\text{m}$ ) and particle distance from center of rotation ( $r$ , cm). All of the forces which are adhesion, gravitational, lift, drag, friction and centrifugal forces were calculated by varying those parameters. The parameters were varied in the range 0-100 rad/s, 0-10  $\mu\text{m}$  and 0-10 cm for  $\omega$ ,  $R$  and  $r$  respectively. All the result then were plotted by Matlab software also. The experimental work was done to validate the force calculation by rotating the dust with different rotational speed. The dust was accumulated on the PC surface then the dust weight before and after rotation were measured by balance.

### **1.12 Characterization**

#### **1.12.1 Scanning Elelectron Microscope (SEM)**

The morphologies were observed by TESCAN LYRA3 field emission gun scanning electron microscope (FEG-SEM) equipped with energy dispersive x-ray spectroscopy (EDS) detector. The samples were coated with gold using a Crossington sputter coater 108auto for 40 seconds. Figure 35 shows the physical appearance of TESCAN LYRA3 field emission gun scanning electron microscope.

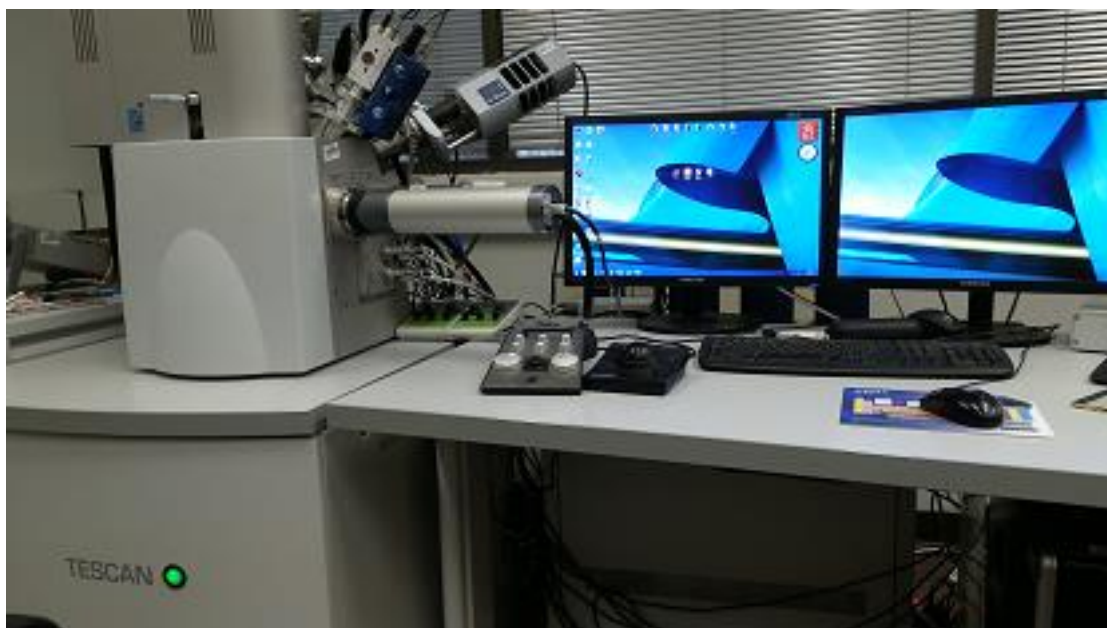


**Figure 35** TESCAN LYRA3 FEG-SEM



**Figure 36** JEOL Scanning Electron Microscope

In addition, the morphology of several samples were also observed using JEOL JSM-6460LV scanning electron microscope (SEM) equipped with EDS detector. The samples

were coated with gold using a JEOL ion sputter JFC-1100 for 8 minutes at 8 mA before imaging. Figure 36 shows the physical appearance of JEOL JSM-6460LV scanning electron microscope.

### **1.12.2 Ultraviolet Visible (UV-Vis) light Spectrophotometer**

The transmittivity of the surfaces were measured by JENWAY 6705 ultraviolet visible (UV / Vis) light Spectrophotometer at 300 – 900 nm wavelength. The light transmittance on air was used as reference and the coating transmittivity was measured on glass substrate. Figure 37 shows the physical appearance of UV-Vis light spectrophotometer.

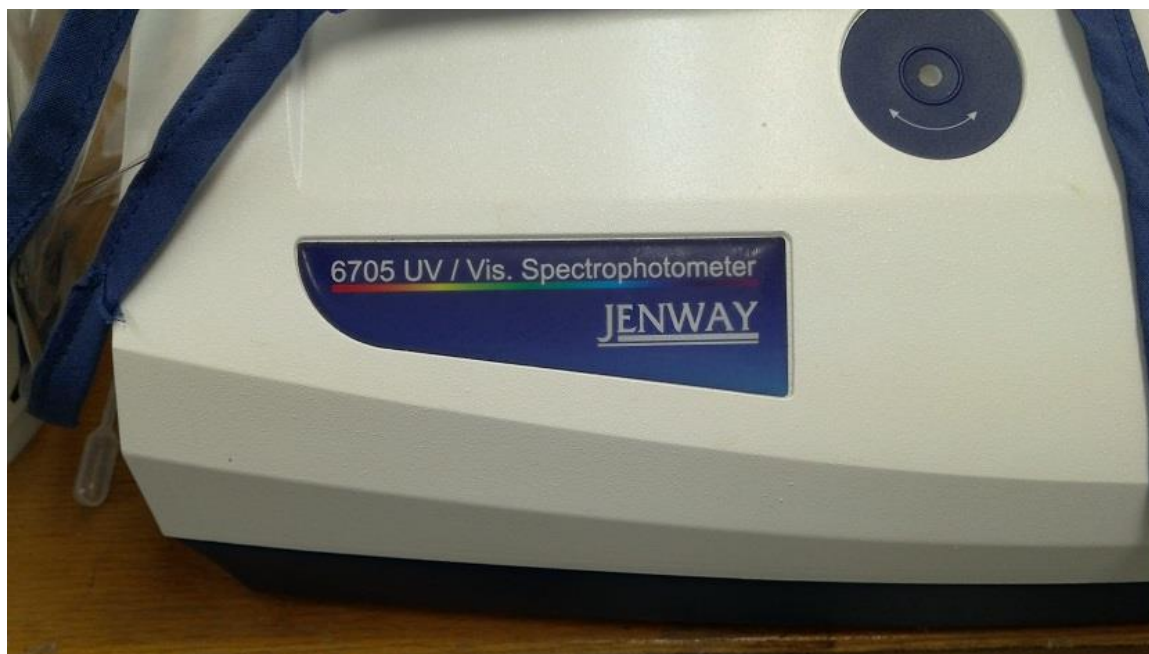


**Figure 37** JENWAY 6705 UV-Vis Spectrophotometer

### **1.12.3 Water Contact Angle Measurement**

The static water contact angle (WCA), hysteresis and sliding angle (SA) were measured using Kyowa DropMaster DM-501. The static WCA was measured by sessile drop method and the hysteresis was calculated by expansion/contraction method. The deionized water



(DI) water was used for all the measurement. The water droplet was dropped manually using micropipette to get accurate droplet volume. Figure 38 shows the physical appearance of Kyowa DropMaster DM-501.

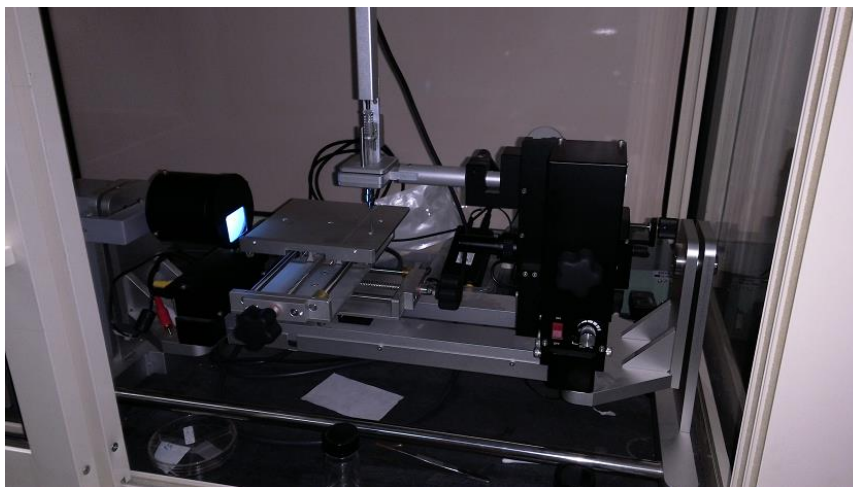


**Figure 38** Kyowa DM-501 contact angle meter

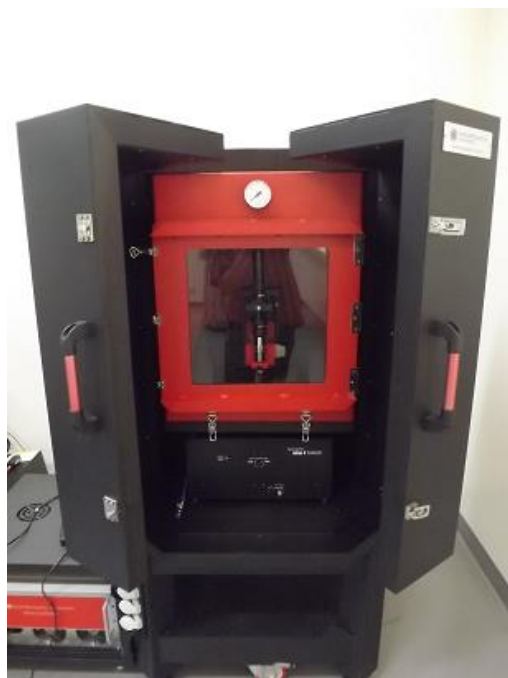


**Figure 39** Nanomagnetics Instrument high performance atomic force microscope (hpAFM)

#### **1.12.4 Atomic Force Microscope**

The topography of the surfaces were observed with Nanomagnetic Instrument high performance atomic force microscope (AFM) by tapping mode. Nanosensors PPP-NCLR scanning probe was used as AFM tip. The maximum scanning area of hpAFM is 90 by 90  $\mu\text{m}^2$ . The roughness value of the surface was measured as average roughness in area and line. Figure 39 shows the physical appearance of Nanomagnetic Instrument high performance atomic force microscope.

#### **1.12.5 Particle Size Analyzer**

Particle size of the dust samples were characterized by Microtrac S3500 Laser Diffraction Analyzer. The dust was analyzed dry condition. The dust particle size was quantified in three different distribution: number, volume and area. The system is able to measure particle size in the range of 0.25 - 2800  $\mu\text{m}$ . Figure 40 shows the physical appearance of Microtrac S3500 Laser Diffraction Analyzer.



**Figure 40** Microtrac S3500 Particle Size Analyzer

## CHAPTER 4

### RESULTS AND DISCUSSION

#### 1.13 Dust Particle Characterization

Dust samples from outdoor laboratory was characterized by Microtrac S3500 particle size analyzer in dry condition. The results of particle size distribution are shown in Figure 41 and its statistical calculation in the volume distribution has really different result compared to number and area distribution. It is due to the volume distribution calculation counts the total volume size of the particle. The number of big particle might be just small number, but due to its big size it has significant impact to pull the mean value. In term of adhesion force analysis also it has big meaning. Basically, the adhesion force, which is dominantly Van Der Waals force in micron size particle, was function of surface area. The big particle does not mean has bigger adhesion than smaller size unless the surface contact area is larger. Based on this analysis, the dust particle sizes are  $0.756 \pm 0.225 \mu\text{m}$ ,  $4.6 \pm 3.9 \mu\text{m}$  and  $16.83 \pm 12.87 \mu\text{m}$  based on number, area and volume distribution respectively as shown on Table 2.

The volume distribution has really different result compared to number and area distribution. It is due to the volume distribution calculation counts the total volume size of the particle. The number of big particle might be just small number, but due to its big size it has significant impact to pull the mean value. In term of adhesion force analysis also it has big meaning. Basically, the adhesion force, which is dominantly Van Der Waals force

in micron size particle, was function of surface area. The big particle does not mean has bigger adhesion than smaller size unless the surface contact area is larger.

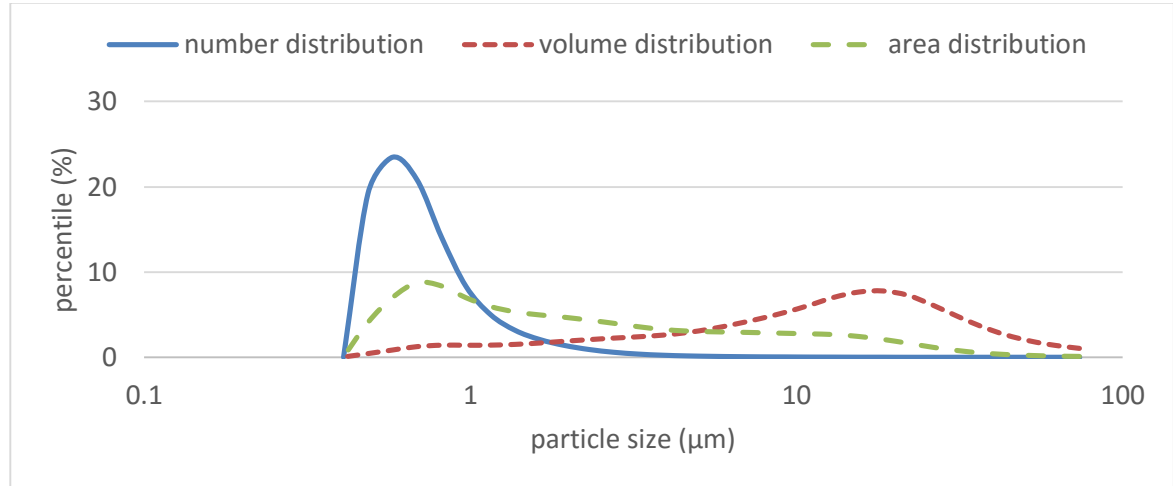


**Figure 41** The dust particle size distribution was presented in number, area and volume percentile

The SEM micrograph validated the particle size analysis results. As shown in Figure 42 there are several big particles with sizes of around 5 – 20  $\mu\text{m}$  and they cover the majority of area in the image. However, in term of particle number, smaller particles in range around 0.5 – 2  $\mu\text{m}$  have larger number than bigger particles. From Figure 38 shows many smaller particles are agglomerated and attached to the bigger particles. These agglomerated particles of small particle form some of the big particles and as a result give more roughness effect. This roughness reduces the surface contact area of the big particles. From these findings big particle should be have weaker adhesion force and easier to remove.

**Table 2** Mean, standard deviation and peak value of dust particle dust distribution

	number	area	volume
Mean ( $\mu\text{m}$ )	0.756	4.6	16.83
Standard deviation ( $\mu\text{m}$ )	0.225	3.99	12.87
Peak Value ( $\mu\text{m}$ )	0.69	1.598	12.46

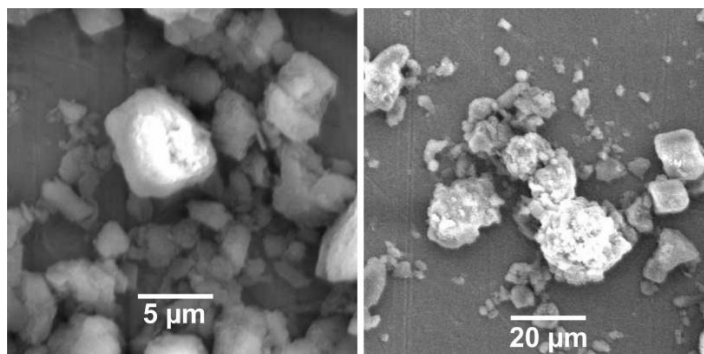


**Figure 42** SEM micrographs of dust particle

EDS analysis was also performed to find the elemental composition of dust particles. Figure 43 and Table 3 show the elemental analysis of dust particles using EDS detector on JEOL JSM-6460LV SEM. These data show that the majority of dust particles have elemental composition of Calcium, Silicon and Oxygen. This means the majority mineral component of the dust samples was Carbonate ( $\text{CaO}_3^{2-}$ ) and Silica ( $\text{SiO}_2$ ) minerals. There is also Sulfide element which can be from sulfate ( $\text{SO}_4^{2-}$ ) or sulfate mixture with silica. Whereas Magnesium element can be come from dolomite minerals ( $\text{CaMg}(\text{CO}_3)_2$ ).

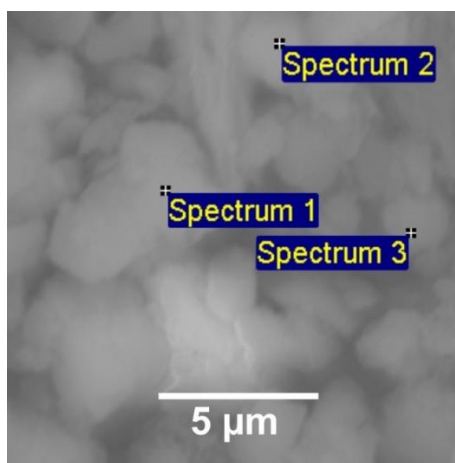


**Figure 43** SEM micrograph of EDS measurement of dust particle

**Table 3 EDS quantitative analysis of dust particle**

Element	Spectrum 1	Spectrum 2	Spectrum 3
O	61.32	57.93	65.94
Mg	2.52	1.79	2.62
Al	2.76	2.48	2.86
Si	7.29	5.79	7.98
S		12.92	
K		0.43	0.52
Ca	24.22	17.63	18.65
Fe	1.89	1.02	1.42
TOTAL	100	100	100

#### **1.14 Oil Impregnated Silica Nanoparticle**

Oil impregnated silica nanoparticle surface coating is one of the approaches studied in this work that is believed that it will minimize the adhesion force between the surface and dust. Moreover, the oil impregnation is also able to create self-cleaning effect to keep the surface clean by help of water droplet rolling on the surface. Table 4 shows samples list which has been done to study this approach. The Corning glass slide was used for this coating as based substrate with 23 x 23 mm<sup>2</sup> size. This coating was done in 3 steps, where each of the steps has specific objective. The first layer is made from silica nanoparticle coating to form hierarchical structure, which aimed at increasing the self-cleaning effect by increasing the hydrophobicity of the surface. The second layer is made by the application of anti-adhesive self-assembly monolayer (SAM), which uses two different silane solution: 5% TMCS and 2% PFOTS in hexane solution. This silanization process was done to increase the hydrophobicity and to bond the third layer which is fluorinated oil.

**Table 4 Oil impregnated silica nanoparticle's samples**

<b>Samples</b>	<b>Number of Samples</b>	<b>First layer</b>	<b>Second layer</b>	<b>Third layer</b>
<b>0</b>	3	Mixed silica	-	-
<b>P</b>	2	5%TMCS-Hexane for 2 h	-	-
<b>Q</b>	2	2%PFOTS-Hexane for 2 h	-	-
<b>A1</b>	3	Mixed silica	5%TMCS-Hexane for 2 h	-
<b>A2</b>	2	Mixed silica	5%TMCS-Hexane for 2 h	Oil
<b>B1</b>	3	Mixed silica	2%PFOTS-Hexane for 2 h	-
<b>B2</b>	2	Mixed silica	2%PFOTS-Hexane for 2 h	Oil

One of the important parameter to study self-cleaning effect is water contact angle that was measured by Kyowa DropMaster DM-501. The most common self-cleaning surface is the hydrophobic surface which has static water contact angle (WCA) more than 90° [49]. The performance of self-cleaning would improve if the WCA is more than 150° which is called superhydrophobic [14]. Figure 44 shows the result of water contact angle measurements

which provides static WCA. The static WCA shows that the surface is already hydrophobic even at first layer which is made only from silica mixed-size nanoparticles. However, the sliding angle of first layer is too high, which makes the water droplet was very difficult to roll unless the surface is tilted to  $30^\circ$ . The layer of 5% TMCS does not change much the sliding angle but the second layer of 2% PFOTS made the sliding angle to worsen leading to it to completely stick. However, it does not matter if static and sliding angle of the second layer is high since the objective of this layer to bond with lubricant in the third layer. In the third layer which is impregnated lubricant, the surface becomes better in cleaning the dust particle since sliding angle was decreased drastically to less than  $5^\circ$  and the static WCA shows the surface still in hydrophobic range with decrease to  $107.3^\circ$  and  $109.7^\circ$  for TMCS and PFOTS coating respectively. The lubricant also adheres on the surface for several days even when the surface is tilted to  $180^\circ$  and water droplet slides on the surface several times. The surface impregnated by PFTOS shows a smaller decrease on static WCA by  $2.4^\circ$  and a higher on sliding angle to  $1^\circ$  due to the effect of the second layer of PFOTS functional groups, which has less hydrophobicity than TMCS on silica particle.

The transmittivity of the samples were measured to investigate the effect of the coating due to its promising application on solar power plant. Table 5 shows the average transmittivity from 400-750 nm which is visible light range. Figure 45 shows the full transmittivity curve from 300 – 900 nm wavelength. From those results, after first layer coating the transmittivity was decreased around 10%. This was caused by silica nanoparticles deposition, which is non-transparent materials, reduces the amount of light transmitted through the surface by absorbing the light or internal scattering effect. Another reason of transmittivity loss is due to surface scattering and reflectance effect of the surface which is



formed by silica nanoparticle deposition. Higher roughness of the surface gives higher transmittivity loss by scattering and reflecting the light.

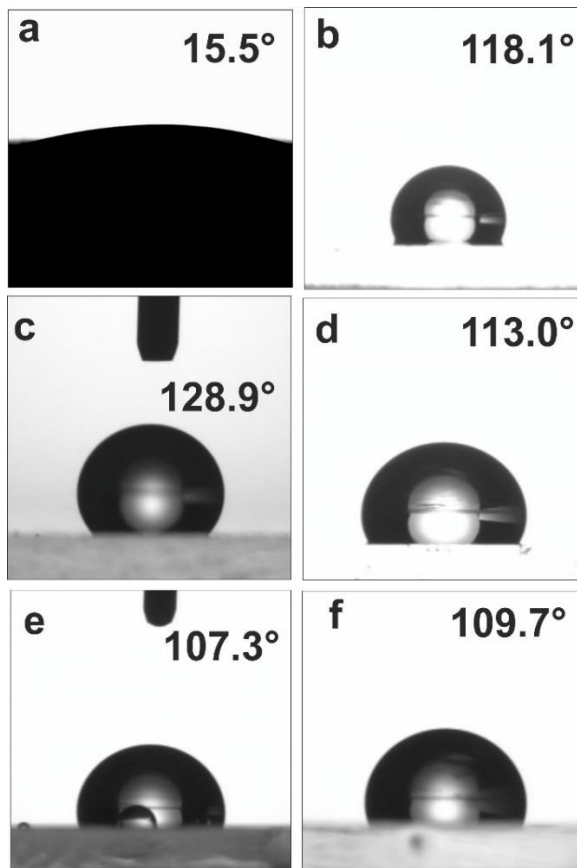


**Figure 44** Static water contact angle of (a) glass substrate, (b) mixed-size silica nanoparticle, (c) sample A11, (d) sample A12, (e) sample B11 and (f) sample B12

The silating agent of TMCS decreased more the transmittivity but PFOTS shows the contrast result which is increasing the transparency. The reason why PFOTS is able to increase the transmittivity is due to it has higher thickness than TMCS. In the SEM characterization, the TMCS coated samples did not show any structure at all, whereas the TMC coated samples still keep the previous morphology structure as shown in Figure 46.

**Table 5** Water contact angle and transmittivity measurement of oil impregnated nanoparticle surface

Samples	WCA (°)	Sliding angle (°)	Transmittivity*(%)
glass	15.5±3.4	Wetting completely	91.8
<b>0</b>	118.1±2.0	30	80.0
<b>P</b>	48.3±2.3	Stick completely	89.8
<b>Q</b>	106.4±1.0	Stick completely	93.6
<b>A11</b>	128.9±0.1	Stick completely	63.9
<b>A12</b>	113.0±3.2	3	83.3
<b>B11</b>	107.3±3.4	Stick completely	89.9
<b>B12</b>	109.7±2.0	4	91.5

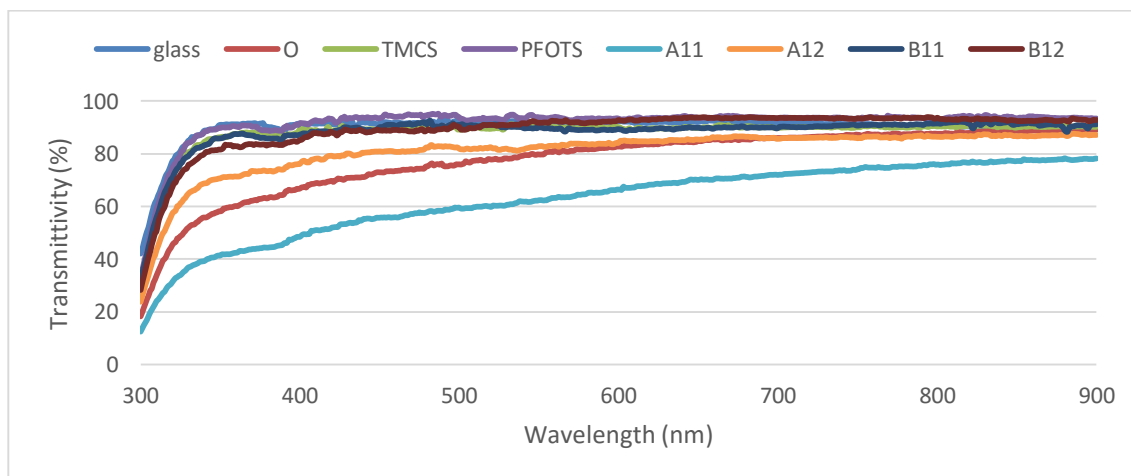


**Figure 45** Transmittivity curve of oil impregnated silica nanoparticle samples from 300 – 900 nm wavelength

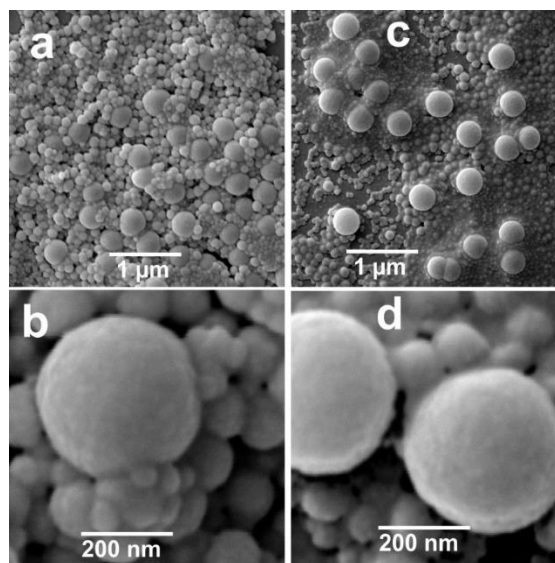


**Figure 46** SEM micrograph of (a & b) sample O: silica mixed size and (c & d) sample A1:  
5% TMCS on silica mixed size

The SEM micrograph shows that the TMCS silating agent is very thin and did not cover completely the structure except some smallest particles (30 nm) was hidden at several spots as shown on Figure 46 c and d. Basically, the silating agent forms this self-assembly monolayer (SAM) on the surface of silica nanoparticle by the reaction of its functional groups, such as Cl- and OH-, with OH- groups on the silica surface. Through the functional groups reaction, silane SAM was formed on the surface as shown on Figure 47.

The AFM also was used to confirm the morphology of the surface further in 3D dimension. The roughness of the surface was calculated from the scanning result data as shown on Figure 48. The roughness of the glass substrate, the mixed-size silica NP and TMCS-modified mixed-silica NP were 1.36, 77.98 and 120.1 nm respectively. It shows that the roughness was increased after silica NP deposition and surface modifying which is the reason why the hydrophobicity or static WCA was increased.

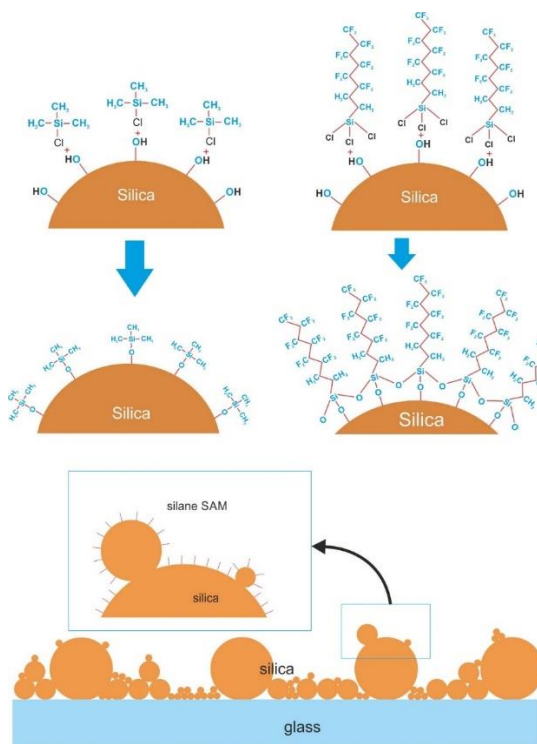


**Figure 47** surface silanization of (left) TMCS and (right) PFOTS

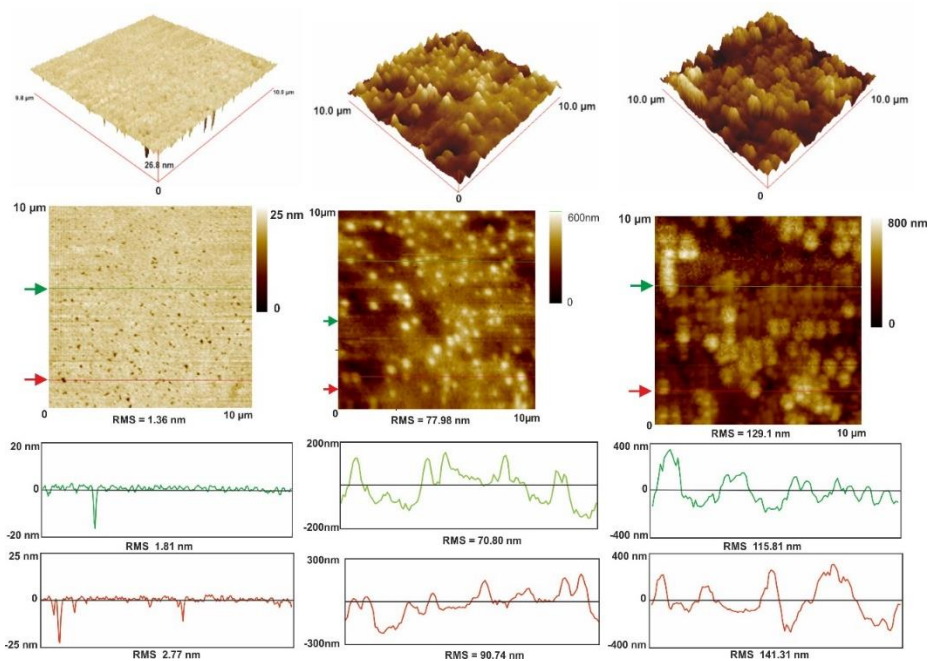


**Figure 48** AFM scanning image of (left) glass substrate, (b) sample O and (c) sample A11

### 1.15 PDMS Double Casting

PDMS, which is transparent silicon based material, was used to cast lotus and rice leaf morphology in order to get transparent hydrophobic surface. Double casting was done to get the positive replica of those leaves morphology. After the first casting the negative replica is produced. Afterward the second casting was done to get the positive replica. However, since negative replica was PDMS and the positive is to be produced using PDMS coating anti adhesive layer must be applied in between these two steps. According to literature [65], anti-adhesive layer should be applied on negative replica to minimize the stickiness between those similar materials. One materials to use as an anti-adhesive is TMCS. After applying TMCS on negative replica, the second replica was relatively easy to be peeled off.

The materials to be copied are rice and lotus leaves since these are superhydrophobic natural leaves with self-cleaning effect and these are very abundant in a country like Indonesia. The problem with these materials, especially lotus leaf, is that these are easily degradable. Lotus leaf rotted just in few days and rice leaf rotted in one to two weeks. The negative casting process should be done immediately before the leaves get spoiled. All of the samples are listed on Table 6.

Figure 49 shows physical appearance of all the samples and their perceived transmittance. It can be concluded that the replicated texture of lotus and rice leaf had lower transmittivity of the PDMS significantly. The transmittivity loss was even more after TMCS coating. However, the oil impregnation recovered back the transparency. Figure 50 and Figure 51 shows the exact transmittivity value of each samples which were characterized by UV-Vis light spectrophotometer.

**Table 6** PDMS lotus leaf double casting's samples

<b>Samples</b>	<b>Number of Samples</b>	<b>First layer</b>	<b>Second layer</b>	<b>Third layer</b>
<b>A1</b>	3	Negative replica	-	-
<b>A2</b>	3	Positive replica	-	-
<b>A3</b>	2	Positive replica	TMCS	
<b>A4</b>	2	Positive replica	TMCS	Oil
<b>B1</b>	3	Negative replica	-	-
<b>B2</b>	3	Positive replica	-	-
<b>B3</b>	2	Positive replica	TMCS	-
<b>B4</b>	2	Positive replica	TMCS	Oil

The transmittivity of lotus leaf replicas shows very bad transparency form all of lotus leaf replica. It was caused by the micro texture of the lotus leaf itself which has many grooves and irregular surface orientation. The orientation of the irregularity of the surface causes more reflection and scattering of light. Another reason is that there are much transfer materials from lotus leaf to negative replica when the first casting was done. Those transfer materials from lotus wax are very opaque. However, the oil impregnation increased the transmittivity very significantly. The cause for this is that he oil fills the grooves on the surface and makes it relatively smooth to minimize reflection and scattering effect of light.



**Figure 49** Optical camera photograph of PDMS double casting samples: (a) - (d) are negative replica, positive replica, TMCS coated positive replica and oil impregnated TMCS coated positive replica of lotus leaf respectively, and (e) - (h) are negative replica, positive replica, TMCS coated positive replica of ice leaf respectively.

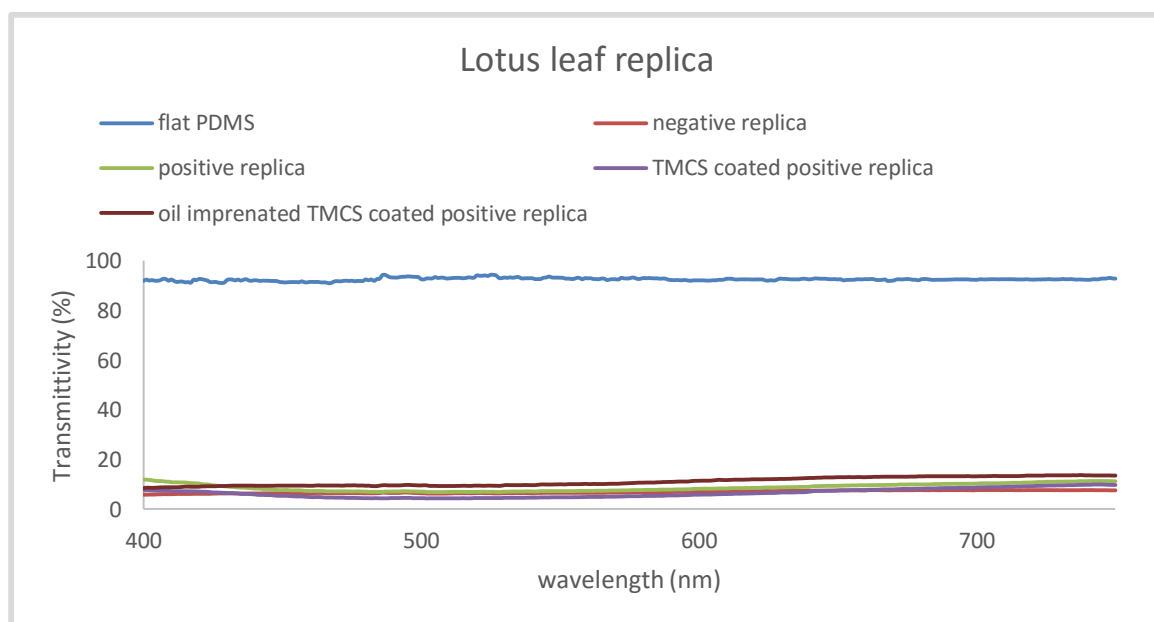


**Figure 50** Transmittivity curve of lotus leaf replica PDMS double casting

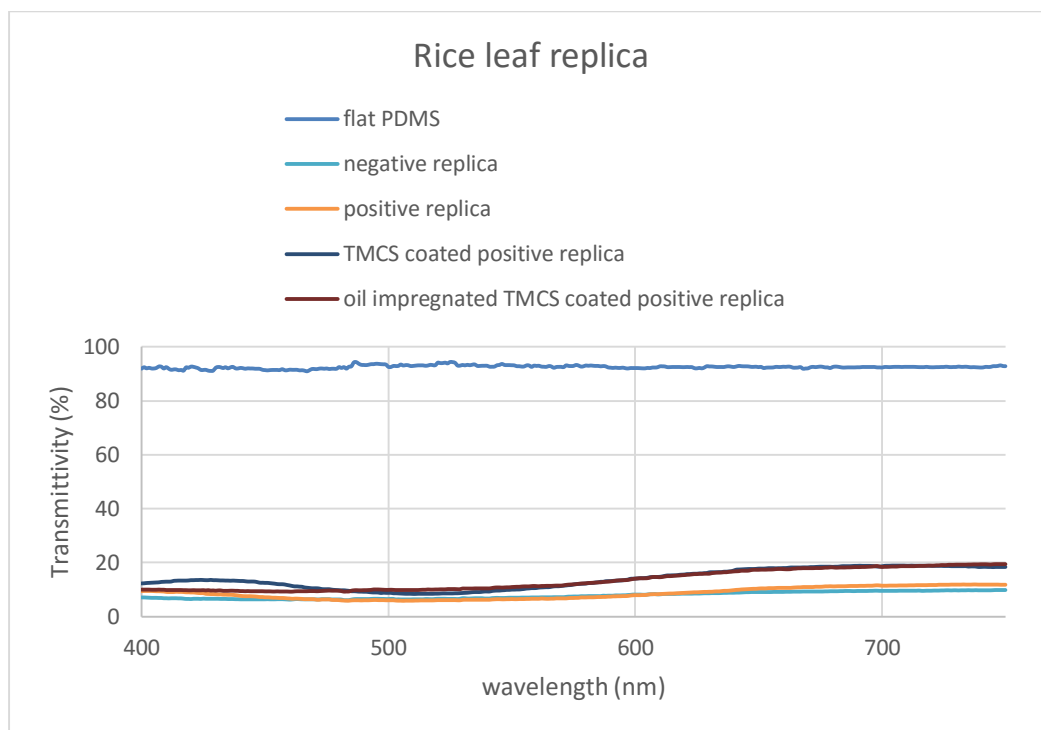


**Figure 51** Transmittivity curve of rice leaf replica PDMS double casting

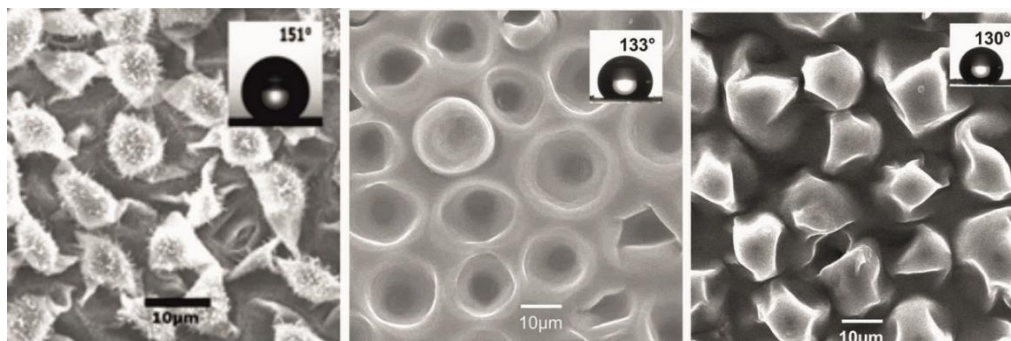


**Figure 52** SEM micrograph of (left to right) lotus leaf, negative replica and positive replica

The SEM micrograph of lotus leaf and its replica shows the micro structure of those surfaces which has many micro spherical-like structure and creases also as shown on Figure 52. Those structure is really decreasing the transmittivity but it give more self-cleaning



effect to the surface. Those structure enhance the roughness of the surface then increase the hydrophobicity which is linier with the self-cleaning effect. However, in lotus leaf structure there are many nano needle-like structure which are not appeared both in negative and positive replica. Those needle-like structures are the main reason lotus leaf has very high water contact angle unlike its replica. Those structure was not replicated most probably because it was damaged in the process of casting since it were very small and soft.

The hydrophobicity of the lotus leaf replicas are shown that these are hydrophobic but it did not achieve superhydrophobic like lotus leaf as shown on Figure 53. The water contact angle of positive replica also has slightly lower than negative replica which most probably caused of holes formed in negative replica acted as air pocket.

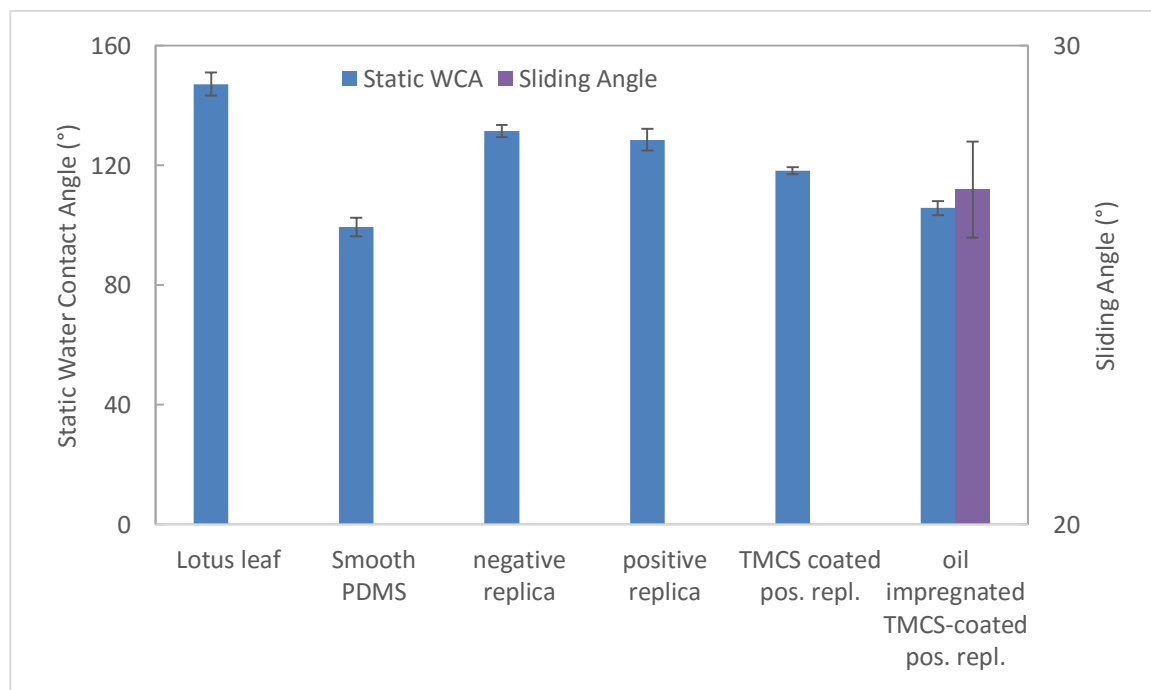


**Figure 53** Water contact angle of lotus leaf replica

On the other hand, rice replicas have better transmittivity which are shown on Figure 51. The reason rice leaf replicas were better due to stability of rice leaf surface materials which is not transferring materials to negative replica. Another reason is due to its structure where there is no creases on rice leaf surface and the structure is relatively more regular than lotus leaf. Those structures can be seen on Figure 54 which indicate also the nano needle-like structures were not replicated as similar as lotus replica. The reason seems similar which is due to damage from casting process even though the rice leaf was felt stronger but the needle-like part is too brittle.

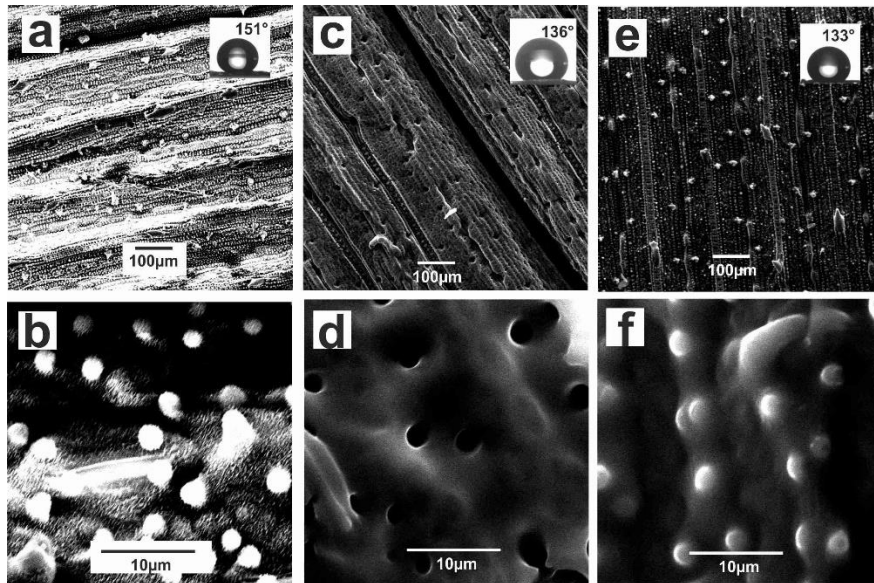


**Figure 54** SEM micrograph of lotus leaf (a & b), negative replica (c & d) and positive replica (e & f)

The water contact angle of rice leaf shows higher than lotus leaf also as shown on Figure 55. Rice leaf has more hierarchical structure as shown in its SEM micrograph. It has straight line and spherical-like structure in micron size and needle-like structure in nano size. It might be the reason rice leaf and its replicas have higher water contact angle.

However, even rice leaf has higher transmittivity and water contact angle but it has disadvantage in term of practical casting process. Rice leaf has size limitation to cast into large area

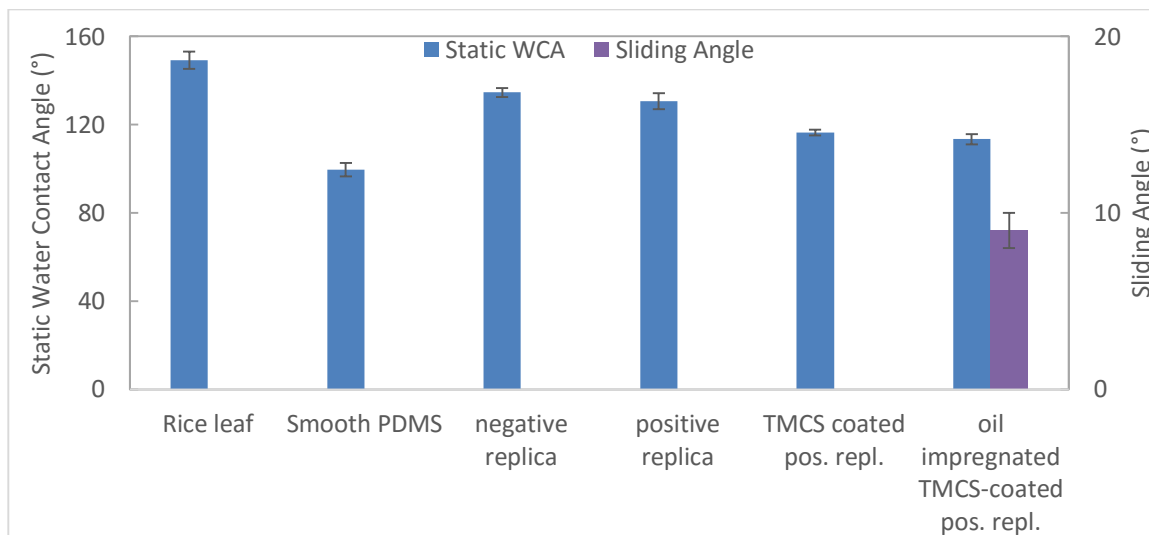


**Figure 55** Water contact angle of rice leaf replicas

### 1.16 Silica Aerogel Nanoparticle Deposition by Sol-gel Dip-coating

Silica aerogel nanoparticle samples were made by sol-gel dip-coating method. The volume ratio of colloidal silica was varied as shown on Table 7. The hydrophobicity of the samples were good especially sample 2 as shown on Figure 56. The static contact angle of sample 1, 2 and 3 are  $137.8 \pm 5.1^\circ$ ,  $143.5 \pm 1.0^\circ$  and  $109.8 \pm 7.5^\circ$  respectively. All of the measurements are done with 15  $\mu\text{L}$  DI water droplet. Whereas, the sliding angle was just obtained on oil impregnated sample 2 which is  $4^\circ$ . Sample 1 to 3 which are not oil-impregnated did not show any sliding angle. Figure 57 shows the surface free energy calculation by goniometer using three different solution (water, formamide and 1-bromonaphthalene). It shows that sample 2 has the lowest surface free energy which is the reason to be chosen as the best sample for oil impregnation step. The silica aerogel was derived from MTMS which have

methyl functional groups. This functional group is the main reason why it has very good hydrophobicity even up to superhydrophobic level.

**Table 7** The samples list of silica aerogel nanoparticle deposition

Sample	Number of Samples	volume (ml)				
		MTMS	MEOH	water	col silica	NH <sub>4</sub> OH
1	2	3	8	2	0	3
3	2	3	8	2	0.5	3
2	2	3	8	2	0.25	3



**Figure 56** Water contact angle of the samples (sample 4 is oil impregnated of sample 2)

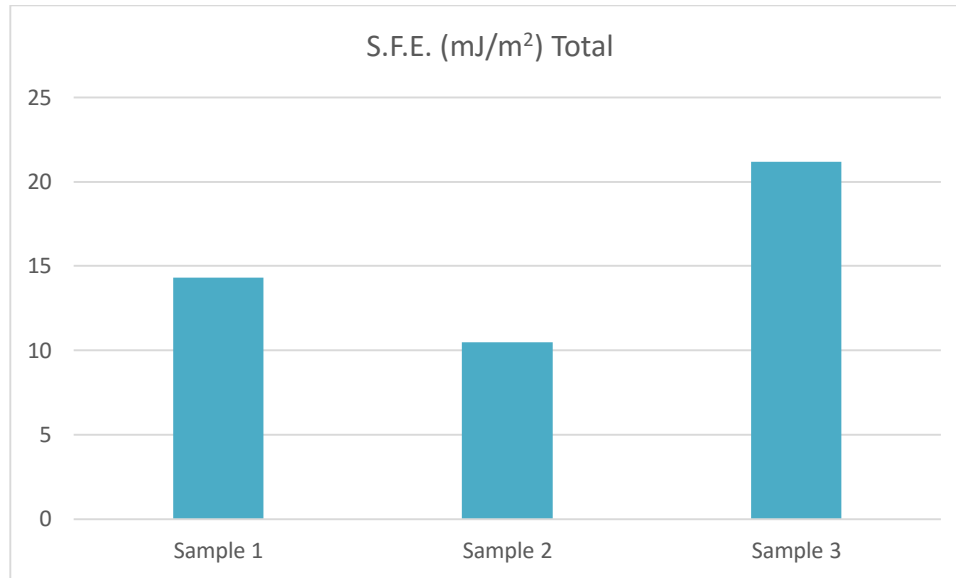


**Figure 57** Surface free energy of the samples

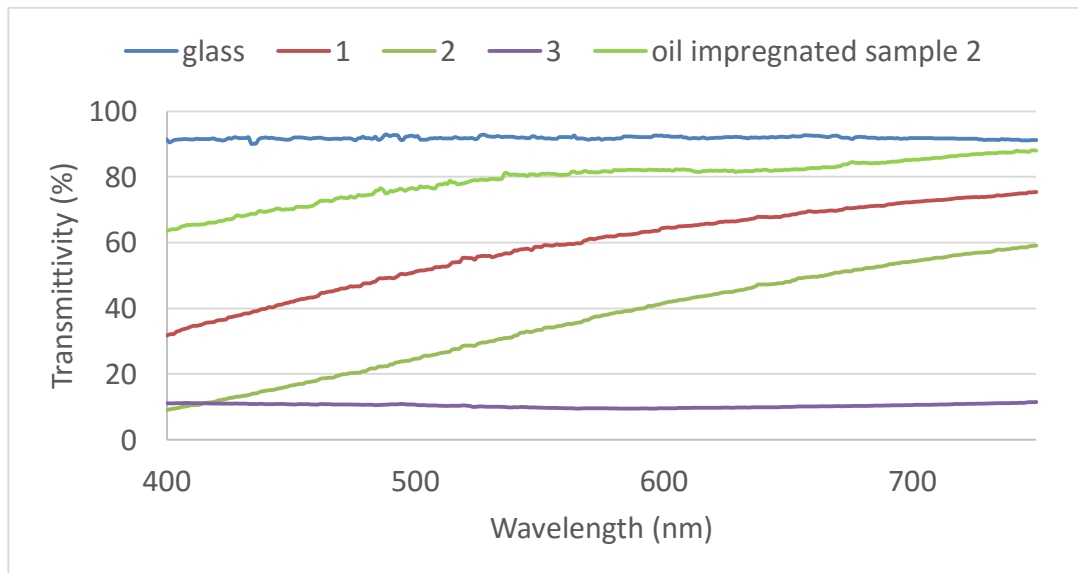


**Figure 58** The transmittivity of the samples

However, the transmittivity of this surface texturing method did not give decent result in term of transmittivity since these samples just have around 59%, 36% and 11% average transmittivity as shown on Figure 58. However, the oil impregnated sample 2 shows promising result which has 79% average transmittivity. The reason of this low

transmittivity is due to high roughness resulted from the combination of silica aerogel and silica NP which are quite opaque materials. The reduction of colloidal silica concentration shows significant improvement of transmittivity which is shown by sample 1 and 2. Oil impregnation increased drastically the transmittivity since it hid all of the grooves by filling with oil. The surface then became very smooth and the oil itself has very good transmittivity.

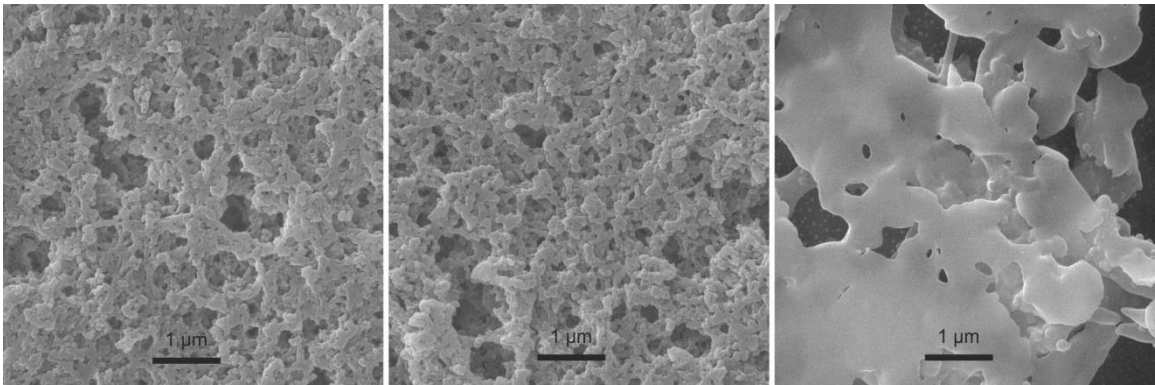


**Figure 59** SEM micrograph of sample 1, 2 and 3 respectively from left to right

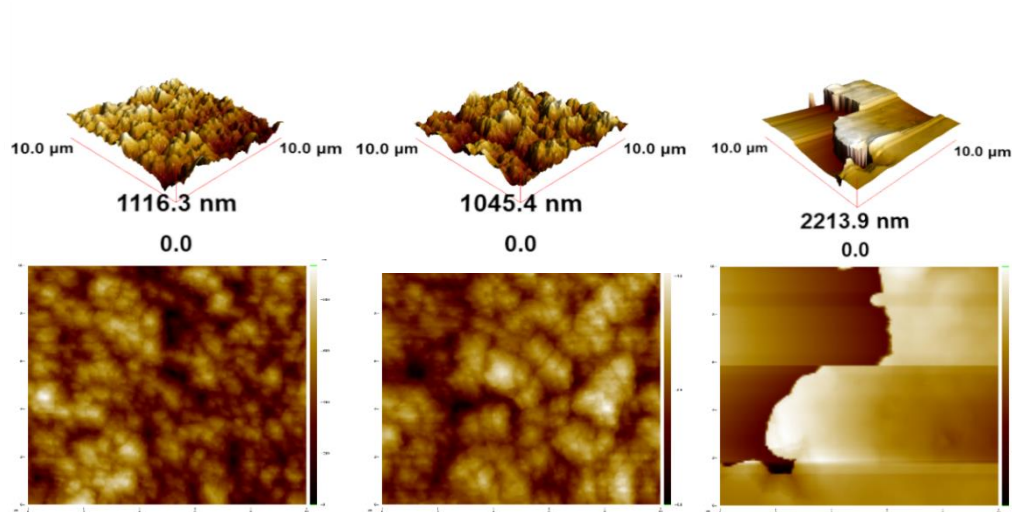


**Figure 60** AFM image of sample 1, 2 and 3 respectively from left to right

The SEM shows randomly porous structure of sample 1 and 2 as shown on Figure 59. This porous structure enhance the roughness and create many air pocket to create hydrophobic surface. The huge number of pores enhance oil stability on the surface. However, sample 3 did not show any porous structure which make it very low hydrophobicity if compare to other samples. The AFM images which is shown by Figure 60 confirms the morphology of each samples from 3D perspective.

### 1.17 Dynamic Dust Cleaning

The forces related to the dust particles located on the rotating disk are predicted from the sets equations (in chapter 1) and the experiments are carried out to identify the amount of dust particles removed from the polycarbonate disk surface after completing the rotation of the disk at various rotational speeds. The force simulations are carried out in line with the experimental conditions incorporating the dust particle size, density, and dust locations on the disk surface. It should be noted that the dust density is measured and the averaged dust particle density is in the order of  $2600 \text{ kg/m}^3$ .

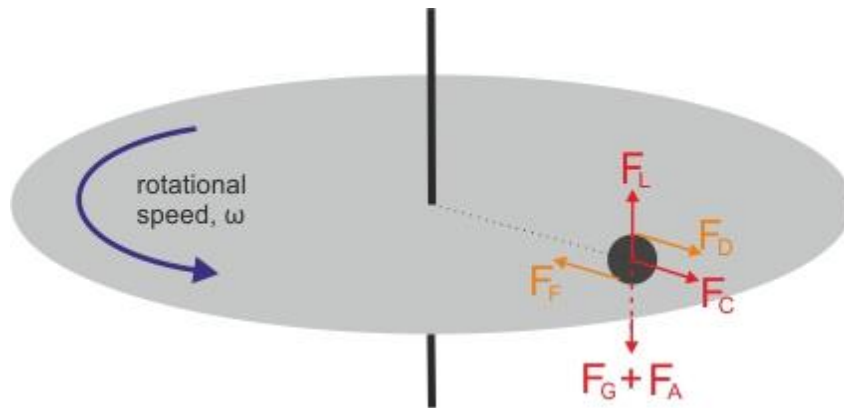


**Figure 61** A schematic view of forces acting on the dust particles during spinning

The forces acting on the dust particles include van der Waals, electrostatic, capillary, lift, drag, and gravitational forces. However, the adhesion force is modified by using Rump-

Rabinovich model, which incorporates the van der Waals force and the roughness of the surface [29]. The lift force acts on z-direction, which is opposite to the Rump-Rabinovich and the gravitational forces (Figure 61). The drag and centrifugal forces act on the lateral direction towards the edge of the disk. The friction force acts opposite to the particle motion and it is related to the gravitational force. In the analysis, three mechanisms are considered for the removal of the dust particles from disk surface during the rotation. The first mechanism is associated with lifting; in which case, if the lift force is larger than the combination of the Rump-Rabinovich and the gravitational forces, the particle can be lifted from the surface. The second one is the sliding, which takes place for the case when the centrifugal force is larger than the frictional force. The third mechanism is related to the rolling, which occurs when the centrifugal force is small, but the drag force is higher than the frictional force.

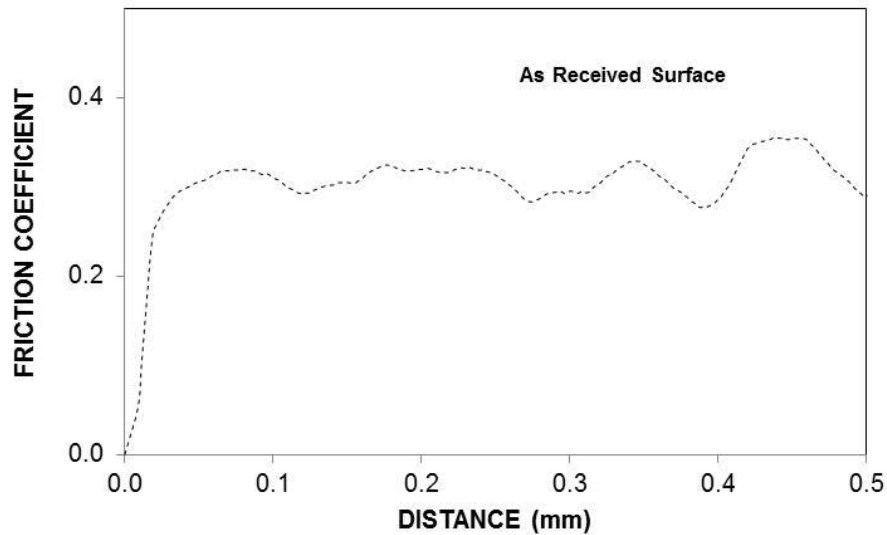


**Figure 62** Friction coefficient for polycarbonate plane sheet without dust on the surface.

In the simulations, the rotational speed of the disk is varied from 0 to 100 rad/s and the dust position is altered from the rotational center towards the disk edge within the range of 0 to



10 cm in line with the experimental conditions for three minutes. Here, 0 represents the rotational center and 10 cm corresponds to the disk edge. In the simulations, the dust particle size is considered as 10  $\mu\text{m}$ , which is averaged size of the dust particles in terms of the volume distribution of the dust particles. The tribology tests are carried out to measure the friction coefficient of the polycarbonate surface. Figure 62 shows the friction coefficient variation along the scan length on the polycarbonate surface. The average friction coefficient is found to be 0.23, which is set in the simulations.

Figure 63 and Figure 64 show the counter plots of ratio of the centrifugal, frictional, drag, lift, and gravitational forces over the adhesion force. Since the adhesion force ( $F_a$ ) is critical for the removal of dust particle from the disk surface, the forces generated on the dust particle are normalized with the adhesion force. In general, increasing the distance along the disk radius towards the disk edge enhances the centrifugal, drag and lift forces acting on the dust particle to be increased. However, the adhesion force remains almost constant along the disk radius. In addition, increasing rotational speed of the disk and dust particle size generate similar behavior for the forces. The adhesion force remains higher than the lift, gravitational, drag, and friction forces. At some radial locations on the disk, centrifugal force becomes larger than the adhesion force, provided that this situation depends on the dust particle size. In this case, the adhesion force remains higher than the centrifugal force for the small size particles at locations close to the center of rotation of the disk. Therefore, the dust removal from the surface may be possible for large size dusts ( $\geq 3 \mu\text{m}$ ) located on the disk surface, which is more pronounced for the locations close to the disk edges.

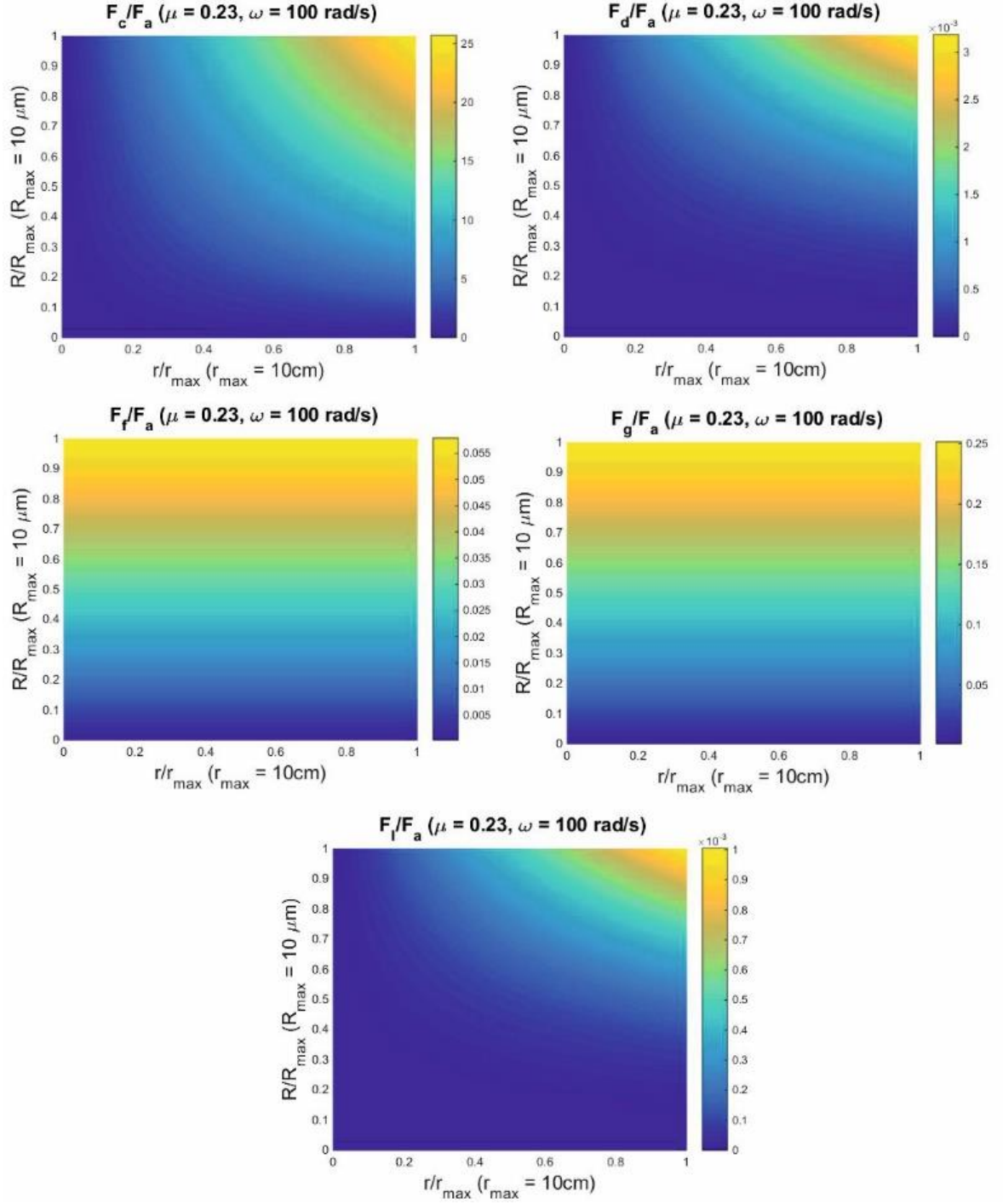


**Figure 63** Contour plots of force ratios along the radial distance ( $r$ ) for different dust particle radius ( $R$ ). The rotational speed is 100 rad/s.

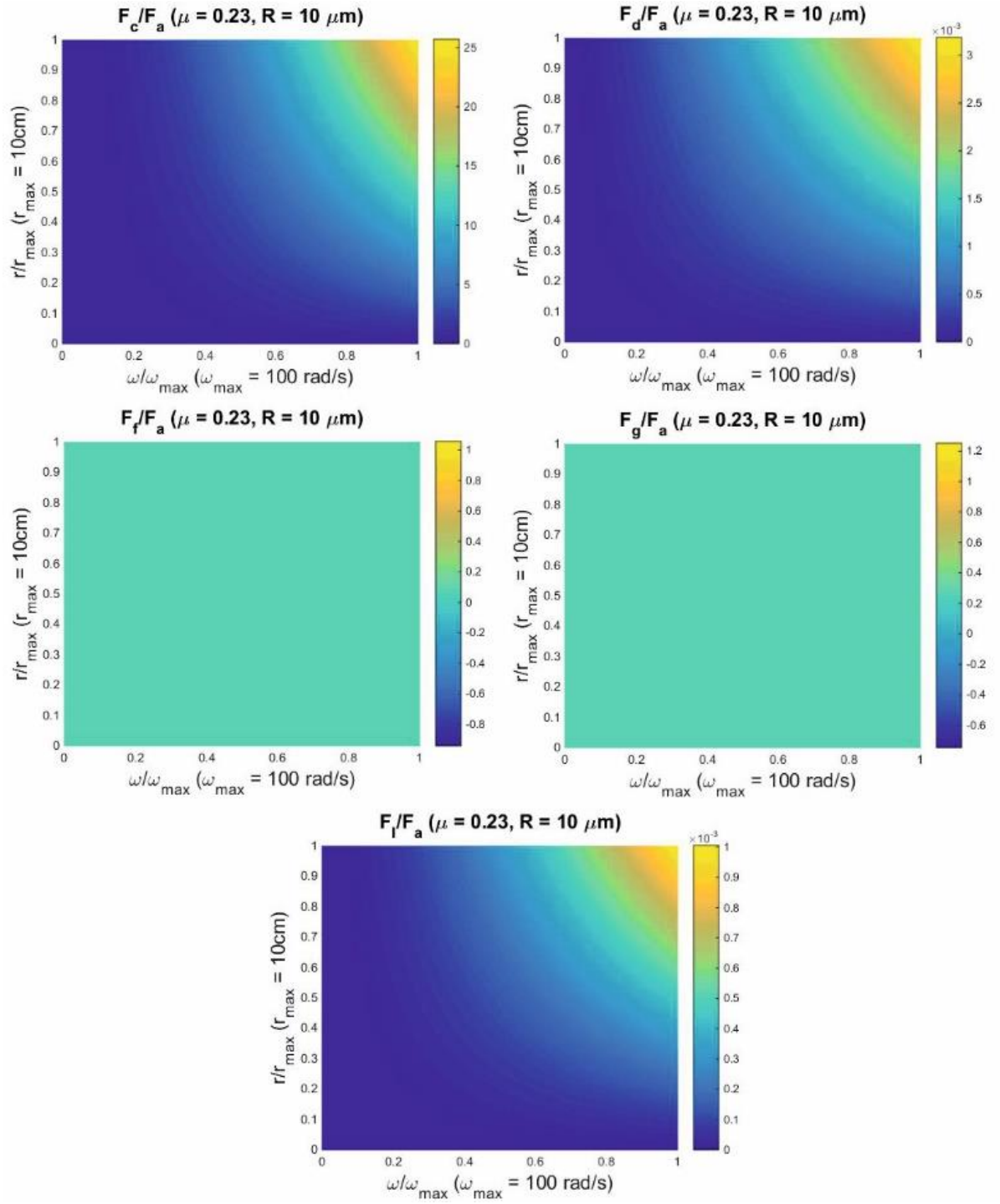


**Figure 64** Contour plots of force ratios along the radial distance ( $r$ ) for different rotational speed ( $\omega$ ). The dust particle radius is  $10 \mu\text{m}$ .

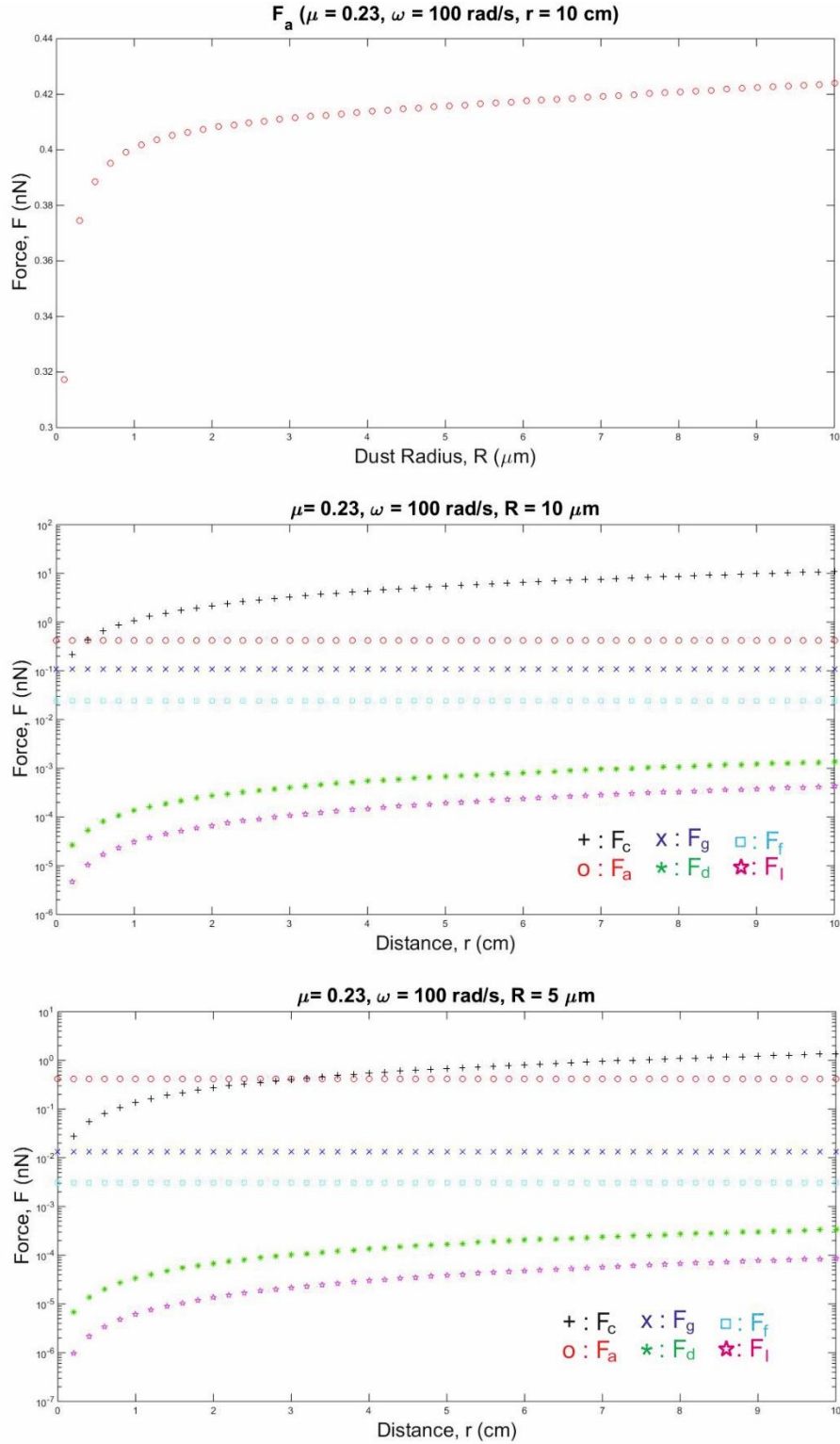


**Figure 65** Semi-log plot of forces along radial distance along disk surface for two dust particle sizes. Adhesion force variation along dust particle radius at disk edge and for  $\omega = 100$  rad/s.

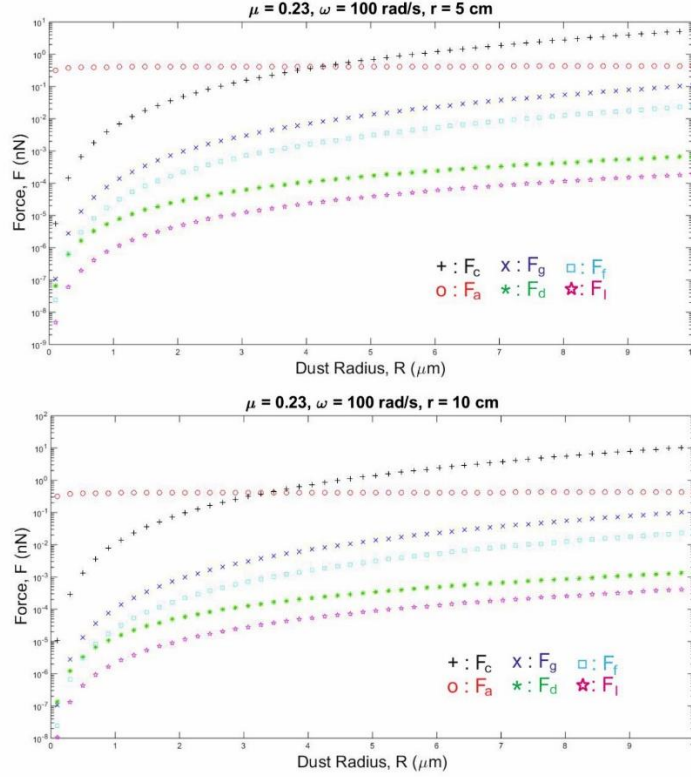


**Figure 66** Semi-log plot of forces with dust particle radius ( $R$ ) for two radial locations on disk.

Figure 65 to Figure 67 show variation of the forces including centrifugal ( $F_c$ ), gravitational ( $F_g$ ), adhesion ( $F_a$ ), Frictional ( $F_f$ ), and drag ( $F_d$ ) forces. The centrifugal, lift, and drag forces increase with distance along the disk radius; however, the other forces remain almost the same. This behavior is associated with the assumption of constant friction coefficient along the disk radius at the surface and constant mass of the dust particle. The adhesion and gravitational forces remain almost constant along the radius at the surface of the disk. The centrifugal force remains high along the radius and it is higher than the other forces. However, the adhesion force becomes higher than the other forces for the particle location close to the rotational center, i.e. 2 cm away from the disk center. Therefore, in the close region of the rotating disk center, the adhesion force is dominant. In addition, the drag and

lift forces become extremely small as compared to that of the gravitational, friction, centrifugal, and adhesion forces. The similar arguments are also true for the small size dust particle (5  $\mu\text{m}$ ), which can be seen in Figure 65. In the case of force variation with the dust particle size (Figure 66), the lift, drag, gravitational, and centrifugal forces increases with increasing dust particle size. However, this increase is sharp for the dust particle sizes  $\leq 3 \mu\text{m}$ . The adhesion force remains higher than all the other forces for these size particles ( $\leq 3 \mu\text{m}$ ). This is true for the dust particle location being at the edge of the disk. As the dust particle location becomes close to the rotational center (5 cm), adhesion force remains higher than the other forces for the dust particles  $\leq 4 \mu\text{m}$ . Consequently, this indicates that the location of the dust particles at the disk surface is very critical to overcome the adhesion force; in which case, the centrifugal force generated becomes larger than the adhesion force while giving rise to removal of the dust particles with sizes  $\geq 3 \mu\text{m}$  from the edge of the disk. It should be noted that the adhesion force varies with the dust particle size. The small plot in Figure 65 shows the adhesion force variation with distance. The effect of rotational speed on the forces generated on the dust particle is shown in Figure 67. The centrifugal force is higher than the adhesion force for the rotational speed in the order of 20 Hz for the case where the dust particle is located at the edge of the disk (10 cm). The rotational speed when the centrifugal force becomes higher than the adhesion force occurs almost at 30 Hz for the dust particle, which is located at mid-distance on the disk surface (5 cm). The rotational speed should be large enough to overcome the adhesion force for the particle removal. The dust particle removal from the disk surface is not possible for the certain range of the rotational speeds. This situation changes with particle location at the surface.

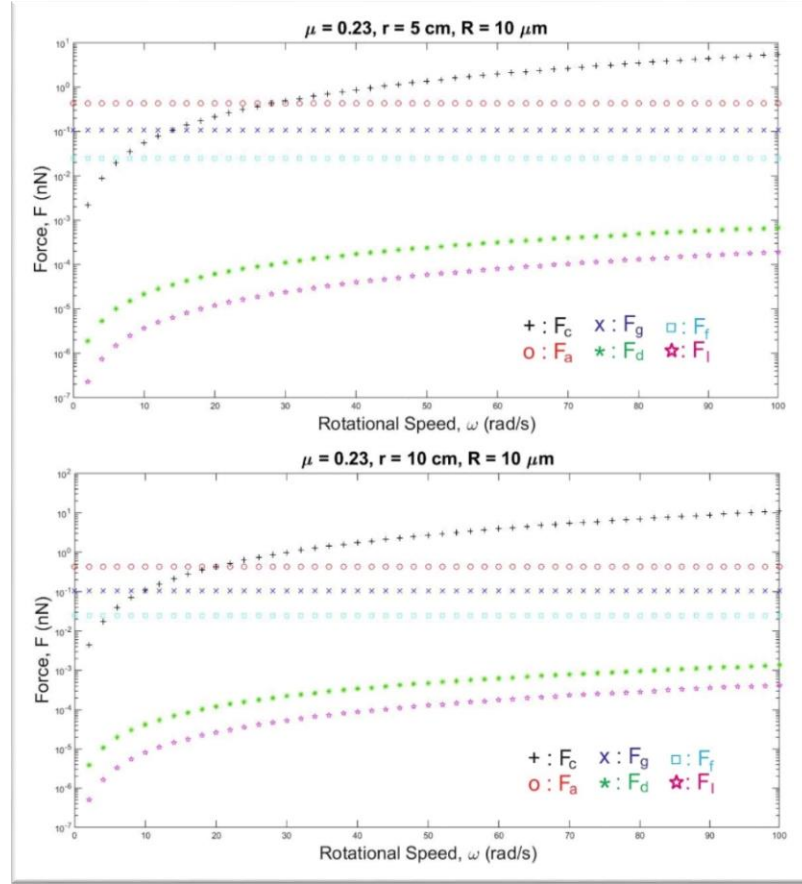


**Figure 67** Semi-log plot of forces with rotational speed ( $\omega$ ) for two radial locations on disk.

**Table 8** Dust removed from polycarbonate disk surface by rotation

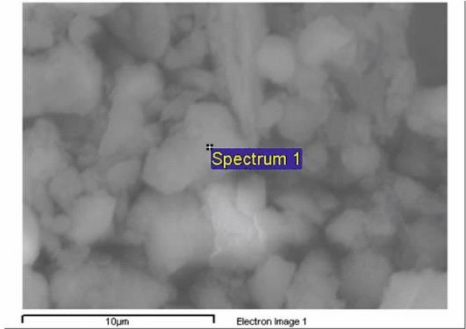
	Speed (rpm)			
	100	175	250	375
disc weight (gr)	21.998	21.998	21.999	22.000
disc/dust weight(gr)	22.065	22.075	22.068	22.071
dust weight (gr)	0.066	0.076	0.069	0.071
disc/dust weight after rotation (gr)	22.063	22.055	22.026	22.016
dust loss (gr)	0.002	0.020	0.043	0.056
Dust loss percentage (%)	3.167	25.916	61.383	78.230

In order to investigate the dust removal from the rotating disk, an experiment is carried out and the weight percentage of the dust particles removed from the disk surface recorded.

Table 8 gives the percentage of dust removed from the surface for various rotational speeds

of the disk. It is evident that, the percentage of the dust particles removed increases significantly with increasing rotational speed. This behavior is mainly attributed to the increase in the centrifugal force at high rotational speeds, which is in agreement with the predictions (Figure 66). To examine the dust residuals on the disk surface after the tests, the geometric features and the elemental composition of the dust residues are analyzed using the electron scanning microscope (SEM) and energy dispersive spectroscopy (EDS). Figure 68 shows SEM micrographs of the dust residues on the disk surface. The dust residues compose of fine size small particles, which attach together at the disk surface. The bright appearance of the dust particles indicates that the electron charge is high at the particle surface. Therefore, the dust residues have charge field, which enhances the adhesion of these particles at the surface.

**Table 9** The elemental analysis of dust residue on the disk surface

Element	Weight %	Atomic %	
O K	57.93	74.43	
Mg K	1.79	1.51	
Al K	2.48	1.89	
Si K	5.79	4.24	
S K	12.92	8.28	
K K	0.43	0.23	
Ca K	17.63	9.04	
Fe K	1.02	0.38	

The elemental analysis (Table 9) reveals that the dust residues contain alkaline (Na, K) and alkaline earth (Ca) metal compounds. These contribute to the ionic bonding at the surface under the influence of humidity [77], which in turn enhances the adhesion between the dust particles and the disk surface. Therefore, the equation used for the adhesion may not be



applicable for this case. This is because of the fact that the formulation of adhesion based on Rump-Rabinovich model relies on the van der Waals forces only and the contribution of the ionic compounds and electrostatic forces to the adhesion force is excluded in the formulation. Consequently, the presence of ionic bonding and electrostatic charge forces in between the dust particles and the disk surface modifies the adhesion force. Nevertheless, the amount of dust residues remain at the surface is small; therefore, rotation of the disk enables to remove the large amount of the dust particles from the disk surface. To assess the adhesion between the dust residuals and the polycarbonate surface, atomic force microscopy force measurement is incorporated. Figure 69a shows atomic force microscope image of the dust residual on the polycarbonate surface while Figure 69b shows the friction image obtained from the atomic force microscope tip. It should be noted that the sensitivity of the atomic force microscope cantilever tip is proportional to the slope of the lateral bending of the tip while the tip is in contact with the surface. From the deflection relation, the adhesion force can be written as:

$$F = k\sigma\Delta V \dots\dots\dots 18$$

where  $k$  is the spring constant of the cantilever tip (N/m)  $\sigma$  is the slope of the displacement over the probe voltage recorded ( $\Delta z/\Delta V$ , m/V), and  $\Delta V$  is the voltage recorded during the surface scanning by the tip in the contact mode. In the measurements, the following data is adopted;  $k = 0.12$  N/m and  $\Delta z/\Delta V = 1.481 \times 10^{-6}$  m/V. The adhesion force obtained from the atomic force microscopy measurement is in the order of 8.6 nN while the calculated adhesion force from the Rump-Rabinovich model is in the order of 0.4 nN (Figure 64) for the same size of the dust size (1.1  $\mu\text{m}$ ) used in the measurements (Figure 68a). This shows

the influence of the ionic compounds and electrostatic forces on the adhesion force between the particles and the disk surface.

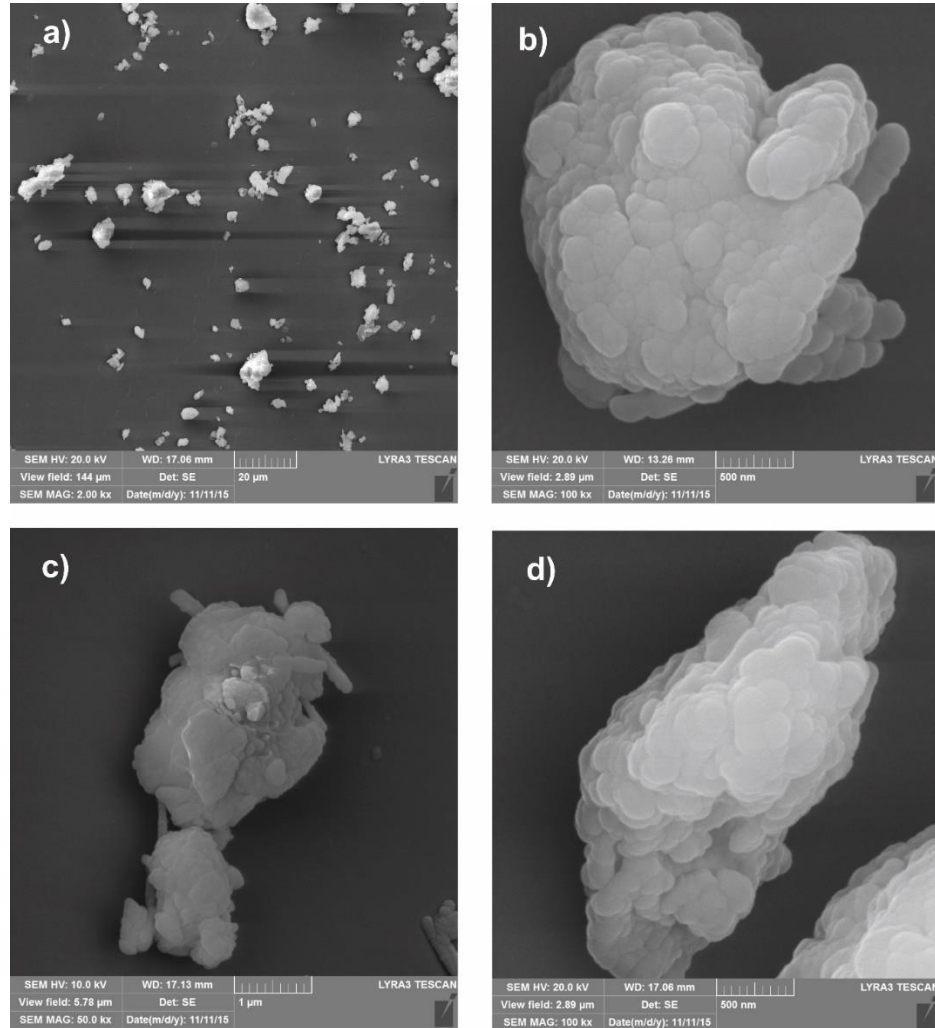


**Figure 68** SEM micrographs of dust residues on polycarbonate disk: a) small and large size dust residues, b) dust residues composed of fine size dust particles, c) combined dust particles, d) elongated dust particles composed of fine size dust particles.

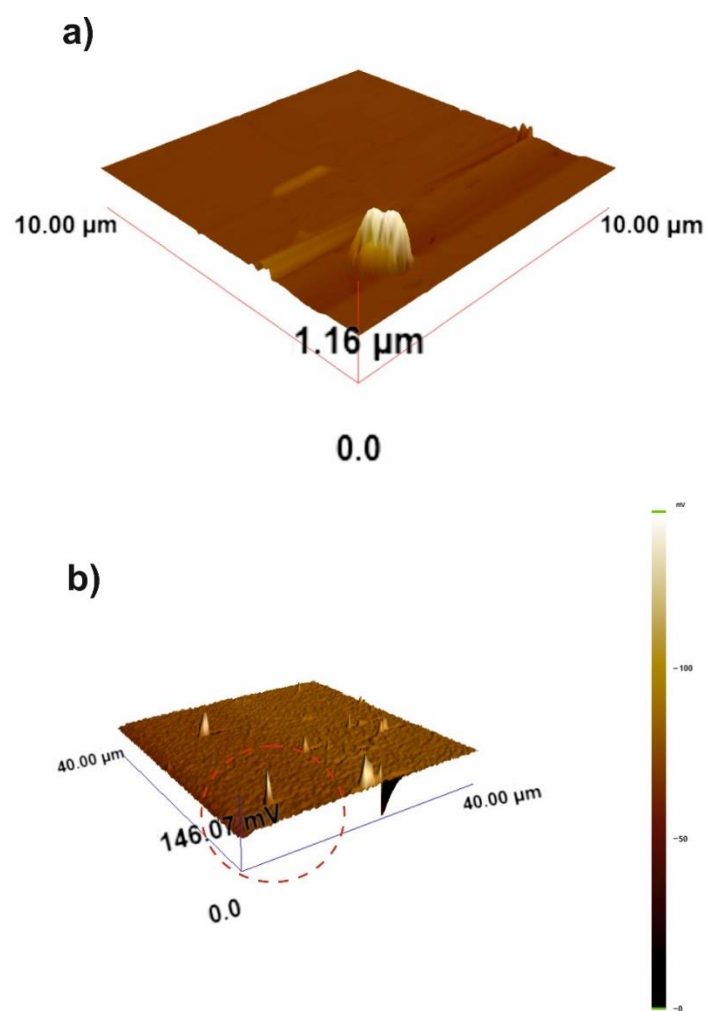


**Figure 69** AFM micro-images of dust particle and the adhesion force: a) dust particle on polycarbonate surface, and b) tangential force map recorded from AFM. The peak in the red circle represents the tangential force for the dust particle shown above.

## **CHAPTER 5**

### **CONCLUSION AND FUTURE WORK**

#### **1.18 Conclusion**

##### **1.18.1 Surface Texturing**

Surface texturing is one of the effective ways to create self-cleaning surface since hydrophobicity is influenced mostly by the structure of the surface. However, not all of the surface texturing gives a good result in term of transparency of the surface. Surface functionalized silica nanoparticle with different size particle is created successfully to create micro-nano hierarchical structure on glass surface. The oil impregnation gives better transparency and sliding angle. To sum up, the oil impregnated modified silica nanoparticle surface is creating self-cleaning surface with  $113^\circ$ ,  $3^\circ$  and 83% of static water contact angle, sliding angle and average transmittivity respectively.

PDMS double casting of lotus and rice leaf does not give good results in term of transparency. Both PDMS replica of lotus and rice leaf have transmittivity less than 20% which is not promising for transparent application such as photovoltaic cover. The static water contact angle was relatively good which, with measurements of  $129^\circ$  and  $131^\circ$  for lotus and rice leaf respectively. The sliding angle of lotus leaf after oil impregnation is  $27^\circ$  which is not efficient for self-cleaning surface but the rice leaf replica has good sliding angle which is  $9^\circ$ .

Silica aerogel nanoparticle deposition by sol-gel dip-coating shows very promising hydrophobicity, which has  $156^\circ$  static WCA and  $7^\circ$  sliding angle. However, that superhydrophobic sample also has low transmittivity measuring around 50%. The decreasing concentration of colloidal silica from 1 to 0.25 compare to ethanol shows improvement of transmittivity from 10% to 50%.

### **1.18.2 Dynamic Dust Cleaning**

Centrifugal force is the only force that is effective in removing dust from the surface by the sliding mechanism since it is higher than frictional force. At 100 rad/s and 6 cm dust position from the center of rotation, the centrifugal force is 60, 15, and 120 times higher than gravitational, adhesion and frictional forces respectively. The lift and drag forces, which can lift and roll the dust are 100-1000 times less than adhesion and frictional force. In the experimental study, the dust is effectively removed from polycarbonate surface even at relatively high angular speed. Many factors increased the adhesion force, among them are dust agglomeration and dust wide size-distribution. The experimental work shows that the accumulated dust can be cleaned by 3.2, 25.9, 61.4 and 78.2 percent at 100, 175, 250 and 375 rpm respectively.

## **1.19 Future Work**

### **1.19.1 Surface Texturing**

According to the result of this study, PFOTS coating is not a good candidate to be applied on a surface while in liquid phase deposition. In the future work, PFOTS vapor deposition might give better results using Chemical Vapor Deposition (CVD) or Plasma Enhanced Chemical Vapor Deposition (PECVD).

Lotus and rice leaves replicas also did not give good results in term of transmittivity, thus another replica such as silicon micro-pillar template might be a good candidate to improve the transparency. However, according to my experience the silicon micro-pillar might give lower static WCA due to the lack of the necessary hierarchical structure. The pillar spacing can be varied to study its effect on WCA and transmittivity.

### **1.19.2 Dynamic Dust Cleaning**

The experimental work on other parameters such as dust radius (R) and particle distance (r) should be performed to validation data on forces calculations. Characterization using XRD is also important since it will give provide additional data on the composition in term of compounds and minerals of the dust samples. The dust removal amount measurement on coated samples also should be calculated to compare between bare glass and PC to coated glass and coated PC.

## References

- [1] W. Mahdi, M. Roca, Saudi Arabia Plans \$109 Billion Boost for Solar Power, Bloomberg.com. (2012). Saudi Arabia Plans \$109 Billion Boost for Solar Power (accessed September 12, 2015).
- [2] M. Mani, R. Pillai, Impact of dust on solar photovoltaic (PV) performance: Research status, challenges and recommendations, *Renew. Sustain. Energy Rev.* 14 (2010) 3124–3131. doi:10.1016/j.rser.2010.07.065.
- [3] A.A. Hegazy, Effect of dust accumulation on solar transmittance through glass covers of plate-type collectors, *Renew. Energy.* 22 (2001) 525–540.
- [4] J.K. Kaldellis, a. Kokala, Quantifying the decrease of the photovoltaic panels' energy yield due to phenomena of natural air pollution disposal, *Energy.* 35 (2010) 4862–4869. doi:10.1016/j.energy.2010.09.002.
- [5] F. Zhang, A. a. Busnaina, M. a. Fury, S.-Q. Wang, The removal of deformed submicron particles from silicon wafers by spin rinse and megasonics, *J. Electron. Mater.* 29 (2000) 199–204. doi:10.1007/s11664-000-0142-0.
- [6] P.G. Saffman, The lift on a small sphere in a slow shear flow, *J. Fluid Mech.* 22 (1965) 385.
- [7] M.A. Hubbe, Detachment of Colloidal Hyrous Oxide Spheres from Flat Solids Exposed to Flow, *Colloids and Surfaces.* 16 (1986) 227–248.
- [8] C.I. Calle, C.R. Buhler, J.L. McFall, S.J. Snyder, Particle removal by electrostatic and dielectrophoretic forces for dust control during lunar exploration missions, *J. Electrostat.* 67 (2009) 89–92. doi:10.1016/j.elstat.2009.02.012.
- [9] P. Atten, H.L.P.H.L. Pang, J.L. Reboud, Study of Dust Removal by Standing-Wave Electric Curtain for Application to Solar Cells on Mars, *IEEE Trans. Ind. Appl.* 45 (2009) 75–86. doi:10.1109/TIA.2008.2009723.
- [10] M. Ma, R.M. Hill, Superhydrophobic surfaces, *Curr. Opin. Colloid Interface Sci.* 11 (2006) 193–202. doi:10.1016/j.cocis.2006.06.002.
- [11] I.P. Parkin, R.G. Palgrave, Self-cleaning coatings, (2005) 1689–1695. doi:10.1039/b412803f.
- [12] V.A. Ganesh, H.K. Raut, a. S. Nair, S. Ramakrishna, A review on self-cleaning coatings, *J. Mater. Chem.* 21 (2011) 16304. doi:10.1039/c1jm12523k.
- [13] X. Yang, L. Zhu, Y. Chen, B. Bao, J. Xu, W. Zhou, Preparation and characterization of hydrophilic silicon dioxide film on acrylate polyurethane coatings with self-cleaning ability, *Appl. Surf. Sci.* 349 (2015) 916–923. doi:10.1016/j.apsusc.2015.05.007.
- [14] E. Ueda, P. a. Levkin, Emerging Applications of Superhydrophilic-Superhydrophobic Micropatterns, *Adv. Mater.* 25 (2013) 1234–1247.

doi:10.1002/adma.201204120.

- [15] J. Drelich, E. Chibowski, Superhydrophilic and superwetting surfaces: Definition and mechanisms of control, *Langmuir*. 26 (2010) 18621–18623. doi:10.1021/la1039893.
- [16] E. Pierce, F.J. Carmona, A. Amirfazli, Understanding of sliding and contact angle results in tilted plate experiments, *Colloids Surfaces A Physicochem. Eng. Asp.* 323 (2008) 73–82. doi:10.1016/j.colsurfa.2007.09.032.
- [17] A.K. Mondal, K. Bansal, A brief history and future aspects in automatic cleaning systems for solar photovoltaic panels, *Adv. Robot.* 29 (2015) 515–524. doi:10.1080/01691864.2014.996602.
- [18] C.I. Calle, J.L. Mcfall, C.R. Buhler, S.J. Snyder, E.E. Arens, Dust Particle Removal by Electrostatic and Dielectrophoretic Forces with Applications to NASA Exploration Missions, *ESA Annu. Meet. Electrostat.* (2008) 1.
- [19] R.B. Williams, R. Tanimoto, A. Simonyan, S. Fuerstenau, Vibration characterization of self-cleaning solar panels with piezoceramic actuation, *Collect. Tech. Pap. - AIAA/ASME/ASCE/AHS/ASC Struct. Struct. Dyn. Mater. Conf.* 1 (2007) 512–520.
- [20] M. Almazroui, Calibration of TRMM rainfall climatology over Saudi Arabia during 1998-2009, *Atmos. Res.* 99 (2011) 400–414. doi:10.1016/j.atmosres.2010.11.006.
- [21] G.J. Huffman, R.F. Adler, P. Arkin, A. Chang, R. Ferraro, A. Gruber, et al., The Global Precipitation Climatology Project (GPCP) Combined Precipitation Dataset, *Bull. Am. Meteorol. Soc.* 78 (1997) 5–20. doi:10.1175/1520-0477(1997)078<0005:TGPCPG>2.0.CO;2.
- [22] A.H. Al Shehri, Dust Mitigation in the Desert : Cleaning Mechanisms for Solar Panels in Arid Regions, in: *Saudi Arabia Smart Grid Conference on Smart Grids and Green Energy* (Ed.), Saudi Arabia Smart Grid Conference on Smart Grids and Green Energy, Jeddah, 2014: pp. 1–18. <http://saudi-sg.com/2014/files/session/B-63.pdf>.
- [23] M. Corn, The Adhesion of Solid Particles to Solid Surfaces, I. a Review, *J. Air Pollut. Control Assoc.* 11 (1961) 523–528. doi:10.1080/00022470.1961.10468032.
- [24] Q. Li, V. Rudolph, W. Peukert, London-van der Waals adhesiveness of rough particles, *Powder Technol.* 161 (2006) 248–255. doi:10.1016/j.powtec.2005.10.012.
- [25] R. Bowling, A theoretical review of particle adhesion, *Part. Surfaces* 1. (1988) 129–142. [http://link.springer.com/chapter/10.1007/978-1-4615-9531-1\\_10](http://link.springer.com/chapter/10.1007/978-1-4615-9531-1_10).
- [26] S.D. Johnson, K. L.; Kendal, K.; Roberts, Surface energy and the contact of elastic solids, 324 (2012) 301–313.
- [27] B.V. Derjaguin, V.M. Muller, Y.P. Toporov, Effect of contact deformations on the adhesion of particles, *Prog. Surf. Sci.* 45 (1994) 131–143.
- [28] H.C. Hamaker, The London—van der Waals attraction between spherical particles,



Physica. 4 (1937) 1058–1072.

- [29] Y. Rabinovich, J. Adler, A. Ata, R. Singh, B. Moudgil, Adhesion between Nanoscale Rough Surfaces: I. Role of Asperity Geometry, *J. Colloid Interface Sci.* 232 (2000) 10–16. doi:10.1006/jcis.2000.7167.
- [30] N. Gao, Y. Yan, Modeling Superhydrophobic Contact Angles and Wetting Transition, *J. Bionic Eng.* 6 (2009) 335–340. doi:10.1016/S1672-6529(08)60135-3.
- [31] M. Nosonovsky, B. Bhushan, Superhydrophobic surfaces and emerging applications: Non-adhesion, energy, green engineering, *Curr. Opin. Colloid Interface Sci.* 14 (2009) 270–280. doi:10.1016/j.cocis.2009.05.004.
- [32] G. Whyman, E. Bormashenko, T. Stein, The rigorous derivation of Young, Cassie–Baxter and Wenzel equations and the analysis of the contact angle hysteresis phenomenon, *Chem. Phys. Lett.* 450 (2008) 355–359. doi:10.1016/j.cplett.2007.11.033.
- [33] Z. Yoshimitsu, A. Nakajima, Toshiya Watanabe, K. Hashimoto, Effects of Surface Structure on the Hydrophobicity and Sliding Behavior of Water Droplets, *Langmuir.* 18 (2002) 5818–5822. doi:10.1021/la020088p.
- [34] X. Zhan, Y. Yan, Q. Zhang, F. Chen, A novel superhydrophobic hybrid nanocomposite material prepared by surface-initiated AGET ATRP and its anti-icing properties, *J. Mater. Chem. A.* 2 (2014) 9390. doi:10.1039/c4ta00634h.
- [35] S.A. Kulkarni, S.B. Ogale, K.P. Vijayamohanan, Tuning the hydrophobic properties of silica particles by surface silanization using mixed self-assembled monolayers, *Colloid I.* 318 (2008) 372–379. doi:10.1016/j.jcis.2007.11.012.
- [36] L. Feng, S.H. Li, Y.S. Li, H.J. Li, L.J. Zhang, J. Zhai, et al., Super-hydrophobic surfaces: From natural to artificial, *Adv. Mater.* 14 (2002) 1857–1860. doi:DOI 10.1002/adma.200290020.
- [37] B. Bhushan, K. Koch, Y.C. Jung, Biomimetic hierarchical structure for self-cleaning, *Appl. Phys. Lett.* 93 (2008) 2006–2009. doi:10.1063/1.2976635.
- [38] Y.T. Cheng, D.E. Rodak, C.A. Wong, C.A. Hayden, Effects of micro- and nano-structures on the self-cleaning behaviour of lotus leaves, *Nanotechnology.* 17 (2006) 1359–1362. doi:10.1088/0957-4484/17/5/032.
- [39] Y.-T. Cheng, D.E. Rodak, Is the lotus leaf superhydrophobic?, *Appl. Phys. Lett.* 86 (2005) 144101. doi:10.1063/1.1895487.
- [40] T. Harada, H. Murotani, S. Matumoto, H. Honda, Influence of substrate surface roughness on light scattering of TiO<sub>2</sub> optical thin films, *Chinese Opt. Lett.* 11 (2013) 9–12. doi:10.3788/COL201311.S10303.Optical.
- [41] Y.J. Lin, P. Dias, S. Chum, A. Hiltner, E. Baer, Surface roughness and light transmission of biaxially oriented polypropylene films, *Polym. Eng. Sci.* 47 (2007) 1658–1665. doi:10.1002/pen.20850.
- [42] H.-J. Kim, O.-J. Kwon, Y.-G. Han, Effect of Surface Roughness Variation on the

- Transmission Characteristics of D-shaped Fibers with Ambient Index Change, *J. Korean Phys. Soc.* 56 (2010) 1355. doi:10.3938/jkps.56.1355.
- [43] M.A. Green, K. Emery, Y. Hishikawa, W. Warta, E.D. Dunlop, Solar cell efficiency tables (version 45), *Prog. Photovoltaics Res. Appl.* 23 (2015) 1–9. doi:10.1002/pip.
- [44] N. Gao, Y.Y. Yan, X.Y. Chen, D.J. Mee, Superhydrophobic surfaces with hierarchical structure, *Mater. Lett.* 65 (2011) 2902–2905. doi:10.1016/j.matlet.2011.06.088.
- [45] Q. Ke, W. Fu, H. Jin, L. Zhang, T. Tang, J. Zhang, Fabrication of mechanically robust superhydrophobic surfaces based on silica micro-nanoparticles and polydimethylsiloxane, *Surf. Coatings Technol.* 205 (2011) 4910–4914. doi:10.1016/j.surfcoat.2011.04.073.
- [46] M. Jin, X. Feng, J. Zhai, K. Cho, L. Feng, L. Jiang, Super-Hydrophobic PDMS Surface with Ultra-Low Adhesive Force, (2005) 1–2.
- [47] K. Koch, B. Bhushan, Y.C. Jung, W. Barthlott, Fabrication of artificial Lotus leaves and significance of hierarchical structure for superhydrophobicity and low adhesion, *Soft Matter*. 5 (2009) 1386. doi:10.1039/b818940d.
- [48] R. Fürstner, W. Barthlott, C. Neinhuis, P. Walzel, Wetting and self-cleaning properties of artificial superhydrophobic surfaces, *Langmuir*. 21 (2005) 956–961. doi:10.1021/la0401011.
- [49] N.J. Shirtcliffe, G. McHale, S. Atherton, M.I. Newton, An introduction to superhydrophobicity, *Adv. Colloid Interface Sci.* 161 (2010) 124–138. doi:10.1016/j.cis.2009.11.001.
- [50] D. Tarn, C.E. Ashley, M.I.N. Xue, E.C. Carnes, J.I. Zink, C.J. Brinker, Mesoporous Silica Nanoparticle Nanocarriers: Biofunctionality and Biocompatibility, *Acc. Chem. Res.* 46 (2013) 792–801.
- [51] H. Ogihara, J. Xie, J. Okagaki, T. Saji, Simple method for preparing superhydrophobic paper: spray-deposited hydrophobic silica nanoparticle coatings exhibit high water-repellency and transparency., *Langmuir*. 28 (2012) 4605–8. doi:10.1021/la204492q.
- [52] J. Bravo, L. Zhai, Z. Wu, R.E. Cohen, M.F. Rubner, Transparent superhydrophobic films based on silica nanoparticles, *Langmuir*. 23 (2007) 7293–7298. doi:10.1021/la070159q.
- [53] X. Liu, J. He, Hierarchically structured superhydrophilic coatings fabricated by self-assembling raspberry-like silica nanospheres, *J. Colloid Interface Sci.* 314 (2007) 341–345. doi:10.1016/j.jcis.2007.05.011.
- [54] X. Zhang, A. Fujishima, M. Jin, A. V Emeline, T. Murakami, Double-Layered TiO<sub>2</sub>-SiO<sub>2</sub> Nanostructured Films with Self-Cleaning and Antireflective Properties, *J. Phys. Chem. B.* 110 (2006) 25142–25148. doi:10.1021/jp064442u.
- [55] S. Anand, A.T. Paxson, R. Dhiman, J.D. Smith, K.K. Varanasi, Enhanced condensation on lubricant-impregnated nanotextured surfaces, *ACS Nano*. 6 (2012)

10122–10129. doi:10.1021/nm303867y.

- [56] A. Lafuma, D. Quéré, Slippery pre-suffused surfaces, *EPL (Europhysics Lett.* 96 (2011) 56001. doi:10.1209/0295-5075/96/56001.
- [57] K. Rykaczewski, S. Anand, S.B. Subramanyam, K.K. Varanasi, Mechanism of frost formation on lubricant-impregnated surfaces, *Langmuir.* 29 (2013) 5230–5238. doi:10.1021/la400801s.
- [58] J.D. Smith, R. Dhiman, S. Anand, E. Reza-Garduno, R.E. Cohen, G.H. McKinley, et al., Droplet mobility on lubricant-impregnated surfaces, *Soft Matter.* 9 (2013) 1772–1780. doi:10.1039/C2SM27032C.
- [59] B. Solomon, K. Khalil, K. Varanasi, Lubricant-impregnated surfaces for drag reduction in viscous laminar flow, *Bull. Am. Phys. Soc. Volume 58*, (2013). <http://meetings.aps.org/link/BAPS.2013.DFD.H7.5>.
- [60] S.B. Subramanyam, K. Rykaczewski, K.K. Varanasi, Ice adhesion on lubricant-impregnated textured surfaces, *Langmuir.* 29 (2013) 13414–13418. doi:10.1021/la402456c.
- [61] a. Venkateswara Rao, S.S. Latthe, D.Y. Nadargi, H. Hirashima, V. Ganesan, Preparation of MTMS based transparent superhydrophobic silica films by sol-gel method, *J. Colloid Interface Sci.* 332 (2009) 484–490. doi:10.1016/j.jcis.2009.01.012.
- [62] S.S. Latthe, H. Imai, V. Ganesan, a. V. Rao, Superhydrophobic silica films by sol-gel co-precursor method, *Appl. Surf. Sci.* 256 (2009) 217–222. doi:10.1016/j.apsusc.2009.07.113.
- [63] M.M. Stanton, R.E. Ducker, J.C. MacDonald, C.R. Lambert, W.G. McGimpsey, Super-hydrophobic, highly adhesive, polydimethylsiloxane (PDMS) surfaces., *J. Colloid Interface Sci.* 367 (2012) 502–8. doi:10.1016/j.jcis.2011.07.053.
- [64] B. Bhushan, Y.C. Jung, K. Koch, Self-Cleaning Efficiency of Artificial Superhydrophobic Surfaces, *Langmuir.* 25 (2009) 3240–3248. doi:10.1039/b818940d.
- [65] M. Sun, C. Luo, L. Xu, H. Ji, Q. Ouyang, D. Yu, et al., Artificial Lotus Leaf by Nanocasting, *Langmuir.* 21 (2005) 8978–8981.
- [66] Y. Chen, W. Pei, R. Tang, S. Chen, H. Chen, Conformal coating of parylene for surface anti-adhesion in polydimethylsiloxane ( PDMS ) double casting technique, *Sensors Actuators A Phys.* 189 (2013) 143–150.
- [67] G. Shao, J. Wu, Z. Cai, W. Wang, Fabrication of elastomeric high-aspect-ratio microstructures using polydimethylsiloxane (PDMS) double casting technique, *Sensors Actuators A Phys.* 178 (2012) 230–236. doi:10.1016/j.sna.2012.01.034.
- [68] L. Gitlin, P. Schulze, D. Belder, Rapid replication of master structures by double casting with PDMS., *Lab Chip.* 9 (2009) 3000–2. doi:10.1039/b904684d.
- [69] M. a. Hubbe, Detachment of colloidal hydrous oxide spheres from flat solids

- exposed to flow 4. Effect of polyelectrolytes, *Colloids and Surfaces*. 25 (1987) 325–339.
- [70] D. Leighton, A. Acrivos, The lift on a small sphere touching a plane in the presence of a simple shear flow, *ZAMP Zeitschrift F  r Angew. Math. Und Phys.* 36 (1985) 174–178.
  - [71] P. Cherukat, J.B. McLaughlin, The inertial lift on a rigid sphere in a linear shear flow field near a flat wall, *J. Fluid Mech.* 285 (1995) 407.
  - [72] F.M. White, *VISCOUS FLUID FLOW*, 3rd ed., McGraw-Hill, 2005.
  - [73] M.E. O’Neill, A sphere in contact with a plane wall in a slow linear shear flow, *Chem. Eng. Sci.* 23 (1968) 1293–1298.
  - [74] A.J. Goldmans, R.G. Cox, H. Brenner, O. Neill, Slow viscous motion of a sphere parallel to a plane wall-1 Motion through a quiescent fluid +, 22 (1967).
  - [75] M.B. Lyles, H.L. Fredrickson, a. J. Bednar, H.B. Fannin, D. Griffin, T.M. Sobecki, Medical Geology : Dust exposure and potential health risks in the Middle East ., *Geochim. Cosmochim. Acta.* 10 (2008) 1–4.
  - [76] K. Kandler, N. Benker, U. Bundke, E. Cuevas, M. Ebert, P. Knippertz, et al., Chemical composition and complex refractive index of Saharan Mineral Dust at Iza  a, Tenerife (Spain) derived by electron microscopy, *Atmos. Environ.* 41 (2007) 8058–8074. doi:10.1016/j.atmosenv.2007.06.047.
  - [77] B.S. Yilbas, H. Ali, M.M. Khaled, N. Al-Aqeeli, N. Abu-Dheir, K.K. Varanasi, Influence of dust and mud on the optical, chemical, and mechanical properties of a pv protective glass, *Sci. Rep.* 5 (2015) 15833. doi:10.1038/srep15833.

## Vitae

Name : Aditia Rifai

Nationality : Indonesia

Date of Birth : 10/14/1987

Email : aditiarifai47@gmail.com

Address : KFUPM student housing, building 803 room 301

Academic Background : Bachelor degree in Engineering Physic

Publications : Aditia Rifai, Muhammad Iqbal, Nugraha , Ahmad Nuruddin, Suyatman and Brian Yuliarto, Synthesis and Characterization of SnO<sub>2</sub> Thin Films by Chemical Bath Deposition, AIP Conf. Proc. 1415, 231 (2011)

B. Yuliarto, N. Nugraha, B. Epindonta, R. Aditia, M. Iqbal, "Synthesis of SnO<sub>2</sub> Nanostructure Thin Film and its Prospective as Gas Sensors", Advanced Materials Research, Vol. 789, pp. 189-192, 2013

Aditia Rifai, Numan Abu Dheir, Bekir Sami Yilbas, Mazen Khaled, Mechanics of dust removal from rotating disk in relation to self-cleaning applications of PV protective cover, Solar Energy, vol. 130, pp. 193-206, 2016

Aditia Rifai, Numan Abu-Dheir, Mazen Khaled, Bekir  
Sami Yilbas, Fabrication of Transparent Self-cleaning  
Surface by Oil Impregnation on Silica Nanoparticle Layer  
(ready to submit)